

Convective Cold Pools over the Atlas Mountains and Their Influence on the Saharan Heat Low



INAUGURAL - DISSERTATION

zur
Erlangung des Doktorgrades
der Mathematisch-Naturwissenschaftlichen Fakultät
der Universität zu Köln
vorgelegt von

Robert Redl

aus Cham

Freising, 2016

Berichtersteller/in: Prof. Dr. Andreas H. Fink
Prof. Dr. Susanne Crewell
Prof. Dr. Peter Knippertz

Tag der mündlichen Prüfung: 25.01.2016

Abstract

The West African Monsoon (WAM) and its representation in numerical models are strongly influenced by the Saharan Heat Low (SHL), a low-pressure system driven by radiative heating over the central Sahara and ventilated by the cold and moist inflow from adjacent oceans. It has recently been shown that a significant part of the southerly moisture flux into the SHL originates from convective cold pools over the Sahel. These density currents driven by evaporation of rain are largely absent in models with parameterized convection. This crucial issue has been hypothesized to contribute to the inability of many climate models to reproduce the variability of the WAM.

Here, the role of convective cold pools approaching the SHL from the Atlas Mountains, which are a strong orographic trigger for deep convection in Northwest Africa, is analyzed. Knowledge about the frequency of these events, as well as their impact on large-scale dynamics, is required to understand their contribution to the variability of the SHL and to known model uncertainties. The first aspect is addressed through the development of an objective and automated method for the generation of multi-year climatologies not available before. The algorithm combines freely available standard surface observations with satellite microwave data. Representativeness of stations and influence of their spatial density are addressed by comparison to a satellite-only climatology. Applying this algorithm to data from automated weather stations and manned synoptic stations in and south of the Atlas Mountains reveals the frequent occurrence. On the order of 6 events per month are detected from May to September when the SHL is in its northernmost position. The events tend to cluster into several-days long convectively active periods, often with strong events on consecutive days.

This study is the first to diagnose dynamical impacts of such periods on the SHL, based on simulations of two example cases using the Weather Research and Forecast (WRF) model at convection-permitting resolution. Sensitivity experiments with artificially removed cold pools as well as different resolutions and parameterizations are conducted. Results indicate increases in surface pressure of more than 1 hPa and significant moisture transports into the desert over several days. This moisture affects radiative heating and thus the energy balance of the SHL. Even though cold pool events north of the SHL are less frequent when compared to their Sahelian counterparts, it is shown that they gain importance due to their temporal clustering on synoptic timescale. Together with studies focusing on the Sahel, this work emphasizes the need for improved parameterization schemes for deep convection in order to produce more reliable climate projections for the WAM.

Key Points

- From May to September, about 6 large cold pool events per month are detected over the Atlas Mountains.
- These events are often clustered into several days long periods.
- Cold pools increase surface pressure and transport moisture into the Sahara over multiple days.
- Cold pools contribute to the variability of the heat low on synoptic time scale.

Zusammenfassung

Kernaussagen

- Von Mai bis September werden über dem Atlas Gebirge ca. 6 große Dichteströmungsereignisse pro Monat detektiert.
- Diese Ereignisse treten oft gruppiert über mehrere Tage hinweg auf.
- In diesen Perioden erhöhen die Dichteströmungen den Bodendruck und transportieren Feuchte in die Sahara.
- Dichteströmungen aus dem Atlas Gebirge tragen zur Variabilität des Hitzetiefs auf der synoptischen Zeitskala bei.

Der westafrikanische Monsun (WAM) und seine Darstellung in numerischen Modellen ist stark beeinflusst vom Hitzetief über der zentralen Sahara (engl.: *Saharan Heat Low*, SHL). Dieses Tiefdruckgebiet entsteht durch starke Einstrahlung, ein Druckausgleich erfolgt durch den Zustrom kalter und feuchter Luft von den angrenzenden Ozeanen. Es konnte unlängst gezeigt werden, dass ein wesentlicher Anteil der von Süden in das Hitzetief transportierten Feuchte im Zusammenhang steht mit Dichteströmungen aus Konvektion in der Sahelzone. Diese Dichteströmungen werden durch das Verdunsten von Regen erzeugt und sind in Modellen mit parametrisierter Konvektion nur unzureichend repräsentiert. Es wurde die Hypothese aufgestellt, dass es sich hierbei um einen entscheidenden Beitrag zu Unzulänglichkeiten bei der Wiedergabe des WAM handelt.

Die Rolle der konvektiven Dichteströmungen wird hier untersucht für Ereignisse mit Ursprung über dem Atlasgebirge, einem starken orographischen Auslöser für hochreichende Konvektion in Nord-West-Afrika. Um den Beitrag dieser Ereignisse zur Variabilität und zu bekannten Unsicherheiten in Modellen zu verstehen, ist sowohl die Kenntnis ihrer Häufigkeit als auch ihrer Auswirkung auf die großskalige Dynamik erforderlich. Der Aspekt der Häufigkeit wird durch die Entwicklung einer objektiven und automatisierten Methode zur Erstellung mehrjähriger Klimatologien untersucht. Der Algorithmus kombiniert standardmäßig durchgeführte Bodenbeobachtungen mit Satellitenmessungen im Mikrowellenbereich, beides ist frei verfügbar. Die Repräsentativität der Stationen und der Einfluss ihrer räumlichen Verteilung werden durch Vergleich mit einer nur aus Satellitendaten erstellten Klimatologie untersucht. Durch Anwendung des Algorithmus auf Daten automatischer Wetterstationen und bemannter synoptischer Stationen im und südlich des Atlasgebirges wird das häufige Auftreten von Dichteströmungsereignissen in dieser Region gezeigt. Etwa sechs Ereignisse pro Monat werden von Mai bis September detektiert, das Hitzetief ist zu dieser Zeit in seiner nördlichsten Position. Die Ereignisse tendieren zu einer Gruppierung in konvektiv aktive Perioden, die sich über mehrere Tage erstrecken, häufig mit zwei starken Ereignissen an aufeinander folgenden Tagen.

Der Aspekt der dynamischen Auswirkungen auf das Hitzetief durch solche konvektiven Perioden wird in dieser Studie zum ersten Mal analysiert. Die Grundlage dafür bilden Simulationen zweier Beispielfälle mit dem Wetterforschungs- und Vorhersage-Modell WRF (engl.: *Weather Research and Forecast*) bei konvektionserlaubender Auflösung. Es werden Sensitivitätsexperimente durchgeführt mit künstlich entfernten Dichteströmungen, geringeren Auflösungen und Parametrisierun-

gen für Konvektion. Die Resultate zeigen, dass Dichteströmungen über mehrere Tage hinweg zu einem Anstieg des Bodendrucks von mehr als 1 hPa und zu einem signifikanten Transport von Feuchte in die Wüste führen. Diese Feuchte hat Einfluss auf die strahlungsbedingte Erwärmung und somit auch auf die Energiebilanz im Hitzetief. Obwohl Dichteströmungsereignisse nördlich des Hitzetiefs verglichen mit der Sahelzone weniger häufig auftreten, gewinnen sie trotzdem an Bedeutung durch ihr gruppiertes Auftreten auf der synoptischen Zeitskala. Zusammen mit auf die Sahelzone fokussierten Studien hebt diese Arbeit die Notwendigkeit verbesserter Parametrisierung für Konvektion hervor. Ohne Fortschritte in diesem Bereich können keine verlässlichen Klimaprojektionen für den WAM erstellt werden.

Contents

Abstract	I
Zusammenfassung	II
1. Introduction	1
1.1. The Saharan Heat Low and its Variability	4
1.2. Convectively Generated Cold Pools	11
1.3. Objectives and Structure of This Study	17
2. Data	21
2.1. IMPETUS Station Network	22
2.2. Fennec Station Network	23
2.3. SYNOP and METAR	24
2.4. Meteosat SEVIRI 'Desert Dust' Product	25
2.5. AMSU-B and MHS Microwave Data	27
2.6. ECMWF (Re)-Analysis Data	29
3. Methods	31
3.1. Objective Cold Pool Detection Algorithm	31
3.1.1. Ground Observation Screening	31
3.1.2. Microwave Satellite Convection Screening	34
3.1.3. Limb Correction for AMSU-B and MHS	37
3.2. Sensitivity Experiments with WRF	39
3.2.1. The WRF Model and its Configuration	39
3.2.2. Modifications of Model Microphysics	41
3.2.3. Tracing of Moisture from Evaporation of Rain	44
3.2.4. Low Resolution Experiments with Different Con- vection Schemes	46
4. Climatology of Convective Cold Pool Events	47
4.1. Climatology with Station Data	47
4.2. Satellite Only Climatology	52
4.3. Atlas Mountains Convection Index	54
5. Impact of Convective Cold Pools on the Saharan Heat Low	59
5.1. Case Selection	59
5.2. Description of Case 1: 2011-06-20 to 2011-06-24	59
5.3. Description of Case 2: 2012-06-27 to 2012-07-01	64
5.4. Impact on Surface Pressure	68
5.5. Cold Pools as Moisture Source for the Desert	69

5.6. Modification of Surface Radiation Balance	69
5.7. Representation of Cold Pools with Low Resolution	75
6. Summary, Discussion, and Outlook	81
6.1. Spatio-Temporal Variability of Cold Pool Activity	81
6.2. Impact of Cold Pools on the Saharan Heat Low	83
6.3. Future Perspectives	85
A. Appendix	87
A.1. Noise Detection in Microwave Satellite Data	87
References	91
Acronyms	99
Danksagung	103
Erklärung	105

1. Introduction

The [West African Monsoon \(WAM\)](#) is a complex and closely coupled system of interactions between ocean, land surface, and atmosphere. Climate models struggle to realistically reproduce the precipitation variability associated with this system ([Hourdin et al. 2010](#)). This is particularly pertinent to the Sahel region (approx. 12°N–20°N), where agricultural productivity, and thus the livelihood of the population, is highly dependent on sufficiently large precipitation amounts. The Sahel was affected by a major drought in the 1970s and 1980s, but rainfall has been recovering since then ([Sanogo et al. 2015](#)). Despite large efforts during the last decade to explain this recovery and to better understand the [WAM](#) system, including international research programs and field campaigns such as [African Monsoon Multidisciplinary Analyses \(AMMA\)](#) ([Redelsperger et al. 2006](#); [Parker et al. 2008](#)) and [Fennec](#) ([Washington et al. 2012](#)), the reasons are still a matter of discussion. The recovery has been attributed to variability in [Sea Surface Temperatures \(SSTs\)](#) (e.g., [Rodríguez-Fonseca et al. 2011](#); [Martin et al. 2014](#)), which in turn are affected by aerosols (e.g., [Booth et al. 2012](#)), but also to natural ([Evan et al. 2015](#)) and anthropogenic ([Dong and Sutton 2015](#)) greenhouse gas warming of the [Saharan Heat Low \(SHL\)](#), a key component of the [WAM](#). Average surface warming rates over the Sahara are at least two times larger than the global mean ([Cook and Vizy 2015](#)), the causes of which are still disputed ([Lavaysse 2015](#)).

During the summer monsoon season the center of the [SHL](#) is typically located over the central Sahara near the border between Algeria and Mali ([Lavaysse et al. 2009](#)). It drives the moist southwesterly monsoon flow across the Guinea Coast towards the Sahel, as well as the dry northerly Harmattan winds across the Sahara ([Parker et al. 2005](#); [Lavaysse et al. 2009](#)). Caused by a lack of operational observations and complex dynamics, the [SHL](#) region has been identified as a major source of uncertainty for modeling the [WAM](#) ([Agustí-Panareda et al. 2010](#); [Garcia-Carreras et al. 2013](#)). With the Sahara being the most important mineral dust source on earth (e.g., [Prospero 2002](#)), aerosol forcing has received much attention, e.g., during the recent [Fennec](#) project (e.g., [Ashpole and Washington 2013](#); [Marshall et al. 2013b](#); [Ryder et al. 2013](#); [Todd et al. 2013](#); [Allen et al. 2015](#)). Uplifted dust is known to have a cooling effect on the surface ([Evan et al. 2009](#)), but processes leading to dust emission like monsoon surges or convectively driven cold

pools are usually related to an increasing amount of water vapor, which in contrast amplifies radiative heating (Marsham et al. 2015).

Even if called into question (Cook and Vizy 2015; Lavaysse 2015), Evan et al. (2015) suggested that an increasing amount of water vapor in the lower troposphere is responsible for the deepening of the SHL (increase in lower tropospheric temperature) in the past decades. Observations made in 2011 in Bordj Badji Mokhtar (BBM) in southern Algeria (Garcia-Carreras et al. 2013) and a modeling study conducted by Marsham et al. (2013a) indicate that a significant part of the meridional moisture flux towards the SHL is caused by convective cold pools created by Mesoscale Convective Systems (MCSs) in the Sahel. The dynamics of these MCSs, typically embedded into African Easterly Waves (AEWs) (e.g., Fink and Reiner 2003; Lavaysse et al. 2006), are not captured by global models due to insufficient horizontal resolution and the consequent usage of convective parameterization schemes (Marsham et al. 2013a). This problem is also reflected in large discrepancies between different (re)-analysis products, which are widely used to study the WAM (Roberts et al. 2014). AEWs contribute from the south to the variability of the SHL on the synoptic time scale (e.g., Couvreux et al. 2010; Lavaysse et al. 2010). From the north, pathways of ventilation for the SHL investigated so far are cold surges from the Mediterranean Sea, often related to mid-latitude Rossby waves (e.g., Knippertz 2008; Vizy and Cook 2009; Lavaysse et al. 2010), and the so-called Atlantic inflow, which is a sea-breeze front at the Mauritanian coast reaching exceptionally far inland (Grams et al. 2010). The Atlas Mountains are located in between as an orographic barrier.

Against the background of the relevance of cold pools from Sahel convection, the question arises whether and to what extent the SHL is affected by cold pools originating from the Atlas Mountains in Morocco, northern Algeria, and Tunisia, which are located at the northern flank of the SHL. A marked characteristic of cold pools in semi-arid environments like northwestern Africa is the associated steep increase in dew point temperature (T_d) at the surface (e.g., Knippertz et al. 2007; Engerer et al. 2008; Emmel et al. 2010). Comparing this variable measured at manned synoptic and Automated Weather Station (AWS) with the operational analysis of the European Centre for Medium-Range Weather Forecasts (ECMWF) indicates that issues with parameterized convection, as known from the Sahel region, affect Northwest Africa in a very similar way (Figs. 1.1a–c). Biases during the winter months are small in magnitude and do not show a systematic geographical distribution (Fig. 1.1a). On the contrary, in summer biases are predominantly negative reaching values well below -3K, particularly along the southern foothills of the Atlas chain (Fig. 1.1b). Monthly time series show a continuous increase in the negative bias of dew point temperature towards the summer months, with the largest magnitudes in July

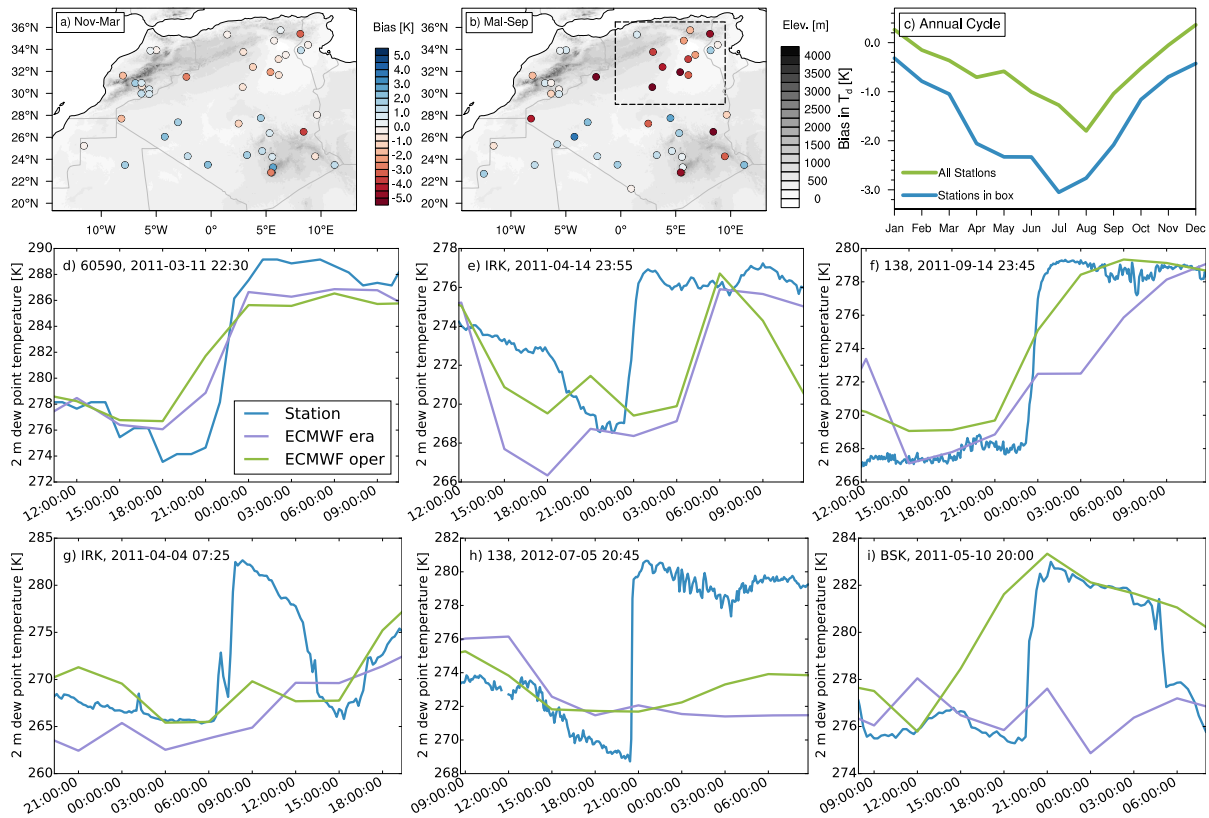


Figure 1.1.: Bias in 2 m dew point temperature (T_d) in the ECMWF operational analysis with regard to ground observations. (a) Average bias per station for the months November-March for 2011–2012. (b) As (a) but for the months May-September, the dashed box indicates an area with particularly pronounced biases. (c) Annual cycle of the bias averaged over all stations and over the stations located in the dashed box from panel (b). (d-i) Temporal evolution of T_d for example cases with ERA-Interim included as additional information. Source: Redl et al. (2016).

and August (Fig. 1.1c). Looking at individual cases and stations reveals an interesting mix of satisfactory reproduction in both ECMWF operational analysis and ERA-Interim re-analysis (Fig. 1.1d-f), missed events (Fig. 1.1g and h), and large discrepancies between the two analysis products (Fig. 1.1i).

These biases in dew point temperature suggest that cold pool events could be an additional pathway of ventilation for SHL, so far not sufficiently investigated and presumably misrepresented in numerical models. The assessment of these events is split up into two parts: (a) are convective cold pool events a regular feature at the northern flank of the SHL, as indicated by a first climatology created by Emmel et al. (2010)? (b) is there a significant impact of these cold pool events on larger scale dynamics? Answers can contribute to an improved understanding and prediction of the SHL variability on time scales of days to weeks.

1.1. The Saharan Heat Low and its Variability

The SHL¹ is a thermal low driven by temperature differences between the continent, with maxima in the hyper-arid Saharan desert, and the surrounding oceans, with minima related to cold currents like the South Equatorial or Canary Current. Such heat lows are persistent climatological features during the warmer months of the year in arid regions around the world, where insolation is high and evaporation is low (e.g., Rácz and Smith 1999, and references therein). In a review of the findings from the AMMA project, Lafore et al. (2011) highlighted the importance of the SHL as a key component of the WAM and its interactions with other components of the system, all shown for January and July in Fig. 1.2 and in detail discussed in Fink et al. (2016).

The low surface pressure in the SHL drives the moist southwesterly monsoon flow across the Guinea Coast towards the Sahel, as well as the dry northerly Harmattan winds across the Sahara (Parker et al. 2005; Lavaysse et al. 2009). Both flows converge in the region of the SHL along the so-called Inter-Tropical discontinuity (ITD). The resultant baroclinity of the dry and hot air in the north and colder and moist air in the south is an important driver for the African Easterly Jet (AEJ), a wind speed maximum around 700 hPa, and also responsible for instabilities of this waveguide, which create AEWs (Thorncroft and Blackburn 1999). AEWs with wavelengths of 2000–4000 km and westward propagation speeds around 8 ms⁻¹ are the most important synoptic features in the WAM and play a crucial role in the organization of deep convection into MCSs (Fink and Reiner 2003; Lavaysse et al. 2006). This organization is of particular importance as 70–90% of the precipitation in the Sudan and Sahel zones originates from MCSs (Mathon et al. 2002; Fink et al. 2006).

Against the background of this process chain from the SHL to the MCSs, it becomes clear that variations of the SHL translate into variations of precipitation amounts in tropical West Africa. On the decadal time scale, this link recently attracted attention as it might help to explain the recovery from the Sahel drought since the 1980s. Using rain gauge data from stations between the African west coast and 15°E, Sanogo et al. (2015) found a statistically significant positive trend in annual totals as well as in extreme events exceeding the 95th percentile in the Sahel. Using observations and re-analysis products, another positive trend with temporal coincidence was found by Evan et al. (2015) in SHL air temperatures. These authors attributed the deepening of the SHL to a rising concentration of water vapor in the lower troposphere, which is a natural greenhouse gas. Especially at night-time, water vapor

¹SHL vs. WAHL: In Literature the alternative term West African Heat Low (WAHL) is also frequently used instead SHL (e.g., Lavaysse et al. 2009, 2010), especially when a distinction from the eastern counterpart is intended (Fink et al. 2016).

1. Introduction

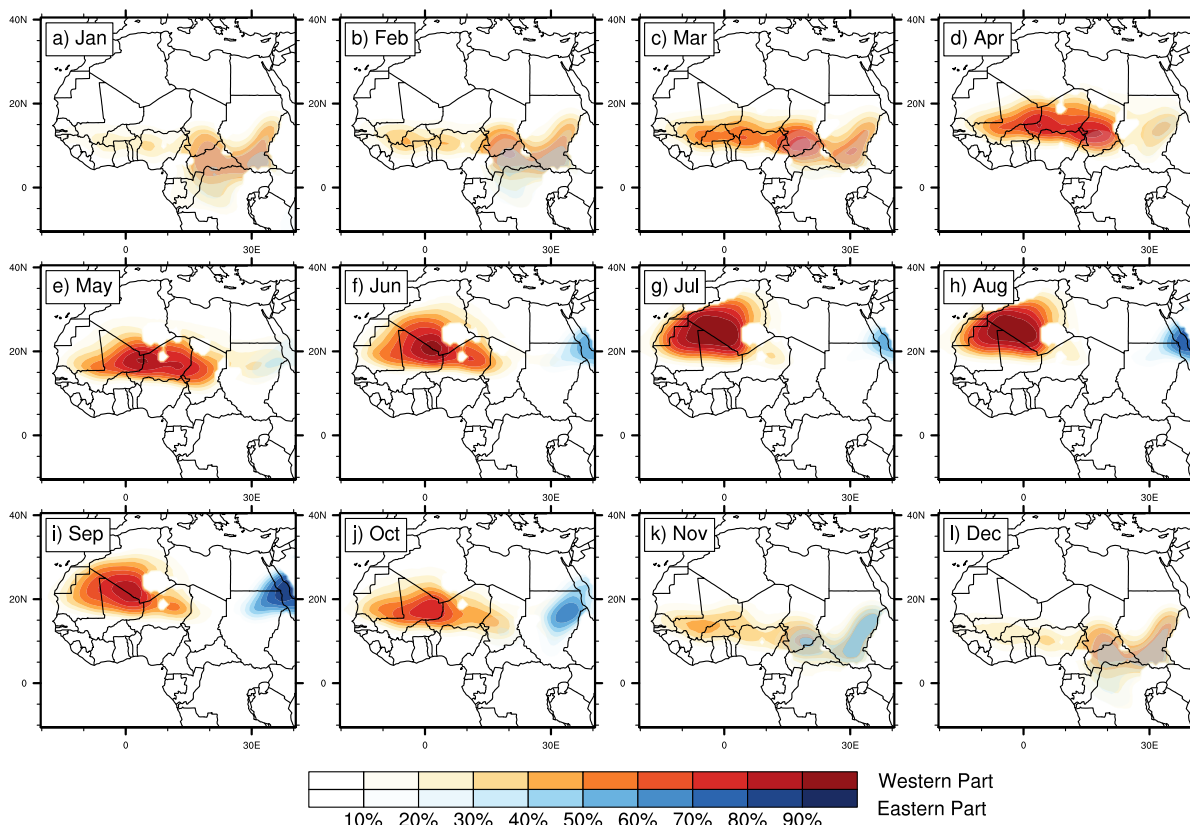


Figure 1.3.: Seasonal cycle of the SHL. Monthly mean values of the position calculated from ERA-Interim for the time period 1979–2014. Shown is the frequency of occurrence at each grid point. Grid points with an elevation above the 925 hPa surface were excluded from the calculation, which results in white spots at the margins of the SHL.

forms a positive contribution to the radiation balance. [Dong and Sutton \(2015\)](#) offer a different explanation. They identified in experiments with a global climate model higher levels of anthropogenic greenhouse gases as main reason for the deepening of the SHL. But regardless of the reason, both studies agree that the changes of the SHL played a major role in the recovery from the Sahel drought. A point of view that is shared by [Lavaysse \(2015\)](#), who points out that the reason for the warming trend over the Sahara, which is at least two times larger than global according to [Cook and Vizy \(2015\)](#), is still unknown.

A method to assess changes to the SHL was suggested by [Lavaysse et al. \(2009\)](#). They calculated the layer depth between 700 and 925 hPa in a domain spanning from 20°W–20°E and 0°N–40°N. The SHL is then defined as the region where layer depth values above the 90th percentile with respect to the domain mentioned before are found. Only 06 UTC re-analysis fields are used as the impact of clouds and convection is minimal at this time. This method was used here to create Figs. 1.3 and 1.4, but with an extended domain and two additional modifications. Firstly, grid points above the 90% threshold are grouped together into contiguous areas; during the boreal summer months this results in two distinct heat lows. One over the Sahara and one over the Arabic Penin-

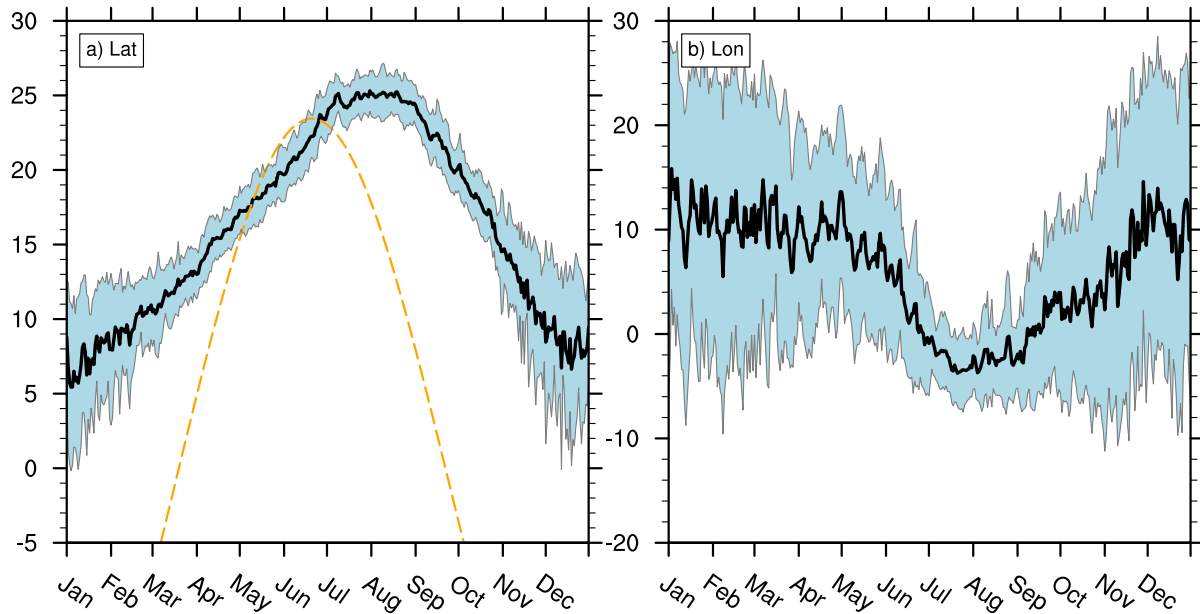


Figure 1.4.: Seasonal cycle of the SHL. Monthly mean values of the position calculated from ERA-Interim for the time period 1979–2014. Shown is (a) the latitude in degrees north and (b) the longitude in degrees east of the western part (see Fig. 1.3) with daily resolution. The blue area indicates the standard deviation and the dashed orange line in (a) the zenith position of the sun.

sula (referred to as western and eastern part in Fig. 1.3). Secondly, in order to make this feature detection more robust a 1000 km spatial low-pass filter was applied to the input data prior to the calculation of the layer depth².

The method described above allows the reliable calculation of the SHL position from decadal down to daily time scales (Lavaysse et al. 2009), but care should be taken for interpretations. The method is only as good as its input data and unfortunately re-analysis products show significant discrepancies for the SHL and ITD region (e.g., Roberts et al. 2014; Cook and Vizy 2015). Roberts et al. (2014) attributes the discrepancies to misrepresentation of important processes and lack of assimilated observations. But keeping that in mind, the method is still well suitable to analyze the variability of the SHL.

The climatological seasonal cycle (Figs. 1.3 and 1.4) shows two extrema in the position of the SHL. In boreal winter (November–February), it is located in the Sahel and central Africa between 5 and 10°N and in boreal summer (June–September) over the Sahara between the Atlas and Hoggar Mountains (20–25°N). The simultaneous shift in the location of other components of the WAM is illustrated in Fig. 1.2. The SHL south-north movement follows the zenith position of the sun, but shows a delay of 1–2 months (Fig. 1.4a). Lavaysse et al. (2009) speculated

²The SHL analysis adapted in this way has been contributed to the Central Evaluation System (CES; Kadow et al. 2014) of the decadal prediction project MiKlip (*Mittelfristige Klimaprognose*) (Pohlmann et al. 2013). It is used in the CES to evaluate the representation of the SHL in regional and global climate models.

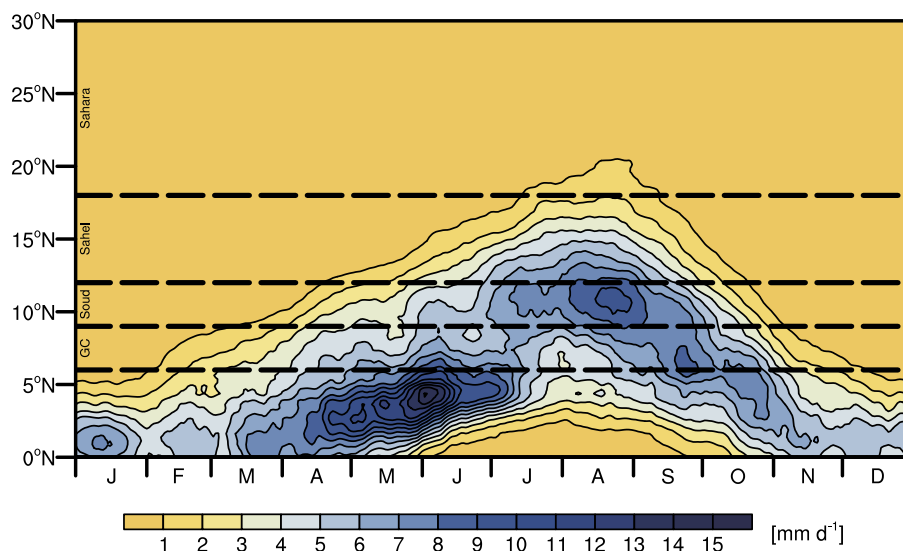


Figure 1.5.: Mean annual precipitation in tropical West Africa. Hovmöller diagram of the 15-day running mean of daily precipitation, obtained from the TRMM product 3B42, 1998–2012, averaged between 10°W and 10°E. Source: Fink et al. (2016).

about complex surface-atmosphere interactions to be responsible for this delay without going into details. Fink et al. (2016) showed a peak in July and August in the net radiation balance in Sahel and Sahara using data from the Global Energy and Water Exchanges (GEWEX) project. In the Sahel, the maximum has been attributed to changes in vegetation, cloudiness, and specific humidity (Guichard et al. 2009). However, vegetation can be neglected in the central Sahara, which makes water vapor and cloudiness likely to cause the late summer maximum.

Even more interesting is the east-west movement of the SHL, especially the transition from the position south-east of the Hoggar Mountains (May, Fig. 1.3e) to the position between the Atlas and Hoggar Mountains (July, Fig. 1.3g). This rather abrupt transition happens around 20 June (Lavaysse et al. 2009 and Fig. 1.4b). Sultan and Janicot (2003) found the monsoon onset to happen only a few days later at 24 June. As pointed out by Fitzpatrick et al. (2015), this date is dependent on the definition of the onset as well as on the dataset used for the calculation, but always happens in late June or early July. This jump is well visible in zonally averaged precipitation in tropical West Africa (Fig. 1.5). The physical background is an active field of research, not least because most global and regional climate models struggle to reproduce it, which results in an Inter-Tropical Convergence Zone (ITCZ) located too far in the south (e.g., Martin et al. 2014; García-Serrano et al. 2013; Hourdin et al. 2010). According to Janicot et al. (2015), who recently highlighted key research questions with regard to the prediction of the WAM, surface conditions in the area of the SHL and of the so-called Atlantic cold tongue in the Gulf of Guinea (indicated by a blue area at the equator in Fig. 1.2b) are of major importance. Unfortunately, both areas are related to large uncertainties in numerical models.

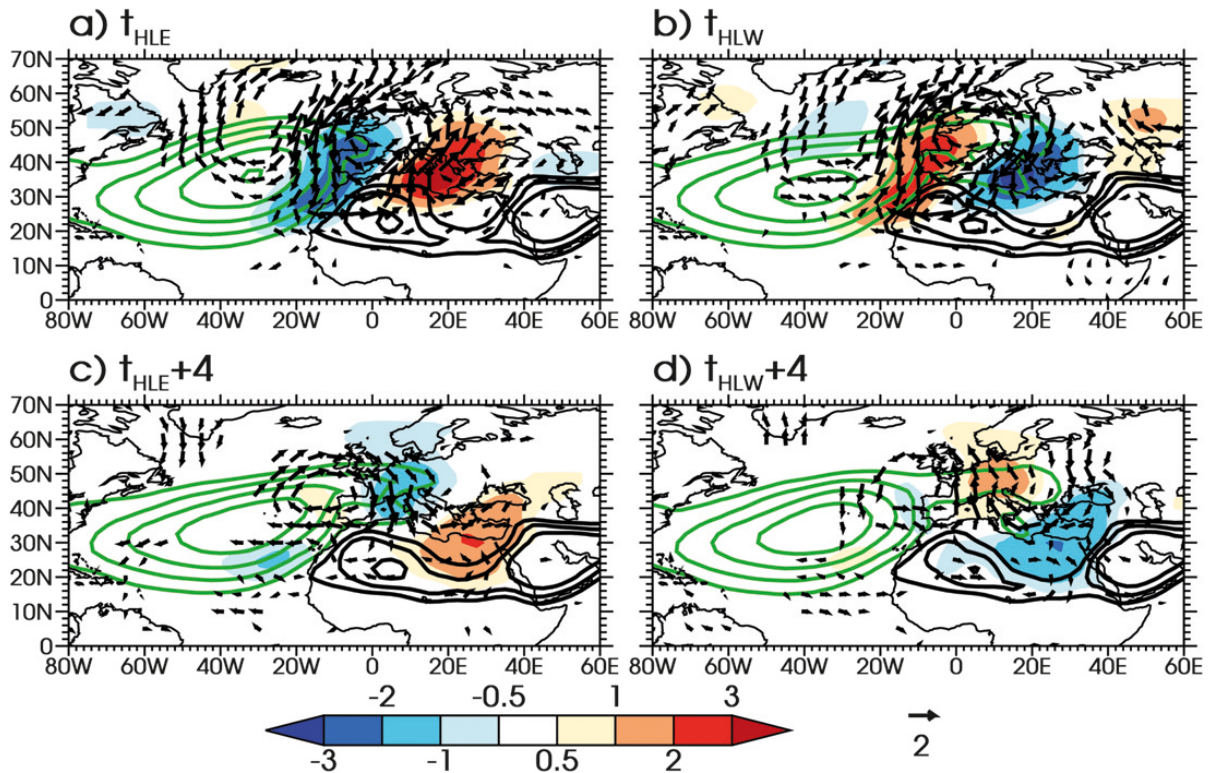


Figure 1.6.: Composite of the east (HLE) and west (HLW) phase of the SHL at 850 hPa. Shown are 10–60 days band-pass filtered potential temperature anomalies [K] (colored shading), wind anomalies [ms^{-1}] (vectors), reconstructed potential temperature [K] (black contour lines, interval 2 K, 38–42 K), reconstructed mean sea level pressure [hPa] (green contour lines, interval 2 hPa, 1016–1024 hPa). Reconstructed fields are calculated by adding band-pass filtered anomalies to climatological mean values. The beginning of HLE (a) and HLW (b) are shown in the upper row, conditions four days later in the lower row. Source: Roehrig et al. (2011).

On the intra-seasonal time scale the SHL shows variations in two frequency bands: 3–10 days and 10–30 days (Lavaysse et al. 2010). Variations in the 3–10 days band are mainly related to AEWs at the tropical flank of the SHL. The cold and moist air advected northward in the AEW troughs tends to weaken the SHL by reducing the temperature in the lower troposphere. The 10–30 days band is mainly related to upper-level waves at the extra-tropical flank. Chauvin et al. (2010) and Roehrig et al. (2011) identified and discussed two different phases of the SHL, referred to as Heat Low East (HLE) and Heat Low West (HLW). An HLE event is related to an upper-level trough crossing the African West coast and causing strengthened ventilation of the SHL over Mauritania and Morocco and weakened ventilation over Algeria and Libya. Stronger (weaker) ventilation in the west (east) is related to negative (positive) temperature anomalies (Fig. 1.6a); the SHL strengthens in the following days and is extended eastward (Fig. 1.6c). Opposite conditions are found for an HLW event (Fig. 1.6b), where a ridge at the west coast is causal to stronger ventilation from the Mediterranean Sea leading to a weakening and westward extension of the SHL (Fig. 1.6d). This weakening can be further amplified by cold surges over Libya into the Sahara (Vizy and Cook 2009; Chauvin et al. 2010; Lavaysse et al. 2010). An ex-

ceptional weak state of the SHL is possible when an AEW event in the south coincides with a cold surge in the north (Lavaysse et al. 2010). During the dry-season interactions with the extra-tropics are reported to decrease the pressure over the Sahara. These rather rare events (1–2 per dry season) are related to advection of warmer air in front of a far southward reaching trough at the African west coast and can cause precipitation in tropical West Africa (Knippertz and Fink 2008, 2009).

Variability on the synoptic time scale is as afore mentioned related to AEWs, which are also relevant in the pre-monsoon season (Couvreux et al. 2010). Another important mechanism is lee cyclogenesis down-stream of the Atlas Mountains related to eastward moving upper-level troughs. The falling pressure at the Saharan side of the mountain range can cause a northward extension of the SHL and consequent cold surges from the Mediterranean Sea, which counteract the falling pressure (Knippertz 2008). Cold surges are extreme manifestations of a more regular mesoscale phenomenon, the sea breeze front. Such fronts are part of the diurnal cycle and can directly affect the SHL in case they penetrate far enough inland, which is regularly the case for the so-called Atlantic Inflow over the Mauritanian coast. At day-time, dry convection in the Planetary Boundary Layer (PBL) hinders inland movement of the front, but at night-time it propagates up to 400 km inland until the first orographic barrier is reached (Grams et al. 2010).

Flamant et al. (2007) proposed a mechanism coined ‘Atlas-Hoggar Pumping’ to have an impact on the diurnal cycle of the SHL as well. The elevated terrain of Atlas and Hoggar Mountains (3000–4000 m) is in the morning located above the convective boundary layer in the surrounding. The elevated radiative heating in these areas results in convective plumes, which are expected to spread horizontally with consequent subsidence and reduced growth of the convective boundary layer in the SHL region in between both mountain ranges. This assumption is based on the analysis of the ECMWF and on a research flight in the framework of the AMMA project. The analysis for this particular day showed positive vertical motion over the Atlas Mountains up to about 8 km. The idea was repeated by Cuesta et al. (2009) and partially confirmed by Birch et al. (2012) in regional model experiments with a focus on the Saharan boundary layer and dust transport. Convective plumes above elevated terrain were found, but not the proposed subsidence in the SHL area.

Another atmospheric phenomenon related to the mountain ranges and affecting the ventilation in the SHL is the convective cold pool, which is in the focus of this study and discussed in the following section.

1.2. Convectively Generated Cold Pools

Deep convection is the result of unstable atmospheric conditions and plays a fundamental role in maintaining the heat balance of the tropical upper troposphere (Riehl and Malkus 1958). The two most relevant dynamical aspects of convection are the up- and downdrafts. The vertical stratification controls the strength and vertical extent of updrafts, or to be more precise, the depth of the layer where a pseudo adiabatically rising parcel is warmer than its environment. While rising, parcels convert their potential into kinetic energy. The maximum energy available for an idealized parcel was defined by Emanuel (1994) as **Convective Available Potential Energy (CAPE)**:

$$CAPE = \int_{p_{LFC}}^{p_{EL}} R_d(T_{vp} - T_{ve})d \ln p \quad (1.1)$$

where p_{LFC} is pressure at the **Level of Free Convection (LFC)** at which a parcel reaches saturation and starts to be warmer than its environment due to latent heat release, p_{EL} is the equilibrium level where a parcel has again the temperature of its environment and accordingly no more positive buoyancy, T_{ve} is the virtual temperature of the environment and T_{vp} the virtual temperature of the rising air parcel. **CAPE** does not take into account that air parcels are mixed with their environment during their ascent, which has significant effects (Zhang 2009). Nevertheless, **CAPE** is, due to its simple calculation, often used by forecasters to assess the likelihood of a convective event. It is reduced towards zero during the event and due to this property used as closure in some parametrization schemes for deep convection (e.g., Zhang and McFarlane 1995; Gregory et al. 2000).

As pointed out by Lafore et al. (2016), **CAPE** is almost always sufficiently high in tropical West Africa during the monsoon, the same is true for the **Column Water Vapor (CWV)**, which is often termed **Precipitable Water (PW)**, and is also a prerequisite for the development of deep convection. Conditions in northern Africa are different. Mean values of **CAPE** are comparably low there throughout the year (Riemann-Campe et al. 2009; Narendra Babu et al. 2010) and larger values are only occasionally reached; that also applies to the monsoon months May to September (Fig. 1.7). However, large values of **CAPE** alone are not enough to trigger convection, an air parcel has to overcome the **Convective Inhibition (CIN)** first. **CIN** is the energy necessary to reach the **LFC** starting from the surface, its calculation is analogous to Equation 1.1 except for integration boundaries, which are the surface and the **LFC**. Values of **CIN** are larger in subtropical northern Africa than in the tropics (Riemann-Campe et al. 2009), which makes, in combination with low values of **CAPE**, deep convection comparatively unlikely. The focus of this study is on the Atlas Mountains, they provide two mecha-

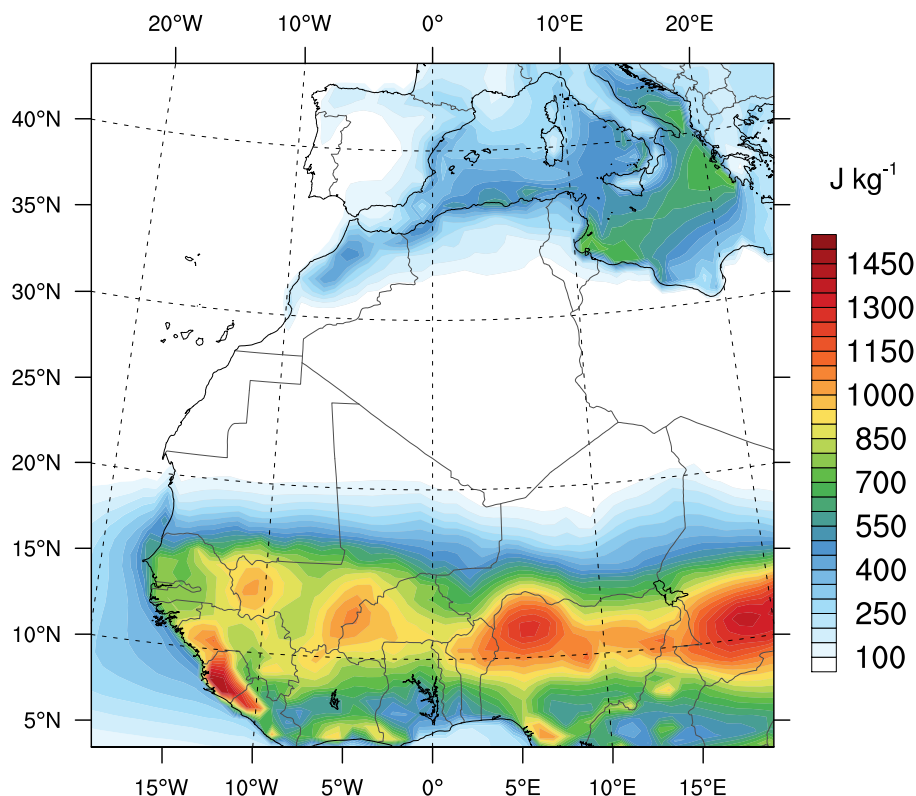


Figure 1.7.: Mean values of **CAPE** from ERA-Interim for the monsoon months May to September and the years 1979–2014, using 18 UTC time steps.

nisms to overcome large **CIN** values. On the one hand, this is orographic lifting, on the other hand, this is heating of elevated terrain.

Once updrafts are triggered, compensatory subsidence is required due to mass conservation. This downward motion may happen on different scales, ranging from intense microscale downdrafts (also called microbursts) with vertical velocities as high as 15 ms^{-1} (horizontal extent $< 1 \text{ km}$) to synoptic and planetary subsidence of only a few cm s^{-1} (Lafore et al. 2016). Located in between are convective downdrafts with horizontal extents of a few kilometers. They are fed by evaporative cooling of rain and cloud drops. Emanuel (1994) proposed a method for the calculation of the energy available for the creation of downdrafts called **Downdraft Convective Available Potential Energy (DCAPE)**. The calculation is again analogous to **CAPE**. Air parcels descend pseudo-adiabatically to the surface, which means they are cooled down by evaporation on their way. Like **CAPE**, **DCAPE** is merely a theoretical quantity. Its calculation contains uncertainties like the unknown start level, also the amount of precipitation available for evaporative cooling might be too small to keep the descending parcel saturated (Provod et al. 2015). Lafore et al. (2016) highlighted that, even in the presence of uncertainties, **DCAPE** is a useful tool for operational forecasters, as high values of **DCAPE** related to dry mid-level layers (700–500 hPa) increase the likelihood of downdrafts.

The cold air formed by evaporation and melting of precipitation below a convective cloud system behaves like a density current (e.g., [Simpson 1987](#); [Weisman and Rotunno 2004](#)). It descends to the ground and spreads out horizontally driven by the density difference to the warmer surrounding air. The speed of the leading edge can be estimated using the Froude number, which is the ratio of inertial and buoyancy forces (e.g., [Simpson 1987](#)):

$$U_f = k\sqrt{g'H} \quad (1.2)$$

where k is the Froude number, which is about 1 for atmospheric density currents, H is the depth, and $g' = g\Delta\rho/\rho$ is the so-called reduced gravity, where $\Delta\rho$ is the difference in density between the density current and its environment. In the atmosphere, additional aspects are of relevance for the spreading of the current. One is the radial spreading away from the convective cell, which leads to a reduced propagation speed of the front as the radius of the cylinder describing the flow is increased and its depth H accordingly decreased. This is more relevant for isolated events in areas without significant orographic constraints (like the example shown in [Fig. 2.3](#)), where the flow can spread into all directions unhindered. At the Atlas Mountains convective cells are often lined up along the ridge forming a more linear source.

Another aspect is the Coriolis force, which becomes increasingly important as the size of the density current increases. The relevant measure for this effect is the Rossby number $Ro = U/(Lf)$, where L is the length scale and f is the Coriolis parameter, the latter becomes dominant for $Ro \ll 1$. At 30°N , Ro falls below 1 for $L > 137$ km, with a propagation speed around 10 ms^{-1} , this is the case after 3.8 h of spreading away from the source. Thus, it is expectable to see the flow within the density currents south of the Atlas Mountains to become anti-cyclonically diverted during the night. [Hallworth et al. \(2001\)](#) found in water tank experiments and numerical simulations the maximal radius to be reached after a time of $t \approx 2/\Omega$, where Ω is the rotation rate of the reference system in rad s^{-1} . Accounting for the geographical latitude φ yields $t \approx 2/(\Omega\sin\varphi)$, which is approx. 15.2 h at 30°N and indicates that a density current initiated by late afternoon convection can grow throughout the night. [Roberts and Knippertz \(2014\)](#) call the applicability of this idealized approach to the real atmosphere into question. In a model experiment with the [Weather Research and Forecast \(WRF\)](#) model that successfully reproduced observations of an extremely large density current in the Sahel (~ 800 km), these authors found the theoretically maximal radius exceeded by at least a factor of 1.5. Possible reasons are not discussed, however, the said density current propagated into the cyclonic [SHL](#) area and was potentially deformed there in the ambient flow.

The air mass of such a density current is commonly called cold pool and is an inherent part of many convective systems, but typically the

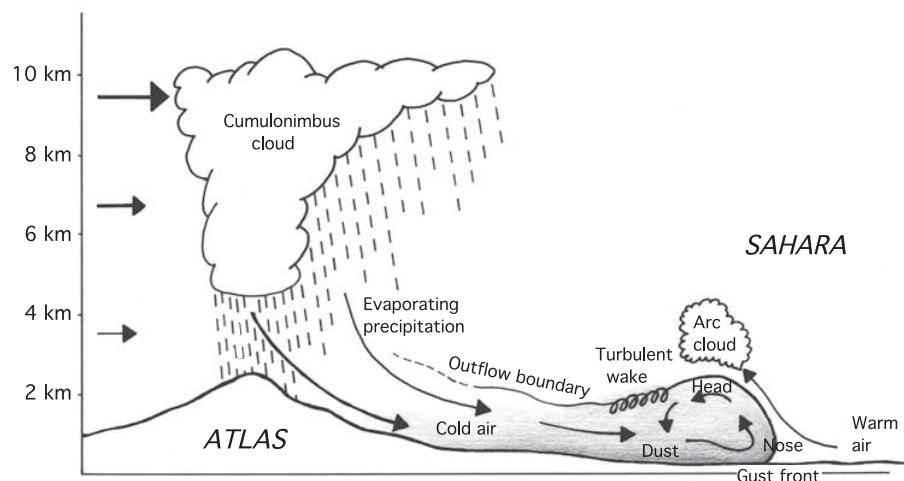


Figure 1.8.: Schematic of a convective cold pool originating from the Atlas Mountains. Source: Knippertz et al. (2007).

largest dimensions of this feature are observed in low-latitude arid or semi-arid regions. There, beside of a small Coriolis parameter, optimal conditions for the evaporation are provided by a deep, warm, and dry daytime convective boundary layer. A further enhancement of the evaporative cooling typically happens when vertical wind shear separates up- and downdrafts (Coniglio et al. 2006; Cohen et al. 2007; Roberts and Knippertz 2014). A horizontal extent of hundreds of kilometers, as in the example from Roberts and Knippertz (2014), and a depth of up to 3 km are not unusual and often reached by merging of several smaller cold pools (Knippertz et al. 2009a). The vertical structure including the wind shear of such an event is illustrated in Fig. 1.8.

The highly turbulent gust fronts of cold pools can lead to significant dust emissions and are then called haboobs³. Their occurrence is documented for many dry regions around the planet. Sutton (1925) and Farquharson (1937) were among the first who described the occurrence and characteristics of haboobs in the Sahelian part of the eastern African country of Sudan; more recent literature addressed the Sahel (e.g., Marsham et al. 2008; Williams 2008; Knippertz and Todd 2010; Marsham et al. 2013b), Northwest Africa (e.g., Knippertz et al. 2007; Emmel et al. 2010), the Middle East (e.g., Offer and Goossens 2001; Miller et al. 2008), the Gobi Desert in China (Takemi 2005), Australia (Strong et al. 2011), the Chihuahuan Desert between the US and Mexico (Rivera Rivera et al. 2010), and the Great Plains of the USA (Chen and Fryrear 2002). Many of these regions are uninhabited and events remain unrecognized, but from time-to-time haboobs gain public atten-

³Haboob: According to the glossary of the American Meteorological Society (AMS), the term 'Haboob' has an Arabic origin in the word 'habb', which means 'wind'. Sutton (1925) is given there as a first reference. Nowadays, it is used to describe thunderstorm outflow related dust storms around the world.



Figure 1.9.: Haboob hitting Phoenix (Arizona, USA) on 5 July 2011. Details of this event are discussed in [Raman et al. \(2014\)](#). Courtesy of Mike Olbinski (<http://www.mikeolbinski.com>).

tion when larger cities like Phoenix (Arizona, USA) are hit (e.g., [Raman et al. 2014](#), Fig. 1.9).

These large cold pool events have several important effects on their environment. Observational and modeling studies ([Marsham et al. 2013b](#); [Heinold et al. 2013](#)) show that up to half of the mineral dust emission in the Sahel and southern Sahara during the summer are caused by cold pools. [Marsham et al. \(2011\)](#) proposed an easy to use method to estimate the relative importance of different processes for the total mobilization of dust, the **Dust Uplift Potential (DUP)**:

$$DUP = vU^3 \left(1 + \frac{U_t}{U}\right) \left(1 - \frac{U_t^2}{U^2}\right) \quad (1.3)$$

where v is the fraction of bare soil, U the wind speed in 10 m, and U_t a threshold above which dust uplift takes place. [Marsham et al. \(2011\)](#) used a fixed threshold of $U_t = 7 \text{ ms}^{-1}$ for the Sahel, which was based on an analysis of **Meteosat-4 Infrared (IR)** images conducted by [Chomette et al. \(1999\)](#). The **DUP** itself is based on a parametrization for dust uplift ([Marticorena and Bergametti 1995](#)), but is a merely qualitative measure as the actual soil properties, e.g., the availability of dust or soil moisture, are not taken into account. The advantage is, that it is directly applicable to model output or observations of wind speed. Thus, it allows a ranking of meteorological processes with regard to their potential to mobilize dust decoupled from uncertainties in the description of soil properties. [Roberts and Knippertz \(2014\)](#) showed using **DUP** and the **WRF** model that the dust uplift related to a convective cold

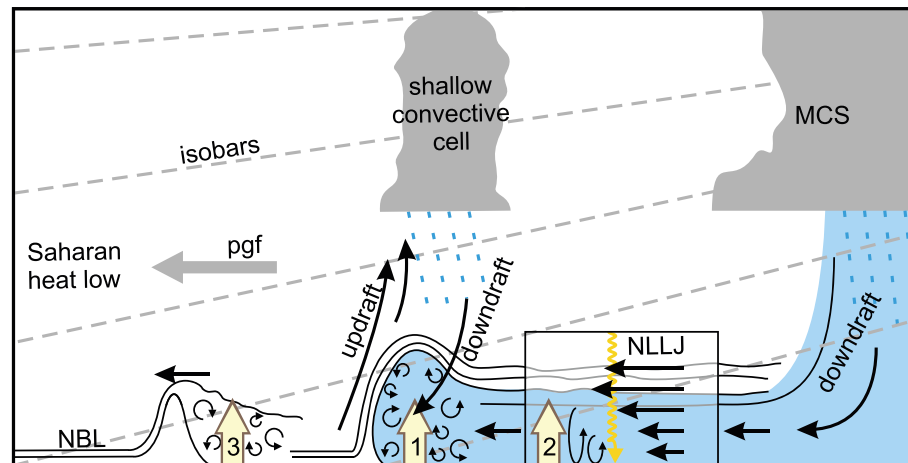


Figure 1.10.: Processes relevant for dust uplift related to a convective cold pool. (1) high wind speeds at the leading edge, (2) an enhanced NLLJ in the aged cold pool that is mixed downward in the morning, and (3) an internal bore in the night-time boundary layer. The 'pgf'-arrow indicates the pressure gradient force. Source: Roberts and Knippertz (2014), modified.

pool is caused by three meteorological processes: high wind speeds at the leading edge, a stronger Night-time Low-Level Jet (NLLJ) whose momentum is mixed downward in the morning, and an internal bore in the night-time boundary layer, which precedes the leading edge of the cold pool (Fig. 1.10). In a different application of the DUP, it has been shown that up to 25% of the annual dust uplift in most regions in northern Africa may be caused by very rare (on the order of one per year) high-wind events (Cowie et al. 2015).

Even without substantial dust emissions, cold pools are a serious threat for aviation due to rapid changes of wind shear between downdrafts of up to 10 ms^{-1} that feed the systems combined with updrafts of up to 6 ms^{-1} at the turbulent head (Goff 1976; Linden and Simpson 1985). The updrafts are created by lifting of warm air above the head of the density current, a process which can lead to arc cloud formation and that is also involved in storm propagation by triggering of new convective cells (Goff 1976). Indeed, cold pools are a key factor for the organization of single cells into larger MCSs and their movement, as pointed out by Zipser (1977) and later confirmed by many others (e.g., Corfidi 2003; Weisman and Rotunno 2004). Recently, large-scale effects of cold pools from Sahelian squall lines on the WAM system have been highlighted by Marsham et al. (2013a). This study also shows that cold pools form a significant part of the low-level northward moisture flux in the WAM and of the ventilation of the SHL.

The fundamental physics behind cold pool generation by density currents are well understood and were discussed in detail decades ago (e.g., Simpson 1987). However, today's climate models still show significant uncertainties for projected changes in the WAM (Xue et al. 2010; Druyan 2011) and other monsoon regions (Christensen et al.

2013) regularly affected by convective cold pools. One major reason for the fact that these models are unable to create realistic cold pools is the usage of parameterizations of deep convection (Heinold et al. 2013; Marsham et al. 2013a). Related effects such as dust emission and modification of the monsoon flow can then further contribute to uncertainties and model errors. For example, the models used for the Fifth Assessment Report of the Intergovernmental Panel on Climate Change (IPCC) all tend to underestimate dust emission over Northwest Africa (Evan et al. 2014).

So far, only few studies on climatological aspects exist. The first historical report from Sudan contained an eight-year climatology of haboobs observed in Khartoum (24.5 cases per year; Sutton 1925); Engerer et al. (2008) analyzed eight years (only April to August) of station and radar data from Oklahoma, USA; Provod et al. (2015) analyzed data from one monsoon season and one station in Niamey, Niger; Emmel et al. (2010) identified cold pools over the Northwest African Atlas Mountains based on a subjective and labor-intensive manual inspection of station data and infrared satellite images.

1.3. Objectives and Structure of This Study

As mentioned in the introduction and in section 1.1, with the current state of research three important pathways of ventilation for the summertime SHL are known, which introduce variability on the sub-monthly time-scale: (a) In the south, the AEWs with their monsoon surges and convective cold pools from MCSs. Both the AEWs and the MCSs are very frequent and thus important for the state of the SHL. (b) In the north, cold surges from the Mediterranean Sea related to upper-level troughs and lee cyclogenesis. Such events are less frequent than AEWs and due to their large scale synoptic forcing easier to reproduce by numerical models. (c) In the west, the Atlantic inflow modulates the SHL.

The present study aims to assess an additional possible pathway: convectively driven cold pools originating from the Atlas Mountains. Fig. 1.11 gives a schematic overview of the processes mentioned before and the one proposed here. The assessment is divided into two parts. Firstly, the regularity of cold pool events in Northwest Africa is addressed by the creation of a multi-year climatology. It is known that weather and climate models with a coarse horizontal resolution struggle to reproduce them (see section 1.2), but so far it is not known whether these events are regular enough to have a significant impact on the SHL. In the second part, the WRF model is used to analyze the impact of cold pool events on the SHL by means of two case studies. This study is part of the project titled 'Multi-scale subtropical controls on the position and intensity of the summertime West African heat low'.

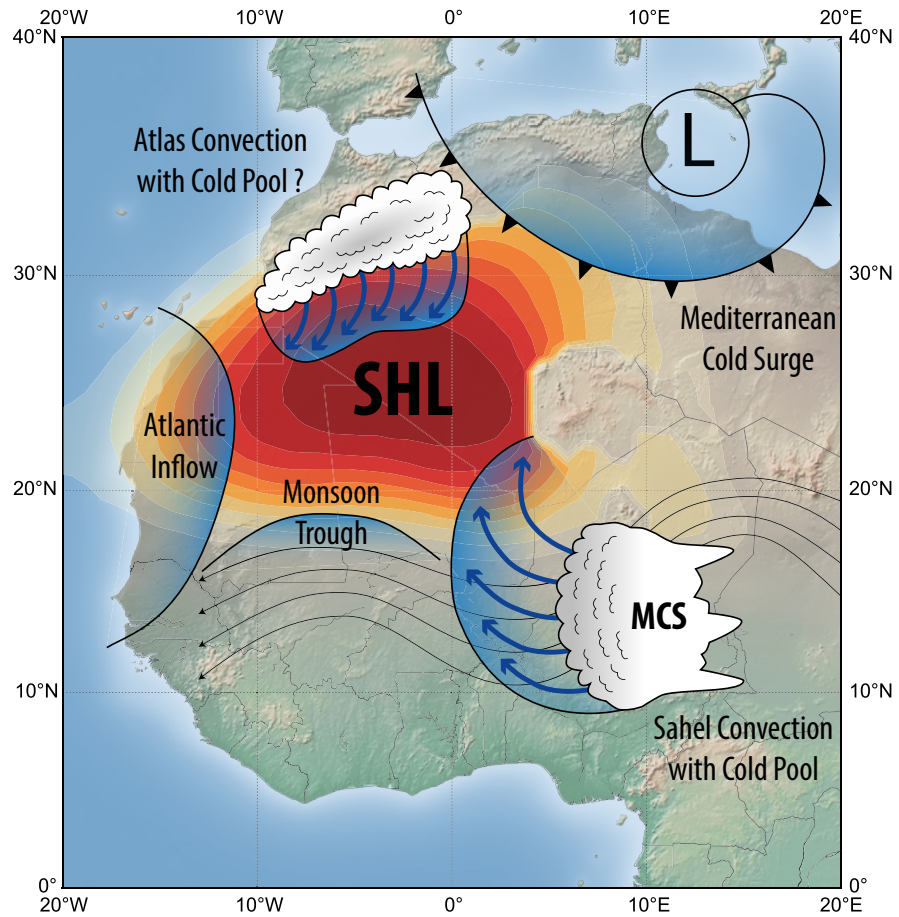


Figure 1.11.: Processes relevant for the variability of the SHL on the sub-monthly time scale. Included are the position of the SHL in August (cf. Fig. 1.3), streamlines of the AEJ with an MCS in a realistic position relative to the AEW, the monsoon trough, the Atlantic inflow, cold surges from the Mediterranean, and convection over the Atlas Mountains, which is proposed to be relevant as well.

The project was funded by the German Science Foundation (DFG) and associated with the UK and French Fennec initiatives.

In the first part, a new objective method suitable to create multi-year climatologies of cold pool events based on station observations of standard meteorological variables combined with microwave satellite data is presented. Given the role of convectively generated cold pools for monsoonal heat low ventilation and moistening from the south, dust emissions, and severe convective storm generation, there is a clear need for automated algorithms of this kind beyond the scope of this study. The algorithm depends on freely available data only and is therefore applicable to all relevant regions worldwide. It is objective in the sense that individual case decisions are based on fixed thresholds and thus are reproducible. Though the thresholds have been selected for an application to northern Africa, they can be adapted to fit to others regions. The method is based on Emmel et al. (2010), but extends the work, especially the labor-intensive manual inspection of IR satellite im-

ages used there is replaced by an automated screening for convection of microwave satellite data.

The second part benefits from the unique co-existence of two [AWS](#) networks at the Saharan foothills of the High Atlas Mountains and the western Sahara in 2011 and 2012. Two convective periods in June 2011 and 2012 identified by the automated algorithm presented in the first part are simulated using the [WRF](#) model with a horizontal resolution of 3 km, which enables to explicitly resolve convection. In both cases cold pools with a horizontal extent of several hundred kilometers are observed in satellite imagery. The aim of this part is to assess the meso- to synoptic-scale impacts of such systems on surface pressure, moisture transport, and surface radiation balance in the northern [SHL](#) region. In addition, the influence of a reduction of horizontal resolution and the usage of parameterized convection is analyzed for one of the events to illustrate possible effects in climate simulations.

The text is organized as follows: All datasets used in the following chapters are described in chapter 2. The cold pool detection algorithm as well as the experimental setup for all [WRF](#) simulations are in chapter 3. Results are split into the cold pool climatology in chapter 4 followed by the case studies performed with [WRF](#) in chapter 5. Findings of both parts are summarized and discussed in chapter 6.1 and 6.2 and an outlook on possible further investigations is given in chapter 6.3.

2. Data

Northwest Africa is in general a data-sparse region, this is especially true for the region south of the Atlas Mountains as most of the synoptic weather stations are located along the northern coast line. Only a few stations are in the Saharan desert and most of them do not report regularly (Fig. 2.1, section 2.3). This lack of data not only hampers scientific investigations, but also affects negatively the reliability of operational forecasts. In this study, it was possible to take advantage of two research projects, both of which addressed the data availability issue by deployment of [AWSs](#), described in sections 2.1 and 2.2. In the first part of this study, these ground observations were combined with microwave satellite measurements (see section 2.5) to create a climatology of convective cold pool events. In the second part, two cases from the climatology were simulated with initial and boundary conditions from the [European Centre for Medium-Range Weather Forecasts](#)

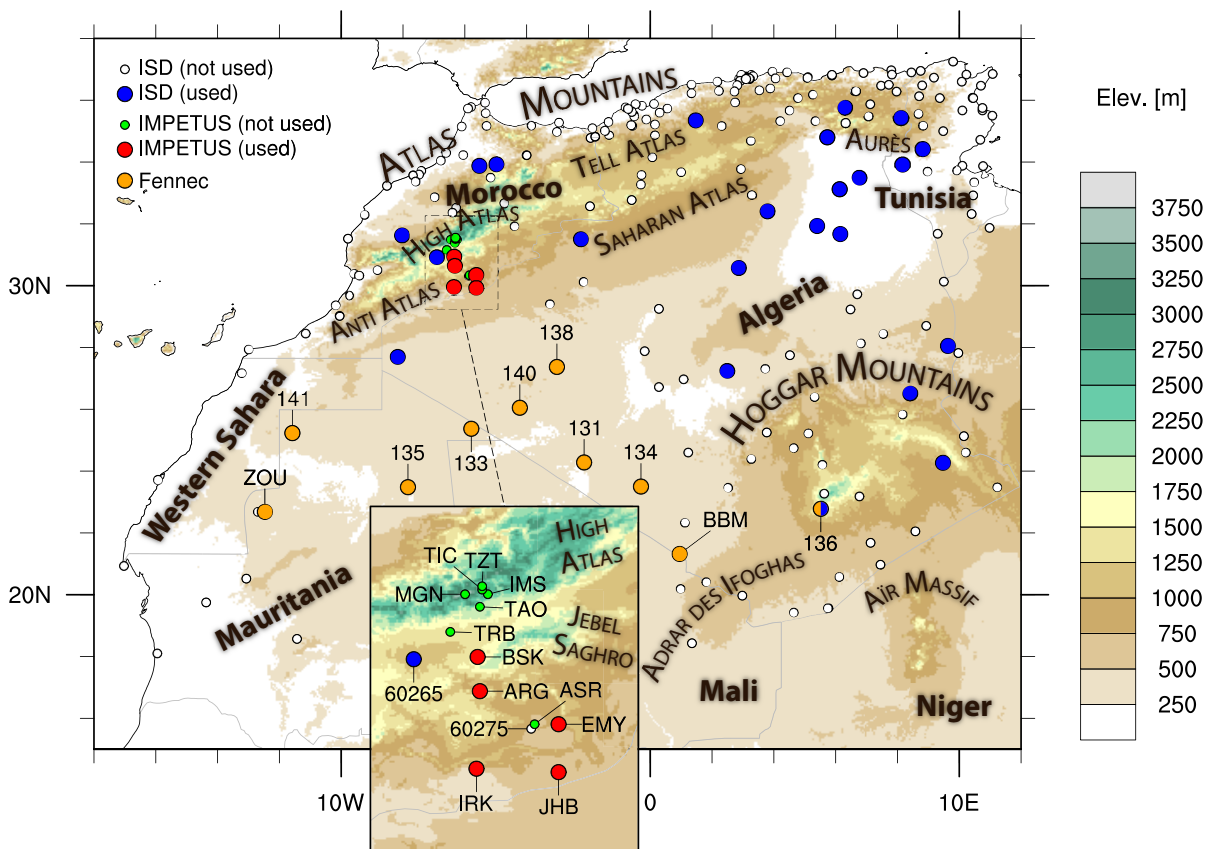


Figure 2.1.: Geographical overview of Northwest Africa including locations of ISD, IMPETUS, and Fennec weather stations.

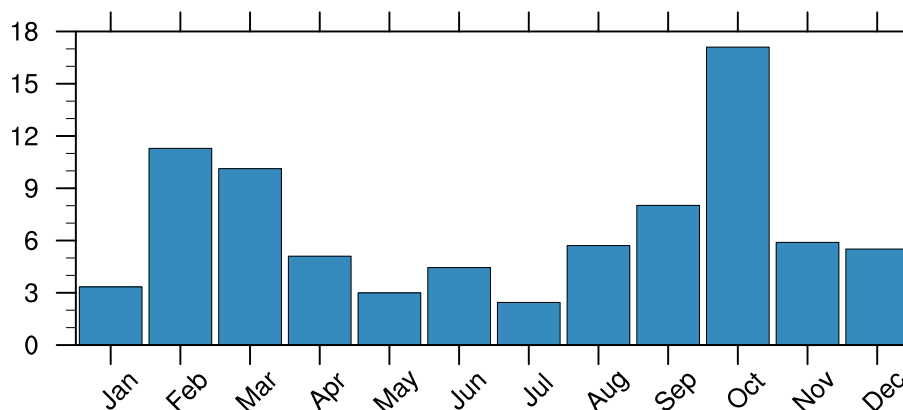


Figure 2.2.: Annual cycle of the precipitation for the stations ARG, BSK, EMY, IRK, and JHB. The years 2002–2011 are included in the calculation.

(ECMWF, see section 2.6) operational analysis. Infrared satellite measurements (see section 2.4) were used in model evaluation.

2.1. IMPETUS Station Network

Like Emmel et al. (2010), who created a first climatology for five years (2002–2006), the current study benefits from a dense network of AWSs deployed in late 2001 and maintained until 2010 by the *Integrated Approach to the Efficient Management of Scarce Water Resources in West Africa (IMPETUS)* project (Speth et al. 2010) in southern Morocco. The maintenance of these stations was extended by the DFG-funded project in which this thesis was embedded to cover the Fennec *Intensive Observation Periods (IOPs)* in June 2011 and 2012. The actual work in Morocco was done by Julie Berckmans and Philipp Aben. The AWSs

Table 2.1.: Location of IMPETUS stations and data availability for the period 2002–2012

<i>Name</i>	<i>Abbr.</i>	<i>Lon</i>	<i>Lat</i>	<i>Elev.</i>	<i>Avail.</i>
Arguioun	ARG	6.32°W	30.65°N	1020 m	70.1 %
Asrir	ASR	5.84°W	30.36°N	750 m	79.7 %
Bou Skour	BSK	6.34°W	30.95°N	1420 m	98.5 %
El Miyit	EMY	5.63°W	30.36°N	792 m	95.5 %
Imeskar	IMS	6.25°W	31.50°N	2245 m	86.0 %
Lac Iriki	IRK	6.35°W	29.97°N	445 m	93.1 %
Jebel Brâhim	JHB	5.63°W	29.94°N	725 m	58.4 %
M’Goun	MGN	6.45°W	31.50°N	3850 m	94.8 %
Taoujgalt	TAO	6.32°W	31.39°N	1900 m	79.9 %
Tichki	TIC	6.30°W	31.54°N	3260 m	79.1 %
Trab Labied	TRB	6.58°W	31.17°N	1383 m	91.0 %
Tizi-n-Tounza	TZT	6.30°W	31.57°N	2960 m	53.4 %

were equipped with instruments for air temperature and humidity, soil temperature and humidity, global and net radiation, wind speed and direction, and precipitation. Data from twelve stations are available from 2002 until 2012. They are located in the basins of the rivers Dadès and Drâa and cover parts of the M'Goun Mountain Massif in the High Atlas and the Jebel Saghro mountain range that belongs to the Anti Atlas mountain range (Fig. 2.1; Table 2.1). The stations were intended to cover the gradient from the semi-arid High Atlas to the arid pre-Saharan landscapes (Schulz 2008). The resultant arrangement makes them very well suited for the observation of cold pool events originating from convection over the High Atlas and propagating down-hill towards the Sahara.

Five stations have been selected here for the climatology because of their location south of the High Atlas and their data availability. These stations are Bou Skour (BSK), Arguioun (ARG), El Miyit (EMY), Jebel Brâhim (JHB), and Lac Iriki (IRK) (red markers in Fig. 2.1). The annual cycle of precipitation for these stations has two maxima, in spring and autumn respectively (Fig. 2.2). The year 2012 is only available until the second half of September, when the stations were dismantled. The average distance from one station to its closest neighbor is 46 km. The measurement intervals of these stations differ between 10 and 15 min. For the sake of easier processing all measurements were interpolated linearly to 5 min intervals. This dataset was used for the cold pool climatology (chapter 4) as well as for the model evaluation (chapter 5).

2.2. Fennec Station Network

The Fennec project (Washington et al. 2012) installed and maintained ten stations in Algeria, Morocco, and Mauritania (Hobby et al. 2013, orange markers in Fig. 2.1, Table 2.2). This includes two super-sites, Zouérat (ZOU) in Mauritania and Bordj Badji Mokhtar (BBM) in Algeria, as well as eight additional AWSs. Details about the full instrumentation of the super-sites can be found in Marsham et al. (2013b) and Todd et al. (2013). Here, only the AWSs are used. They offer measurements of air temperature and humidity, up- and down-welling short- and long-wave radiation, and pressure with a temporal resolution of 1 s at the super-sites and of 3:20 min at the additional AWSs. The stations are partially located in very remote areas in the central Sahara and were deployed with the support of the national meteorological offices of Algeria and Mauritania. The data were automatically transmitted using Iridium Router-Based Unrestricted Digital Internetworking Connectivity Solutions (RUDICS), which is a satellite based data transfer service.

These ground observations were intended to complement the Fennec aircraft campaigns in 2011 and 2012. The AWSs were not disman-

Table 2.2.: Location of Fennec AWSs and average data availability for the months June 2011 and June 2012. ¹Availability for Zouérat refers to 2011 only, the station was not operated in 2012.

<i>Name</i>	<i>Abbr.</i>	<i>Lon</i>	<i>Lat</i>	<i>Elev.</i>	<i>Avail.</i>
131 Blue	131	2.14°W	24.28°N	259 m	58.3 %
133 Yellow	133	5.79°W	25.37°N	336 m	35.9 %
134 Black	134	0.30°W	23.50°N	324 m	95.7 %
135 White	135	7.84°W	23.48°N	315 m	49.8 %
Tamanrasset	136	5.52°E	22.78°N	1378 m	71.5 %
138 Grey	138	3.02°W	27.37°N	375 m	96.4 %
140 Orange	140	4.22°W	26.05°N	379 m	54.2 %
141 Purple	141	11.58°W	25.23°N	336 m	44.7 %
Bordj Badji Mokhtar	BBM	0.95°E	21.32°N	398 m	77.0 %
Zouérat ¹	ZOU	12.47°W	22.68°N	590 m	75.3 %

tled, but their data availability after 2012 is very low as no maintenance has taken place afterwards. Accordingly, the dataset is too short for the creation of a climatology and was here not used for this purpose. But it is very valuable for the model evaluation of the two case studies described in chapter 5. For the 2012 case, data from all stations but the super-site Zouérat are available, which was not operated in 2012. Due to technical issues, only data from 6 stations are available for the 2011 case.

2.3. SYNOP and METAR

Standard surface synoptic observations (SYNOP, format FM-12) and Aerodrome routine meteorological reports (METAR, format FM-15), both routinely collected and distributed via the Global Telecommunication System (GTS) of the World Meteorological Organization (WMO) and described in WMO (2010), are valuable sources of information and available worldwide. However, the station density in Northwest Africa is relatively low compared to other regions of the world. Here not raw reports but the quality controlled Integrated Surface Database (ISD; Smith et al. 2011) compiled by the National Climatic Data Center (NCDC) is used¹. This dataset mainly contains hourly, but also a number of half-hourly observations. For the entire region of interest (Fig. 2.1), 224 stations are available. Because of their reporting frequency not all of these stations are suitable for the creation of a climatology. Only those with a data availability of more than 80% with respect to hourly observations for the period 2002 to 2014 have been

¹The ISD station dataset was obtained from NCDC (<ftp://ftp.ncdc.noaa.gov/pub/data/noaa>)

selected. For the creation of the cold pool climatology, stations with a distance of less than 100 km from the coastline have been removed to avoid detection of sea breeze fronts, which are technically also density currents and can have characteristics very similar to convectively driven cold pools. The remaining dataset contains 23 stations (blue markers in Fig. 2.1) with an average distance from one station to its closest neighbor of 184 km. Like the [IMPETUS AWS](#) data, these observations were also interpolated linearly to 5 min intervals and used for the cold pool climatology (chapter 4) as well as for model evaluation (chapter 5).

2.4. Meteosat SEVIRI 'Desert Dust' Product

The [Meteosat Second Generation \(MSG\)](#) satellites are jointly operated by the [European Organisation for the Exploitation of Meteorological Satellites \(EUMETSAT\)](#) and the [European Space Agency \(ESA\)](#). They are located in geostationary orbits approx. 36,000 km above the equator. The first of these satellites ([MSG-1, Meteosat-8](#)) was launched in 2002 and became operational in 2004. It was followed in 2005 by [MSG-2 \(Meteosat-9\)](#) and in 2012 by [MSG-3 \(Meteosat-10\)](#). The last satellite in this series is [MSG-4 \(Meteosat-11\)](#) launched in 2015. Figures shown in this thesis are created from data² of [MSG-2](#), which was during the investigated cases located at 0.0°E and later relocated to 9.5°E. At the time of writing, the 0.0°E position is occupied by [MSG-3](#). The satellites are spin-stabilized by a continuous rotation around their own axis with a speed of 100 rpm and the axis is aligned to the rotational axis of the earth.

The primary instrument is the [Spinning Enhanced Visible and InfraRed Imager \(SEVIRI\)](#), a line-by-line scanning passive radiometer with three visible, one near infrared, and eight thermal infrared channels. It scans one line with each rotation of the satellite; a full image contains 3712 lines. This results in a spatio-temporal resolution of 15 min and 3 km at nadir, which makes [SEVIRI](#) data suitable for a wide range of applications ([Schmetz et al. 2002](#)). [Lensky and Rosenfeld \(2008\)](#) describe a number of useful RGB-composites³ based on several channels, including the 'Desert Dust' product employed here. In this product, the [BTDs](#) measured by the 12.0 and 10.8 μm channels ($\text{BTD}_{12.0-10.8}$), which indicates the opacity of clouds, is mapped to red. $\text{BTD}_{10.8-8.7}$ is mapped to green; the 8.7 μm channel is sensitive to the size of uplifted quartz

²Data was obtained from the Earth Observation Portal (<https://eoportal.eumetsat.int>).

³RGB-composites: For the creation of [Red-Green-Blue \(RGB\)](#)-composites values of three or more channels are combined into one image. For this purpose each [Brightness Temperature \(BT\)](#) of one channel or the [Brightness Temperature Difference \(BTD\)](#) of two channels is mapped to one of the colors red, green, or blue. The three color channels are then combined to one image.

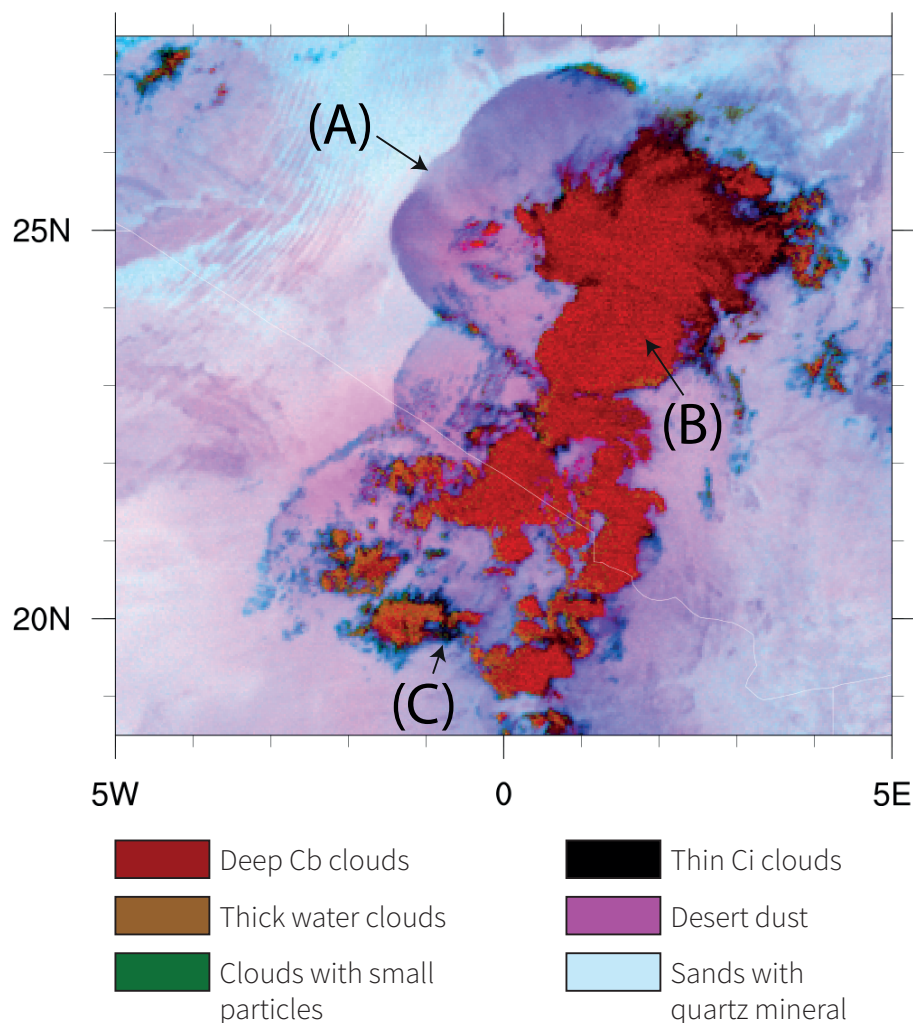


Figure 2.3.: Example for Meteosat SEVIRI 'Desert Dust' product. Capital letters indicate important features: (A) cold pool with uplifted dust, (B) deep convective clouds, and (C) cirrus clouds.

mineral particles. The brightness temperature in the 10.8 μm window channel is mapped to blue and indicates cloud top and surface temperature.

The 'Desert Dust' images are used in chapter 5 to illustrate the evolution of selected cold pool events. Their most important features are labeled with capital letters in Fig. 2.3. Cold pools are visible due to dust uplift by pinkish colors (A). This characteristic has been used by several studies investigating cold pool events in Northwest Africa (e.g. Marsham et al. 2013b; Allen et al. 2013; Bou Karam et al. 2014). However, this is only possible in the absence of higher level clouds and it is to be expected that events are missed when relying on infrared images (Ashpole and Washington 2013; Kocha et al. 2013). This is further supported by Heinold et al. (2013) who showed that up to 90% of cold pool related dust emission in high-resolution model simulations is at least partly covered by clouds. Also, an increased amount of CWV, which is one of the effects of a cold pool, can hinder the detection of uplifted

dust (Brindley et al. 2012). Clouds with a large vertical extend, like Cb, appear in red (B) and thin cirrus clouds in black (C).

2.5. AMSU-B and MHS Microwave Data

To avoid problems with high-level clouds and increased CWV, the cold pool climatology algorithm makes use of microwave satellite data, namely the Advanced Microwave Sounding Unit-B (AMSU-B) on-board National Oceanic and Atmospheric Administration (NOAA)-15, -16, and -17 satellites as well as the Microwave Humidity Sounder (MHS) which is the successor of AMSU-B on-board NOAA-18, -19, MetOp-A and -B. As the name already betrays, the NOAA satellites are operated by NOAA; the MetOp-satellites by EUMETSAT in cooperation with NOAA. NOAA-15, which is the first to carry the AMSU-B instrument, was launched in 1998, NOAA-16–19 followed in 2000, 2002, 2005, and 2009. MetOp-A was launched in 2006, MetOp-B in 2012, MetOp-C is at the time of writing scheduled for 2018.

All these satellites are polar-orbiting with periods of approx. 100 min. Both instruments have two window channels, 89 GHz and 150 GHz (AMSU-B) or 157 GHz (MHS), and three channels at the 183.3 GHz water vapor absorption line. For AMSU-B these channels are 183.3 ± 1 , ± 3 , and ± 7 GHz, for MHS 183 ± 7 GHz is replaced by 190 GHz. Both instruments are designed as cross track line-scanned radiometers with an antenna beamwidth of approx. 1.1 degrees. Together with the nominal altitude of 850 km (AMSU-B) and 870 km (MHS) this translates to a nadir resolution of 16.3 km (AMSU-B) and 17 km (MHS). The swath width⁴ for both is approximately 2200 km. These instruments are able to reliably detect deep convection (Burns et al. 1997; Bennartz and Bauer 2003; Hong 2005). An example from June 2011 illustrates the advantage of the microwave instruments: the infrared image (Fig. 2.4a, 'Desert Dust' product) shows high-level clouds in a wide region over the Atlas Mountains, while on the microwave brightness temperature images (Figs. 2.4b–d) the cores of the convective systems are clearly visible. For the region of interest, 106,582 satellite overpasses (approximately 0.7 TB of data) were selected for the period 2002 to 2014, which corresponds to 22 overpasses per day on average. However, the number of overpasses per year is not constant since the number of satellites has changed over time. The smallest number of overpasses is available for 2002 (11.3 overpasses per day), the largest number for 2013 (28.7 overpasses per day).

⁴Swath width and resolution differ slightly from satellite to satellite as not all of them fly at the nominal altitude.

2. Data

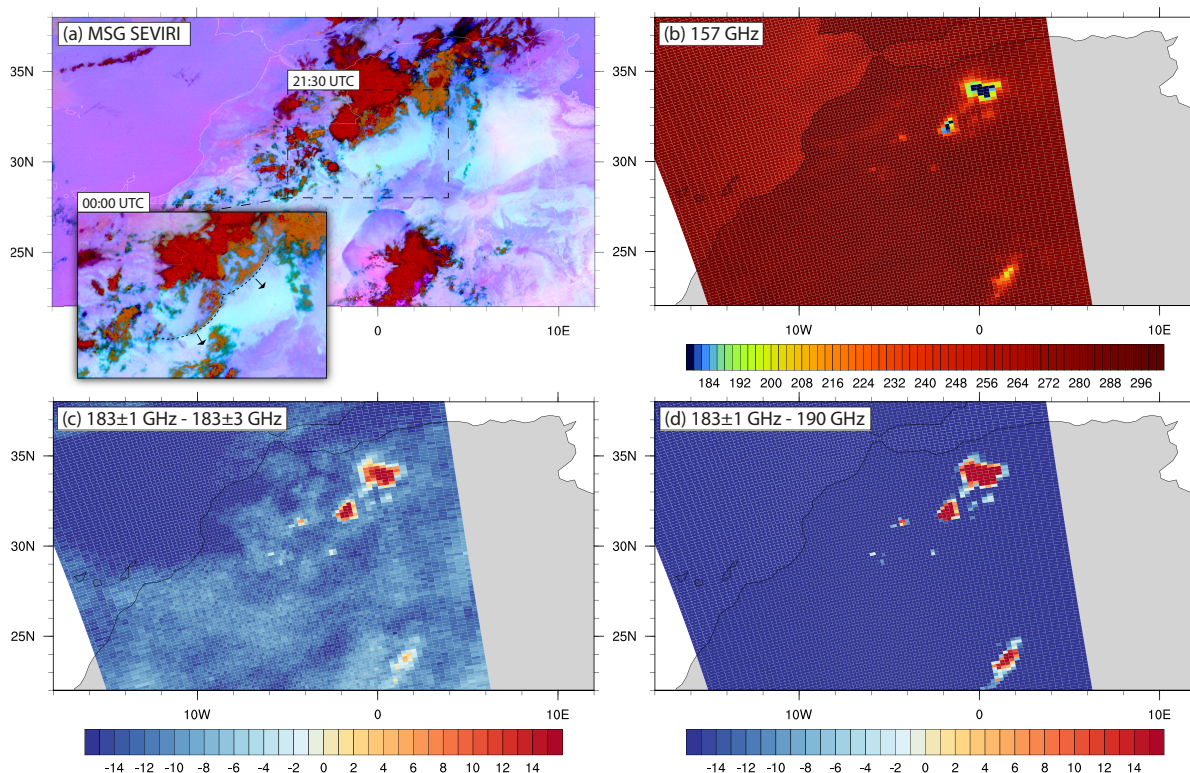


Figure 2.4.: Comparison of infrared and microwave data for a cold pool event on 21 June 2011: (a) Meteosat SEVIRI 'Desert Dust' product at 2130 UTC (whole area) and 0000 UTC (elevated detail, dashed lines and arrows indicate leading edge of cold pool and direction of propagation); (b–d) data from MetOp-B overpass at 2121 UTC; (b) brightness temperature of the 157 GHz channel; (c) difference between brightness temperature of the 183 ± 1 and 183 ± 3 GHz channels; (d) difference between brightness temperature of the 183 ± 1 and 190 GHz channels. Source: Redl et al. (2015)

Data were obtained as raw instrument counts (level 1b) from the NOAA Comprehensive Large Array-Data Stewardship System (CLASS)⁵ and converted to brightness temperatures (level 1c) using the ATOVS and AVHRR preprocessing package (AAPP; Labrot et al. 2011). This conversion also includes a correction for Radio Frequency Interference (RFI), which is especially crucial for NOAA-15 (Atkinson 2001).

Products using data from space-borne radar instruments, like those aboard the TRMM and Global Precipitation Measurement (GPM) satellites, were not taken into account due to their lower spatio-temporal coverage. This lower coverage is caused by the smaller number of satellites combined with smaller swath widths. Moreover, blended rainfall products derived from these and other satellites incorporate infrared measurements with the flaws mentioned above, rendering these gridded products inadequate for the task of convection screening.

⁵CLASS web page: <http://www.nsof.class.noaa.gov>

2.6. ECMWF (Re)-Analysis Data

The operational analysis of the [European Centre for Medium-Range Weather Forecasts \(ECMWF\)](#) serves as initial and boundary condition for all WRF model runs. Data for the first case in 2011 are from the [Integrated Forecast System \(IFS\)](#) cycle⁶ 37r2, data for the second case in 2012 from cycle 38r1. Changes between these cycles include the assimilation of additional satellite data and an updated convection scheme. The horizontal resolution of T1279 (approx. 0.14°) and the number of vertical layers (91) did not change. Data were obtained at a 6-hourly temporal resolution.

In addition to the operational analysis the re-analysis ERA-Interim ([Dee et al. 2011](#)) is used. It provides information about the climatological state of the SHL in chapter 1 and is included for comparison in some figures shown in chapter 5. ERA-Interim is created with the cycle 31r2 and updated regularly. The resolution is T255 (approx. 0.75°) in horizontal and 60 layers in vertical direction. Required fields of both datasets were obtained from [ECMWF's Meteorological Archival and Retrieval System \(MARS\)](#).

⁶ECMWF Model Cycles: The [ECMWF](#) calls the versions of its forecast system 'cycles'. Detailed information about changes between cycles are listed on their web page: www.ecmwf.int.

3. Methods

This chapter is divided into two sections. At first in section 3.1, the algorithm for the creation of cold pool climatologies is described, these methods are published in Redl et al. (2015). This is followed in section 3.2 by a description of the WRF model, modification of the model, and the experimental setup for the case studies, these methods are published in Redl et al. (2016).

3.1. Objective Cold Pool Detection Algorithm

The objective cold pool detection algorithm consists of three steps: (a) preselection of cases based on station data; (b) grouping of contemporaneous cases from multiple stations into single events; (c) confirming the existence of a nearby convective system based on microwave satellite data.

3.1.1. Ground Observation Screening

In the first step, station data is screened for typical characteristics of the leading edge of a convectively generated cold pool. In general, these characteristics are high horizontal wind speeds, high Turbulent Kinetic Energy (TKE), increase in surface pressure, decrease of temperature, and increase in dew point temperature (e.g. Knippertz et al. 2007; Engerer et al. 2008). As in Emmel et al. (2010), only the most stable, and with the selected data sources available indicators, which are mean horizontal wind speed (v_{mean}) and increase in dew point temperature (ΔT_d), are ultimately used (an example case is shown in Fig. 3.1). The selected thresholds are $\Delta T_d \geq 4$ K in 30 min and $v_{mean} \geq 4$ ms⁻¹ in the following hour. In addition to these thresholds, another requirement is no precipitation ± 1 h around the detected jump in T_d , since rainfall near the station can increase T_d in the absence of a convective cold pool event. Ignoring stations that are directly affected by rain does not hinder the detection of large events, as they usually affect multiple stations. However, the absolute number of cases detected in data from the IMPETUS stations is reduced by about 32% due to this criterion. The above-described thresholds are identical to those chosen in Emmel et al. (2010) and based on case studies of cold pool events south

3. Methods

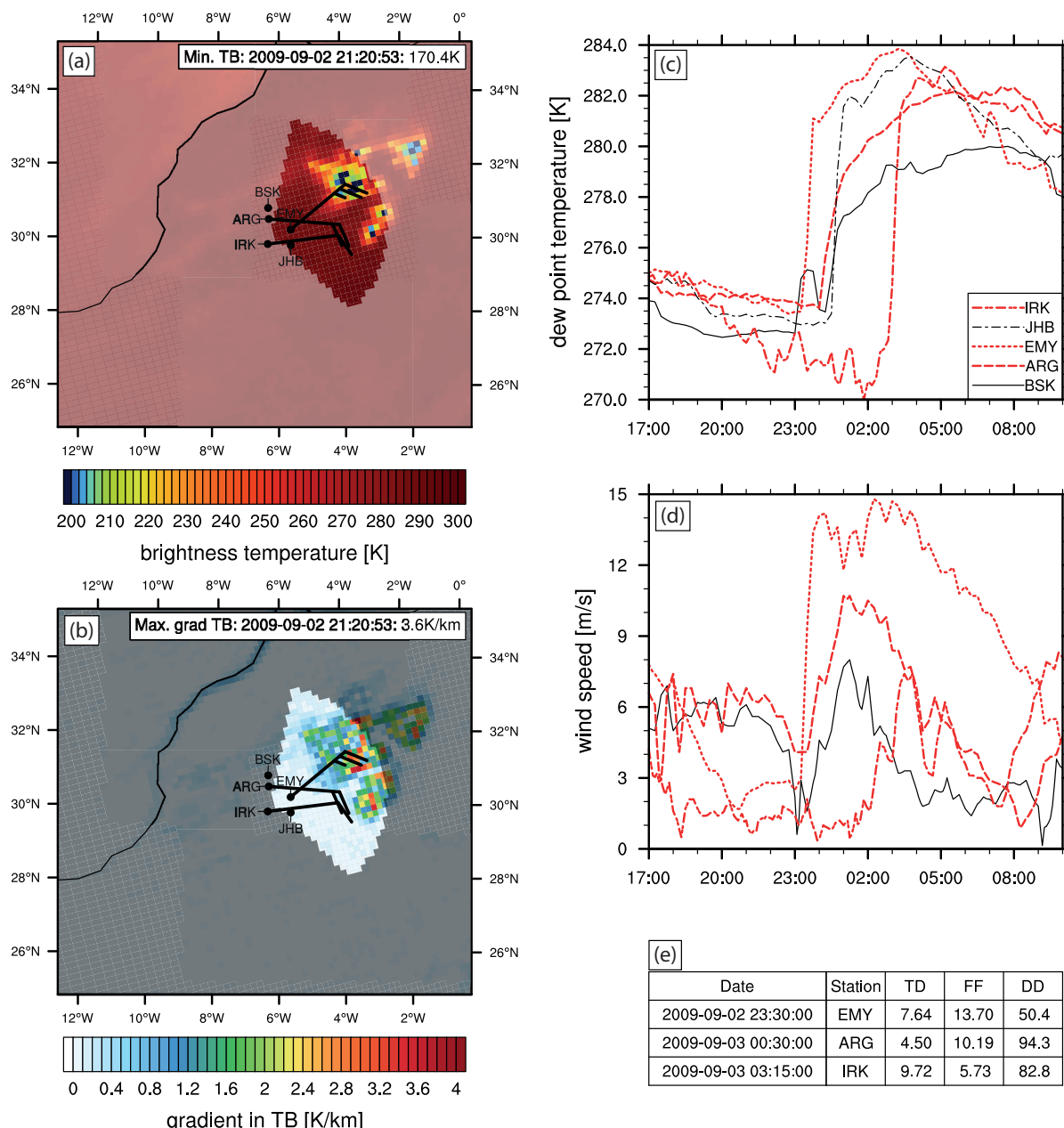


Figure 3.1.: An example case detected by the automated algorithm in ground observations from the **IMPETUS** station network (Fig. 2.1; Table 2.1) and satellite observations from MetOp-B in September 2009: (a) brightness temperatures measured in the 157 GHz channel; (b) horizontal gradient in brightness temperatures of the 157 GHz channel; (c) dew point temperature measured by **AWSs**; (d) wind speed measured by **AWSs**, JHB is not included due to an instrument failure at this time; red color in c and d indicate fulfilled criteria; (e) overview of measured values in tabular form (only stations that fulfill the criteria, TD = increase in dew point temperature, FF = mean wind speed in the hour following the dew point increase, DD = mean wind direction in the hour following the dew point increase). The wedge-shaped brighter areas in (a) and (b) indicate the pixels used by the algorithm for convection screening. Source: [Redl et al. \(2015\)](#).

of the Atlas Mountains ([Knippertz et al. 2007](#)). In some rather rare instances, these thresholds are also exceeded by smaller events not of interest here, such that an additional threshold for the dew point temperature was defined: the average of one hour after the detected jump has to be 2 K larger than the average one hour before the jump. The

other indicators mentioned before suffer from different difficulties but could potentially be used in the presence of appropriate measurement equipment to reduce uncertainties: turbulence is not reported from synoptic stations and not measured from the AWSs in use; the increase in surface pressure is often weak and only detectable with high precision instruments; a decrease in temperature with the arrival of the cold pool can be masked at night by downward mixing of warmer air from above a surface inversion (Knippertz et al. 2007). The downward mixing of heat is discussed in more detail in section 5.6.

The thresholds described above are well suited for AWSs with a high measurement frequency, in the case of the IMPETUS station network 10 to 15 min. However, for an application to synoptic stations, longer measurement intervals need to be considered. This is neither for the precipitation and wind speed criteria, nor for the difference in T_d one hour before and after the passage of concern. But the actual abrupt jump in T_d during the passage of a cold pool's leading edge is often not well captured. The best-case scenario for a measurement interval of one hour is that the passage falls between two measurements. In this case a measured increase of 4 K would result in 2 K per 30 min. The worst-case scenario is that the passage coincides with one measurement. In this case half of the 4 K increase would happen before the measurement, the other half afterwards. This would result in 4 K per 2 h or 1 K per 30 min. This issue was addressed statistically by thinning out the observations from the IMPETUS station network to hourly temporal resolution. The threshold for ΔT_d was then reduced in 0.1 K steps until the minimal bias between the number of events detected with full and reduced temporal resolution was reached. Fortunately, the worst-case scenario mentioned before is much less likely and the actual increase in T_d is often significantly larger than 4 K. The minimal bias (+3.1%) was reached for $\Delta T_d = 2.5$ K, where 255 of 357 single station events were matched, 113 events were added, and 102 events were removed. The procedure was repeated for a temporal resolution of 30 min, where the minimal bias (+3.4%) was reached with $\Delta T_d = 3.5$ K. In this case 308 of 357 events were matched, 61 events were added, and 49 events were removed.

The characteristics of the leading edge are very likely detected at multiple stations at the same time or within a short time period, especially in the case of a dense station network like the one described in section 2.1. The number of stations where the detection thresholds are exceeded could provide information about the strength or spatial extent of the

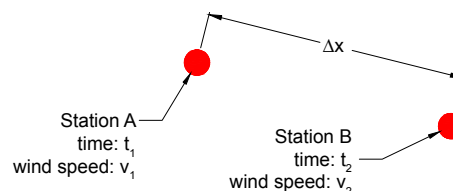


Figure 3.2.: Illustration for the calculation of the maximal distance between two stations.

could provide information about the strength or spatial extent of the

events, but should otherwise not influence the climatology. Thus, in the second step of the algorithm, cases detected at single stations that happen nearly simultaneously are grouped together into single events, as they belong very likely to the same cold pool or at least to the same convective episode, which can create several connected cold pools. Emmel et al. (2010) used fixed time intervals for all pairs of stations for this purpose. Here, in order to make the algorithm applicable to other station networks as well, the maximum time difference between two station cases depends on the distance between the stations (Δx) and the average of the observed wind speed at both stations (v_1 and v_2 , see Fig. 3.2). The selected criterion is that the propagation of the cold pool should not be slower than the half of the observed wind speed. This results in a maximum time difference for the detection at both stations of $\Delta t_{max} = 4\Delta x / (v_1 + v_2)$. If the observed time difference ($\Delta t = \text{abs}(t_1 - t_2)$) is larger than Δt_{max} , then the single cases are considered to have different sources. In addition to the time criterion, a maximum distance Δx of 1000 km is allowed. As in Emmel et al. (2010), an event is classified as a cold pool event if observed at least at two stations. Cases that are only detected at one station, but are too weak to exceed the thresholds at another one, are ignored for the climatology. This criterion has a quite restrictive effect as more than half of the cases detected in the IMPETUS network is only detected at one station. But its application together with the requirement for no rain ± 1 h and the persistently increased T_d for one hour ensures that the created climatology is a conservative estimation for the occurrence of large-scale cold pool events and not biased by the potentially much more frequent occurrence of smaller-scale cold pools and microbursts.

3.1.2. Microwave Satellite Convection Screening

Not only convective cold pool events are selected by the first two steps of the algorithm, but also large-scale flows like cold inflows from an adjacent ocean or synoptic cold fronts could fulfill the same criteria. These synoptic-scale features are better reproduced by numerical models than cold pools. Since model evaluation is an intended application of the created climatologies, the third step of the algorithm is designed to remove these events not related to deep convection by means of microwave satellite data. Satellite overpasses from a time window of -6 h to +3 h around the event are selected. These overpasses are scanned for convection in a radius of 324 km ($6 \text{ h} \times 15 \text{ ms}^{-1}$) around the involved stations in a view angle of ± 60 degree relative to the mean observed wind direction (an example for this wedge-shaped area is shown in Figs. 3.1a and b). The selected value of 15 ms^{-1} is the mean wind speed found by Engerer et al. (2008) for cases in Oklahoma. Here, this value was adopted although Knippertz et al. (2007) found somewhat

Table 3.1.: Criteria applied during the three steps of the convective cold pool event detection algorithm. Symbols: T_d = dew point temperature in 2 m; t_{max} = maximal time difference between the detection at two stations; Δx = distance between two stations; v_i = wind speed measured at the i -th station; v_{mean} = mean wind speed in 60 min

<i>Description</i>	<i>Threshold</i>
Step 1 : Preselection of cases based on station data	
Increase of dew point temperature (ΔT_d) within 30 min	≥ 2.5 K–4 K (observation interval dependent)
Difference between mean T_d within 60 min after jump in T_d and 60 min before jump in T_d	≥ 2 K
Mean wind speed (v_{mean}) within 60 min after jump in T_d	≥ 4 ms ⁻¹
Precipitation ± 1 h around jump in T_d	= 0 mm
Step 2 : Grouping of contemporaneous cases from multiple stations into single events	
Maximal time between jump in T_d at two stations	$\Delta t_{max} = 4\Delta x / (v_1 + v_2)$
Maximal distance between stations (Δx)	1000 km
Minimal number of stations for one event	2
Step 3 : Confirming the existence of a nearby convective system based on microwave satellite data.	
Convective event detected by gradient in 150/157 GHz brightness temperature	≥ 1.8 K–2.55 K (scan position dependent)
Maximal distance between station(s) and convection in satellite image	324 km (6 h \times 15 ms ⁻¹)
Maximal angle between wind direction and connection line between station(s) and convection in satellite image	60°

lower values of 8–12 ms⁻¹. A summary of all applied criteria for the detection of convective cold pool events is given in table 3.1.

In the microwave channels of AMSU-B and MHS, convection becomes visible through a reduction of brightness temperatures due to scattering by large ice particles. Bennartz and Bauer (2003) found the 150 GHz window channel to be most sensitive to these particles, and concluded that this channel should be used in mid and high latitudes. However, this channel is also sensitive to the surface emissivity, which in turn is affected by snow cover, a phenomenon not uncommon for the High Atlas in winter and spring. An alternative, which is not sensitive to surface emissivity, are the channels around the water vapor absorption line at 183.3 GHz, since their weighting functions peak above 10 km. Burns et al. (1997) suggested to use the difference between the 183.3 \pm 1 and \pm 3 GHz channels for convection screening. This approach is only well suited for the tropics, because of the high altitude peak in the weighting function of these channels (Bennartz and Bauer 2003). Hong (2005) used all three channels around 183.3 GHz for a method to detect convection and convective overshooting between 30°S and 30°N. His criterion is that the difference between 183.3 \pm 1 and \pm 3 GHz as well as the difference between 183.3 \pm 1 and \pm 7 GHz is positive (at nadir).

The differences between the 183 GHz channels give a very clear distinction between areas with active convection and their surroundings

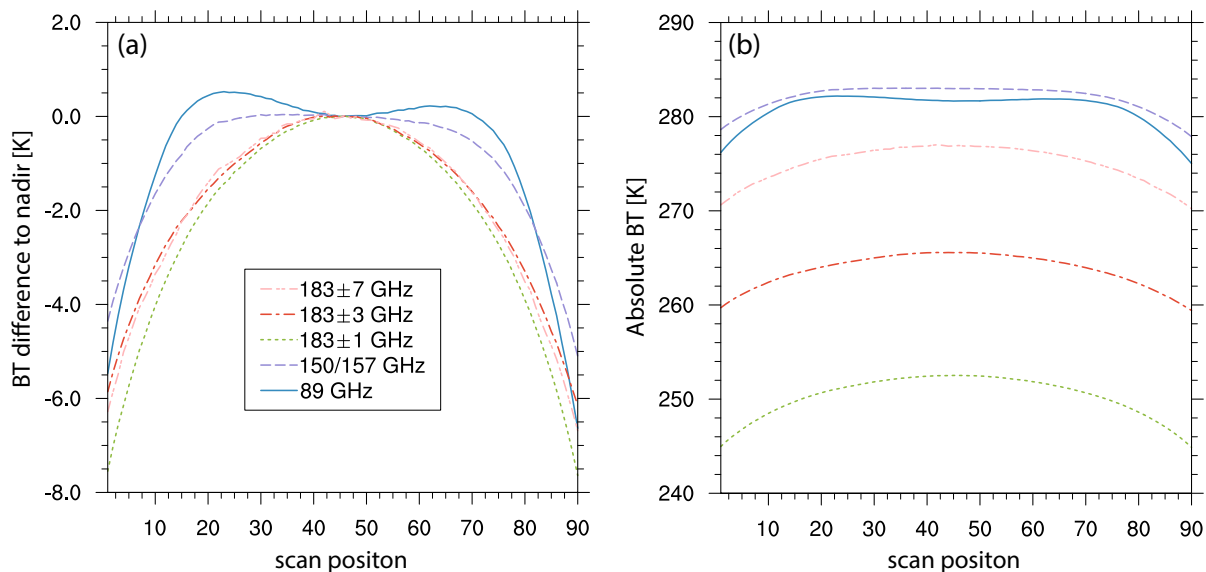


Figure 3.3.: Mean values for BTs at all scan positions averaged over all overpasses and all satellites. (a) Differences to nadir values; (b) absolute values.

(cf. Figs. 2.4c and d). Unfortunately, these channels are affected by noise in many instances. On the one hand this is due to RFI as mentioned in section 2.5; on the other hand, an increase in noise levels over time was found within the 183 GHz channels of some satellites. A simple, but effective algorithm to estimate noise variance of images, originally designed for the processing of photographs (Immerkær 1996), was applied to detect affected overpasses. It turned out that NOAA-15, -16, and -19 were particularly affected by increasing noise levels. Details are described in appendix A.1. In order to obtain a method of convection screening that is stable over time, it was therefore decided to use the 150 or 157 GHz channel, which is unaffected by noise. In order to overcome the surface emissivity issue, the horizontal gradient of the brightness temperatures was used rather than the values themselves. In addition, pixels with a distance of less than 50 km to the coastline were ignored as the different emissivity of water and land surface cause a large gradient as well. For the gradient, a threshold of 2.55 K was chosen by comparing the 150/157 GHz and 183 GHz channels of all noise-free satellite overpasses. At nadir, this yields the same number of cases like the Hong (2005) algorithm. Away from nadir, the threshold was adapted to account for the view angle (see next section). Cases are defined here as one pixel or a contiguous block of several pixels above the threshold.

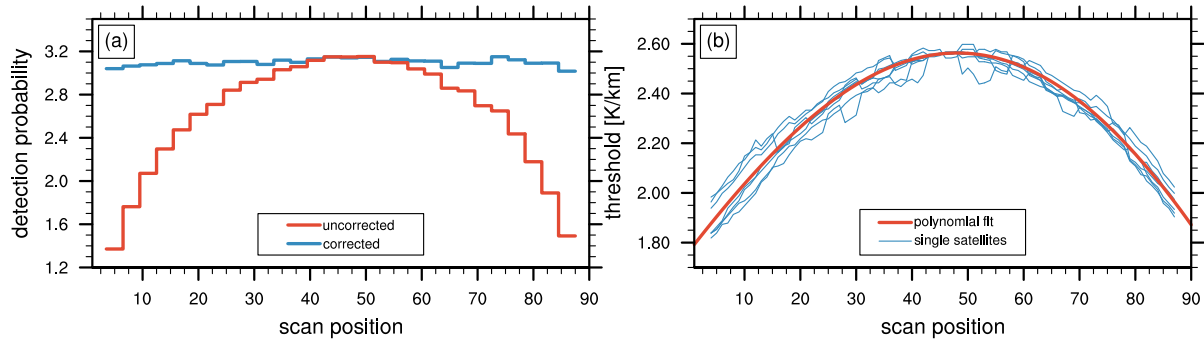


Figure 3.4.: (a) Probability to detect a convective event (number of events per 10000 pixel), binned every three pixel across track before and after limb effect correction; (b) threshold for brightness temperature gradients in the 150/157 GHz channel for convection screening after limb effect correction. Source: Redl et al. (2015).

3.1.3. Limb Correction for AMSU-B and MHS

Like other cross-track scanning instruments, AMSU-B and MHS are affected by a so-called limb effect. This effect arises from the shorter path through the atmosphere at nadir compared to the outer scan positions. Thus, the weighting functions at outer scan positions are shifted upward in altitude (Goldberg et al. 2001) and render constant thresholds for the detection of convection problematic. This issue can be addressed by a correction of the brightness temperatures themselves (cf. Wark et al. 1993; Goldberg et al. 2001; Eymard et al. 2010) or, alternatively, by scan-position-dependent thresholds (cf. Hong 2005). The latter solution was selected, since absolute brightness temperature values are not of interest here.

Based on a cloud model and a radiative transfer model, Hong (2005) suggested a threshold between 0 K at nadir and about 20 K at the outermost scan positions for the differences of the 183.3 GHz channels. In a more recent review of the Hong algorithm based on observations, a much smaller view angle dependency of 3.2 to 5.0 K was found (Xu et al. 2009). These authors considered this to be negligible and suggested a constant threshold of 0 K. Even if hardly visible by eye (see Fig. 2.4b), the 150/157 GHz channel is significantly affected by the limb effect (Fig. 3.3). The outermost scan positions appear darker. To quantify this effect for the gradient-based convection screening, the probability to detect an event was calculated for three-pixel wide bins that were aligned in an across-track direction. The outermost bins were ignored, as the edge of the swath often cuts through a convective system. Without a limb effect, it should be equally probable to detect an event for each scan position. However, it was found that it is more than twice as likely to detect convection in the center of the swath compared to the margins (Fig. 3.4a).

A prerequisite for a meaningful climatology is to overcome this view angle dependency for the convection screening. Therefore, a correction procedure was developed with the aim to get the same detection

probability at each scan position as at nadir. We use an iterative procedure with three steps in which only land pixels are considered: (a) calculation of the detection probability for convective events (p_{conv}) and calculation of the empirical [Complementary Cumulative Censity Function](#) ($CCDF = 1 - CDF$) of the gradient in brightness temperature ($CCDF_{grad}$) for each scan position x ; (b) calculation of the ratio between the detection probability at nadir and at each scan position x :

$$r[x] = p_{conv}[nadir]/p_{conv}[x] \quad (3.1)$$

the nadir value of p_{conv} is the average over the two central 3-pixel-bins; (c) selection of a new threshold ($T_{new}[x]$) for each scan position with a probability of occurrence $r[x]$ times higher than the original one:

$$q_{new}[x] = CCDF_{grad}(T_{old}[x]) \cdot r[x] \quad (3.2)$$

$$T_{new}[x] = CCDF_{grad}^{-1}(q_{new}[x]) \quad (3.3)$$

Finally, a fourth-order polynomial is fitted to the new thresholds.

The event detection probability is not directly proportional to probabilities of gradient values at individual pixels. The reason is that an event consists of several continuous pixels above threshold and the number of pixels per event also depends on scan position. Thus, applying equations (3.1) – (3.3) does not directly yield the result shown in Fig. 3.4 but is only a step in this direction. After six iterations, this procedure results in an almost flat detection characteristic. It is worth noting that the final thresholds (Fig. 3.4b) are not symmetric about the center. This can be explained by asymmetries in the measured brightness temperatures themselves (Fig. 3.3). These asymmetries actually differ from satellite to satellite ([Buehler et al. 2005b](#)), but this was ignored here as the number of overpasses per satellite would otherwise not have been sufficient for a robust statistic.

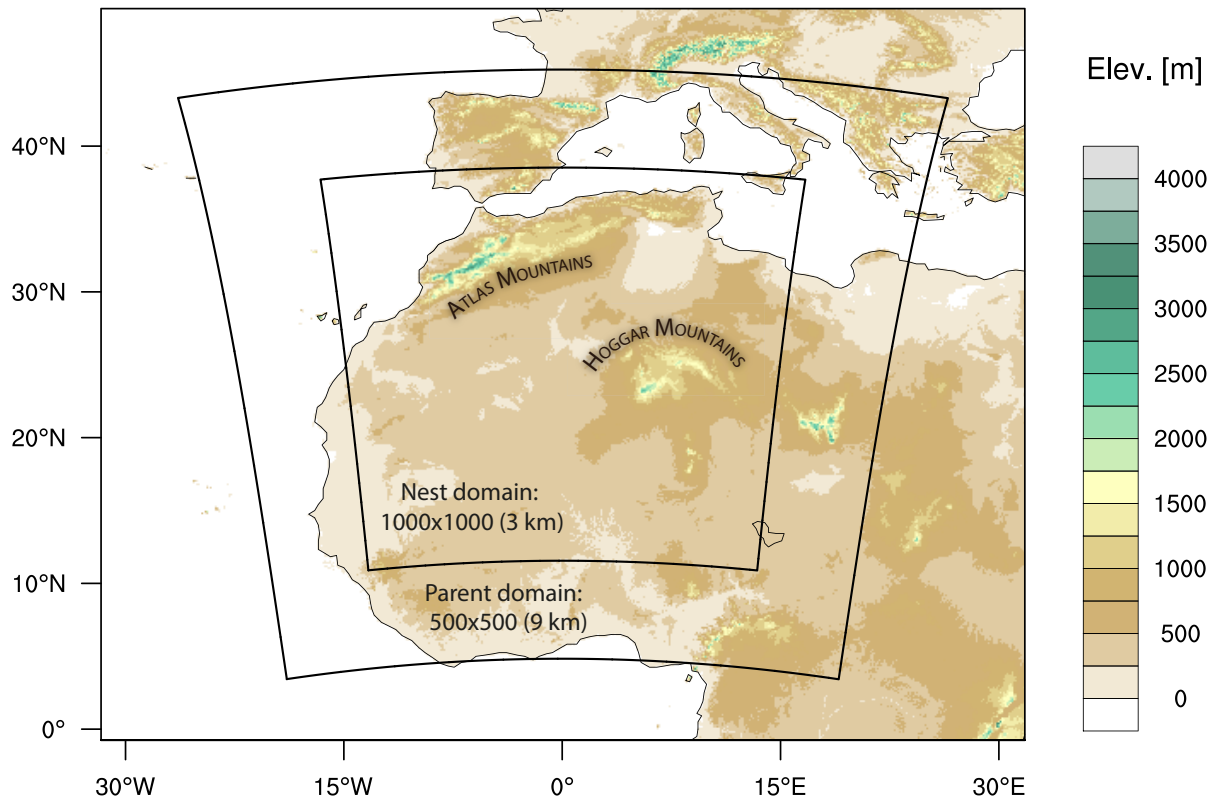


Figure 3.5.: Model domain with orography. Shown are parent and nest domain indicated with bold black lines.

3.2. Sensitivity Experiments with WRF

All sensitivity experiments are designed as a comparison between an undisturbed control run with realistic convective cold pools and modified runs. These include 'unphysical' changes to the treatment of latent heating and cooling, as well as the usage of convection parameterization schemes.

3.2.1. The WRF Model and its Configuration

The [Weather Research and Forecast \(WRF\)](#) model is a numerical model primarily developed in cooperation between the [National Center for Atmospheric Research \(NCAR\)](#), the [National Centers for Environmental Prediction \(NCEP\)](#), which belong to NOAA, the [Air Force Weather Agency \(AFWA\)](#), and the [Federal Aviation Administration \(FAA\)](#). It is designed for research as well as for operational weather forecasts and offers a wide range of applications from [Large eddy simulations \(LESs\)](#) over meso-scale to global simulations, and from now-casting to climate projections. At the time of writing, it is operationally in use at the centers [NCEP](#) and [AFWA](#). WRF is an open-source project and the user community is encouraged to contribute to the development of the model itself as well as to related tools. Not least, this is supported by the very

3. Methods

Table 3.2.: Configuration of the WRF model used for all experiments. Deviations from this setup are made only for low resolution experiments described in section 3.2.4 and 5.7.

<i>Setting</i>	<i>Description</i>	<i>Parent</i>	<i>Nest</i>
projection	rotated lat-lon grid	✓	✓
center point		25°N, 0°E	25°N, 0°E
grid points		1000 × 1000	500 × 500
resolution		0.081° (9 km)	0.027° (3 km)
vertical layers	20 below $\eta = 0.8$	70	70
time step		30 s	10 s
<i>Parameterization schemes</i>			
microphysics	Morrison double moment (MOR2)	✓	✓
SW/LW radiation	Rapid Radiative Transfer Model for GCMs (RRTMG)	✓	✓
boundary layer	Mellor-Yamada-Nakanishi-Niino level 2.5 (MYNN2)	✓	✓
land surface	Noah land surface model	✓	✓
convection	Grell-3d	✓	

extensive user guide (Wang et al. 2013) and technical documentation (Skamarock et al. 2008; Janjić et al. 2010).

WRF combines two alternative dynamical cores into the common WRF Software Framework (WSF). On the one hand, this is the Non-hydrostatic Mesoscale Model (NMM) core (Janjić et al. 2010), developed mainly by NCEP, and based on the Eta-model (Black 1994). On the other hand, this is the Advanced Research WRF (ARW)¹ core (Skamarock et al. 2008), developed mainly by NCAR, and based on the MM5-model (Grell et al. 1995). Both cores solve the fully compressible non-hydrostatic Euler equations and would have been suitable for the present study. ARW was selected as it is more flexible, e.g., in terms of available parametrization schemes, and also more commonly used in research applications. Version 3.5.1, released in September 2013 is used here for all experiments.

Even though the focus of this study is on cold pool events originating from the Atlas Mountains, the model domain covers a much larger region in order to have a realistic representation of the SHL and all ventilation mechanisms at its fringes. The model domain is centered at 25°N and 0°E, close to the climatological center of the SHL in June and July (Fig. 1.3). A two-way nesting is used with a horizontal resolution in the parent domain of 0.081° (approx. 9 km), which covers the western part of the African continent and parts of southern Europe (Fig. 3.5). The

¹ARW vs. NMM: Both model cores offer a comparable set of features. Thus, it can be speculated whether the development of both versions will continue unlimitedly. At the time of writing, the NMM user web page (<http://www.dtcenter.org/wrf-nmm/users>) states that funding for NMM has ended and support will no longer be provided.

nest domain has a horizontal resolution of 0.027° (approx. 3 km), covers the SHL, the Atlas and Hoggar Mountains, and extends far enough south to include MCSs at the southern flank of the SHL. The two-way nesting was selected as it enables feedback from the nest to the parent domain. Modifications to the pressure gradient at the fringes of the SHL, e.g., caused by cold pool events located inside the nest domain, can in such a setup influence the atmospheric flow in the parent domain, which in turn may alter the ventilation of the SHL. A one-way nesting without feedback from the nest domain would break this back coupling, with negative consequences for the interpretability of the experiments.

In the vertical, the upper boundary of the domain is set to 30 hPa, 70 layers are used, 20 of them below $\eta = 0.8$ (about 1.8 km above ground; η is the terrain-following vertical coordinate of WRF). The number of layers in the PBL is usually fixed in WRF with 11 layers below $\eta = 0.8$ and independent of the total number of layers. Increasing this number has been shown to have a positive effect on other PBL phenomena such as the NLLJ and low-cloud formation over southern West Africa (Schuster et al. 2013). The selection of parameterization schemes, listed in Table 3.2, is consistent with this study. References to all parameterizations can be found in the WRF User Guide (Wang et al. 2013).

3.2.2. Modifications of Model Microphysics

To quantify the impact of large-scale convectively driven cold pools from the Atlas Mountains on the SHL, it is necessary to remove the cold pools as completely as possible without perturbing the model otherwise. The most drastic way is to suppress Latent Heat (LH) release over the entire domain. This approach, however, also suppresses convection in the Sahel and therefore makes it difficult to separate the effect of Atlas convection on the SHL. Consequently, the manipulations to the model microphysics were restricted to elevated terrain in Morocco, Algeria, and Tunisia. Technically the selection of this area is implemented as a set of additional namelist settings in the model configuration. The settings contain corner coordinates of a polygon (red line in Fig. 3.6) and a threshold for the elevation. Setting this threshold to 500 m results in the blue area shown in Fig. 3.6 where the bulk of convection north of the SHL occurs (see section 4.2).

The first two days of the case discussed in section 5.2 are used here to analyze the consequences of different ways to remove convective cold pools. In a first experiment, latent heating and cooling were suppressed completely, resulting in removal of convection and associated cold pools in the Atlas region. The problem with this approach is that removing the whole convective system means that the upper-level flow

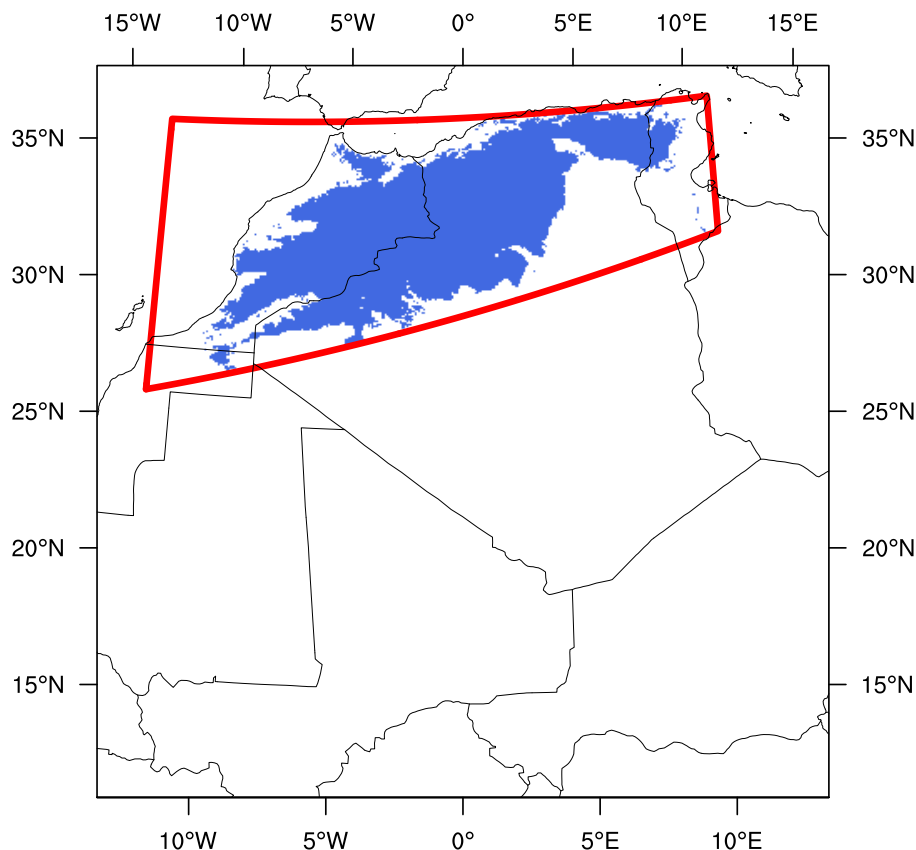


Figure 3.6.: Grid points with manipulated microphysics. Red line indicates a polygon defined by namelist settings that describes an area in which elevated grid points are searched. The blue shading indicates the selected grid points.

is significantly changed (Fig. 3.7d). The upward transport of mass and the anti-cyclonic outflow at the tropopause are missing. Consequently, the difference in surface pressure between control run and experiment are not solely caused by the removal of cold pools. Also, two additional unwanted side-effects are found. Firstly, the suppression of convection does not hinder the development of precipitation completely. Light stratiform rain is produced, which is neither reaching the surface at most grid points (Fig. 3.8a) nor is the evaporative cooling strong enough to form a cold pool (Fig. 3.7a). On the one hand, it is desired not to create a cold pool, but on the other hand it is an issue that not enough moisture is removed from the atmosphere. This is the cause for the second side effect. The moisture, not precipitating out over the Atlas Mountains, is transported westward and triggers convection outside of the modified area one day later. A significant cold pool centered approx. on 1°E, 29°N and spanning about 600 km is simulated in the second night of the experiment (Fig. 3.8b). This event is not observed; experiments spanning multiple days are therefore difficult to interpret.

Given the temporal clustering of convection, which is one of the results from the cold pool climatology (see section 4.3), however, experiments over several days are desirable. Thus, a second experiment

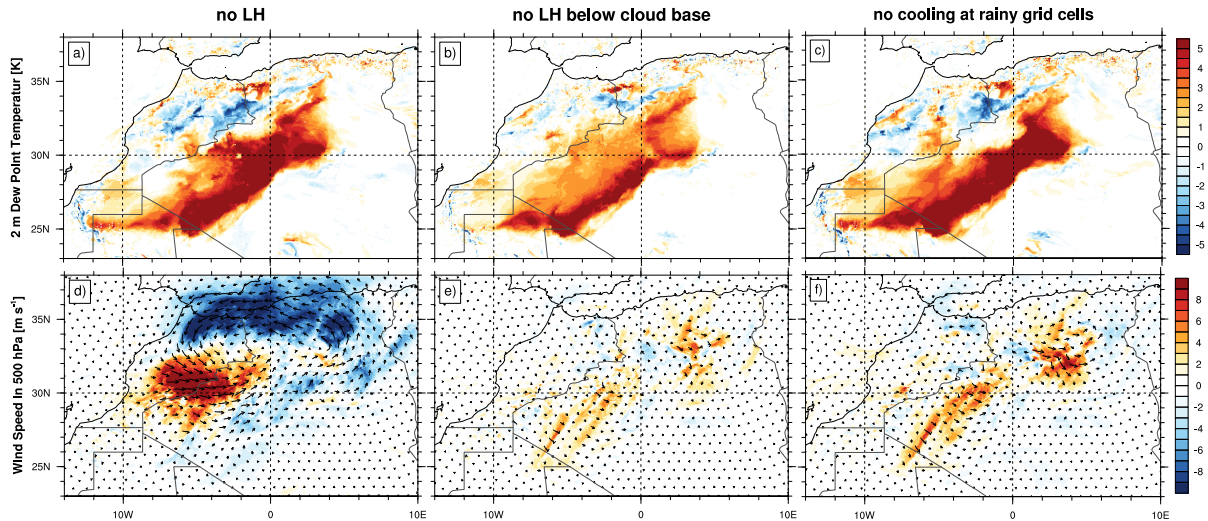


Figure 3.7.: Differences between the control run of the first case at 21 June, 06 UTC (+30h) and runs with three different methods of cold pool removal (control run – modified run). Left column: no LH over the Atlas Mountains. Center column: no LH below cloud base. Right column: no evaporative cooling at grid cells with rain. Top row: 2 m dew point temperature [K]. Bottom row: wind speed in 500 hPa [m s^{-1}]. Source: Redl et al. (2016).

was designed with the aim to remove the cold pool while keeping the convective system itself as intact as possible. A main driver for the cold pool is the evaporation of raindrops on their way from the cloud to the surface. The idea behind this experiment is therefore to disable the evaporative cooling ($LH < 0$) below cloud base. In addition, the water vapor created by evaporation (ΔQ_{vapor}) below cloud base is removed. This experiment did not disturb the upper-level flow significantly (Fig. 3.7e), but the cold pool was also only partially removed (cf. Figs. 3.7a and b). This experiment is therefore well suited to investigate the amount of rain evaporated below cloud base, but the total effect of the cold pool remains unclear.

To overcome this issue, vertical profiles of latent heating and mixing ratios of all hydro-meteors were calculated from the control run of the test case. Profiles from grid points over the Atlas Mountains, where rain reached the surface at 18 UTC (5006 profiles in total) were se-

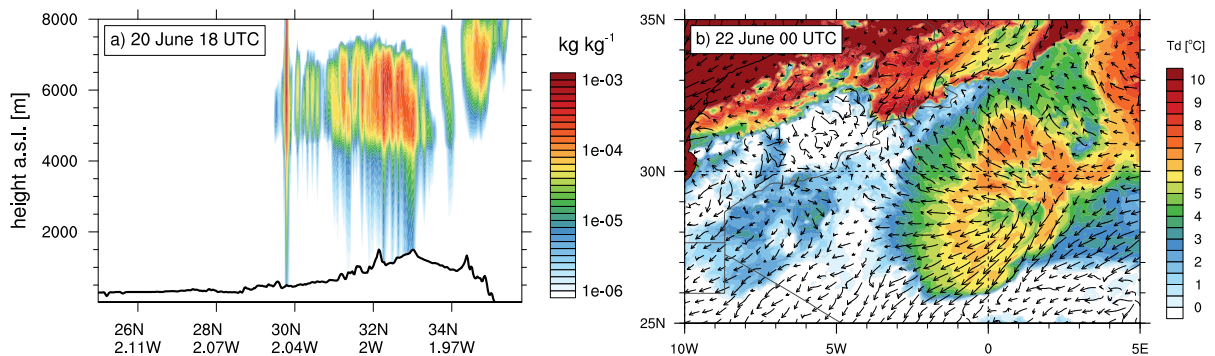


Figure 3.8.: Consequences of disabled latent heat release over the Atlas Mountains: (a) Sum of mixing ratios for rain, snow, and graupel at 18 UTC on first integration day. (b) 2 m dew point temperature [$^{\circ}\text{C}$] (shading) overlaid with 10 m wind vectors after 48 h.

lected, moved into a common origin relative to their respective cloud bases, and then averaged. The maximum evaporative cooling was found about four model layers above cloud base (Fig. 3.9a). According to the profiles of the mixing ratios for rain (Q_{rain}), graupel ($Q_{graupel}$), and snow (Q_{snow}), this is not where the strongest evaporation of rain is found, but where snow and graupel melts to rain. This is supported by Engerer et al. (2008), who found ice processes to be particularly important for the strength of a cold pool. Thus, the explanation for the incomplete removal of the cold pool in the second experiment is that a significant fraction of cooling remained in the system (Fig. 3.9b).

Therefore, a third experiment was created. Again modifications are only applied to the grid points over the Atlas Mountains, but this time evaporative cooling and ΔQ_{vapor} were set to zero for grid cells with $Q_{rain} > 0$ and $LH < 0$. This effectively removes all cooling from the system (Fig. 3.9c), but the release of latent heat remains largely unchanged. As a result, the upper part of the convective systems develops in a way comparable to the control run (Fig. 3.7f), while the cold pool is removed (Fig. 3.7c). This also indicates that, unlike MCS in the Sahel, the cold pool is not mandatory for the organization of the system. All further experiments are carried out with this model configuration.

3.2.3. Tracing of Moisture from Evaporation of Rain

In addition to running sensitivity experiments with removed cold pools, a tracer variable for water vapor created by the evaporation of rain (Q_{ev}) is introduced to WRF and used in the control runs. For each time step t , the tendencies in water vapor created from the microphysics scheme (ΔQ_{vapor}) are added to this new tracer variable:

$$Q_{ev}(t) = Q_{ev}(t-1) + \Delta Q_{vapor} \quad (3.4)$$

This is only done for grid points located over the Atlas Mountains with $LH < 0$, $Q_{rain} > 0$, and $\Delta Q_{vapor} > 0$. The new tracer is then advected with the model winds. To get a realistic estimation of how far this moisture can be transported, account is also taken for the ‘consumption’ of moisture by the creation of new cloud drops or other microphysical processes over the whole domain, also away from the Atlas Mountains. For grid points with $\Delta Q_{vapor} < 0$ the tracer is then reduced:

$$Q_{ev}(t) = Q_{ev}(t-1) - \min(Q_{ev}(t-1), -\Delta Q_{vapor}) \quad (3.5)$$

Cycles of consumption and recreation away from the Atlas are not taken into account, e.g., if the moisture from the tracer is used to create a new cloud and possibly rain drops outside the Atlas Mountains domain delineated in Fig. 3.6, then the moisture from the evaporation of these drops is not fed back into the tracer. Thus, the tracer variable

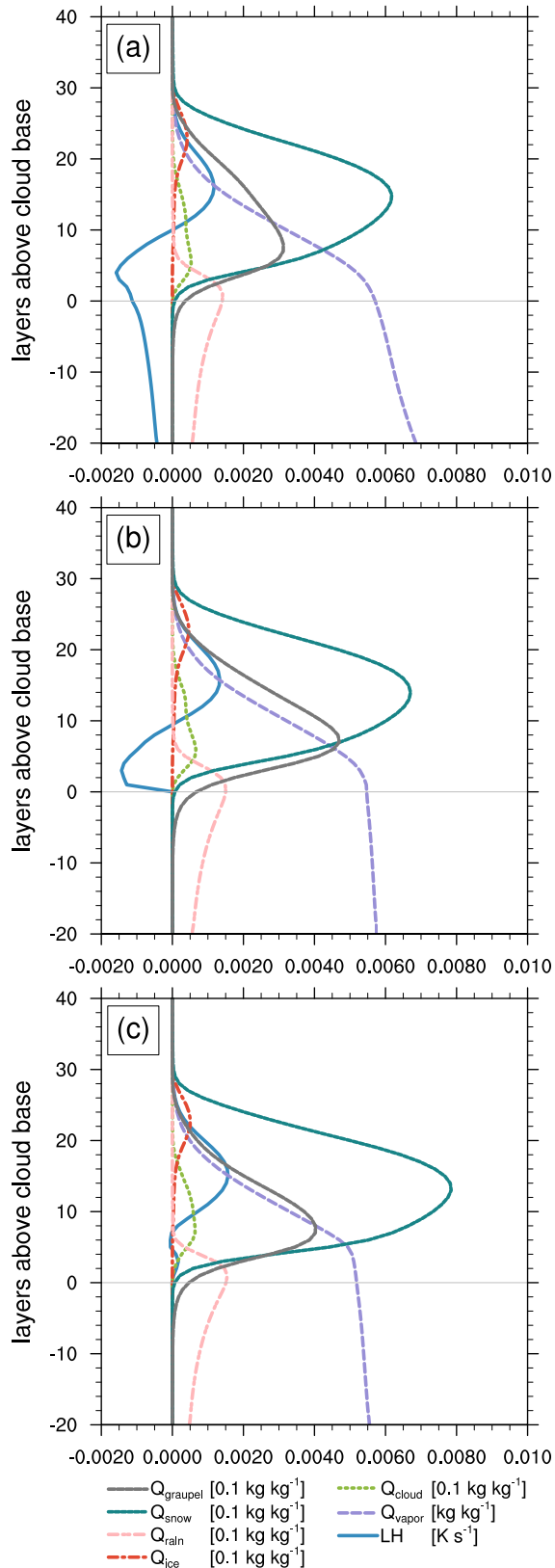


Figure 3.9.: Average vertical profiles of latent heating/cooling as well as mixing ratios for all hydrometeor species in the used microphysics scheme. Profiles are calculated by selecting grid points where rain reaches the surface over the Atlas Mountains at 18 UTC and aligning these profiles to their cloud base. (a) Control run, (b) no LH below cloud base, and (c) no evaporative cooling at grid cells with rain. Source: Redl et al. (2016).

Table 3.3.: Parameterization schemes for deep convection used in low resolution experiments. References can be found in Wang et al. (2013)

<i>WRF namelist</i>	<i>Abbrev.</i>	<i>Scheme</i>
1	KF	Kain-Fritsch
2	BMJ	Betts-Miller-Janjic
3	GF	Grell-Freitas
4	OSAS	Old Simplified Arakawa-Schubert
5	G3	Grell-3D
6	Tiedtke	Tiedtke
7	ZMF	Zhang-McFarlane
14	NSAS	New Simplified Arakawa-Schubert

introduced here yields a conservative estimation of the effect of moisture created by cold pools from the Atlas Mountains. Finally, the tracer variable is enabled in both WRF domains, but values from the parent domain are overridden by the child domain in overlapping areas due to the usage of two-way nesting.

3.2.4. Low Resolution Experiments with Different Convection Schemes

It has been shown that deep convection over the Sahel is responsible for a significant part of the monsoonal northward moisture flux and that parameterized convection leads to a significant bias not only in transport of moisture, but also in geopotential height in the Sahel region (Marsham et al. 2013a). These conclusions were drawn from comparison between runs using the UK Met Office Unified Model (UM) with parameterized and explicitly resolved deep convection at horizontal resolutions of 4 and 12 km. It is not clear whether these conclusions are robust for other convection schemes and coarser horizontal resolutions. Regional climate simulations for Africa are today usually performed with horizontal resolutions of 25 to 50 km (0.22° to 0.44°) (e.g., Jones et al. 2011). Also, the Atlas Mountains at the northern flank of the SHL were not part of the model domain. Therefore, for the first case study additional model runs using horizontal resolutions of 0.22°, 0.44°, and 0.75° were carried out with eight different parameterization schemes for deep convection but otherwise configurations identical to the parent domain of the control run (Table 3.3).

4. Climatology of Convective Cold Pool Events

The most important results presented in this chapter have been published in Monthly Weather Review: [Redl et al. \(2015\)](#).

4.1. Climatology with Station Data

The convective cold pool detection algorithm was first applied to the [IMPETUS](#) station network described in section 2.1. The year-to-year variability within the 10-year period from 2002 to 2011 shows no clear trend with an average number of 13.6 cases per year, but large differences between particular years from 9 (2004) to 22 (2008) cases per year (Fig. 4.1a). The year of 2012 was very likely the year with the weakest activity of convection during the whole period regarding the region covered by the [IMPETUS](#) stations, but the average number of cases per year was calculated without 2012 due to missing data from 23 September onwards. Deviations of the number of cases per year to [Emmel et al. \(2010\)](#) are largest for the years 2002 and 2003. In 2002, [Emmel et al. \(2010\)](#) found five cases more. One of them did not fulfill the slightly stricter criteria for the station data applied here (T_d has to stay higher for at least one hour), the other four cases were identified in station data, but did not fulfill the satellite criteria. Convective systems in these cases were too small or too far away from the stations. However, it is still possible that these cases are also cold pool events, but they have likely been weaker than the other events identified by the criteria in the present study. In 2003, the automated algorithm identified six cases more than [Emmel et al. \(2010\)](#), and from 2004 to 2006 two cases more per year. Additional cases are not surprising, because [Emmel et al. \(2010\)](#) used infrared images ($10.8\ \mu\text{m}$) in which high clouds can obscure low-level arc clouds and temperature differences associated with the leading edge of a cold pool. In four of the additional cases in 2003, the microwave images showed multiple convective cells around the stations. In such a situation contiguous high-level cloud shields are particularly likely. However, it should be remarked here that the automated algorithm is not able to distinguish a synoptic cold front with embedded deep convection from convection not associated with a frontal system.

4. Climatology of Convective Cold Pool Events

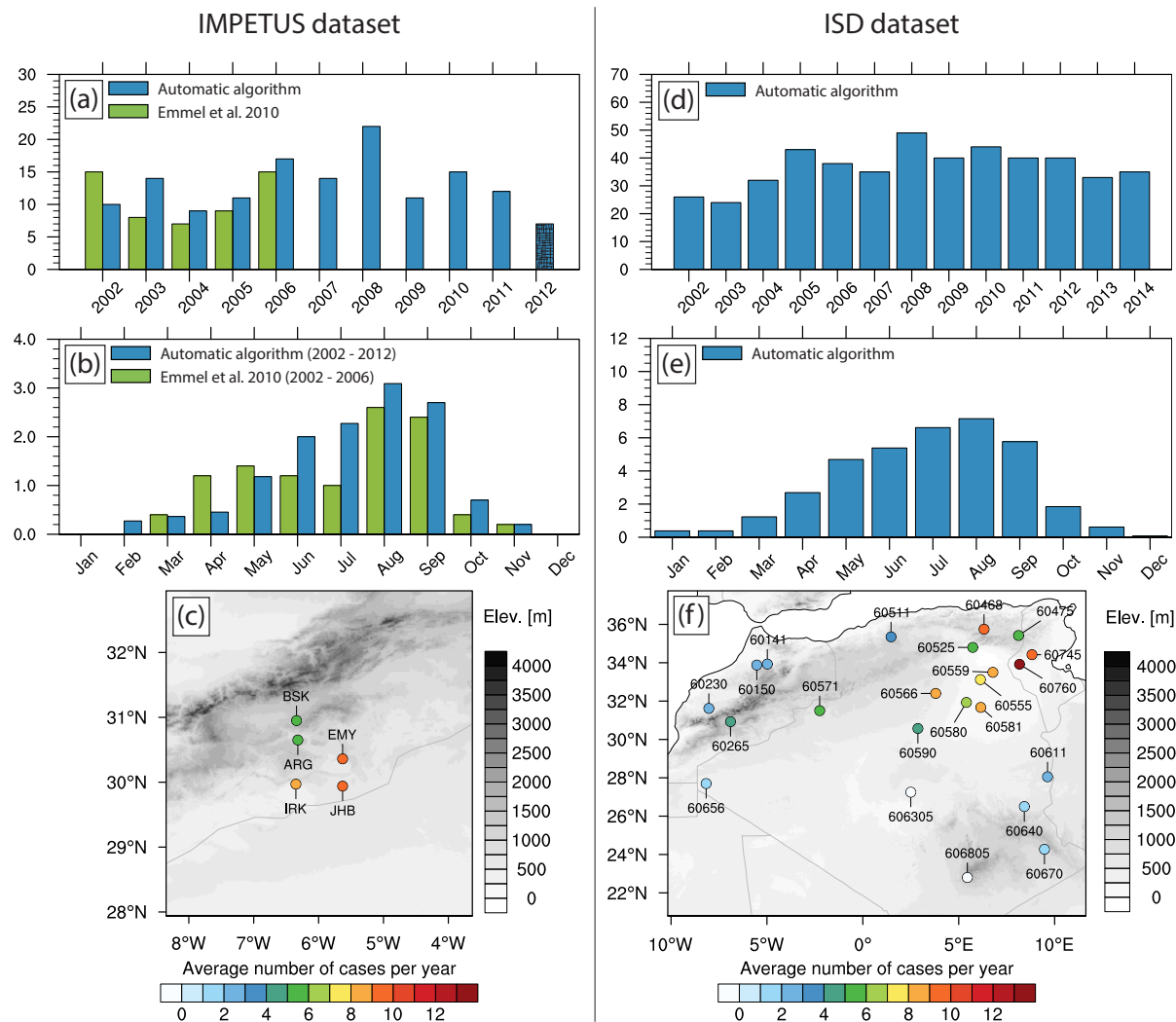


Figure 4.1.: Climatology of cold pool events created from the IMPETUS dataset (a–c) and the ISD dataset (d–f): (a and d) Number of cases per year; (b and e) average number of cases per month; (c and f) average number of cases per station and year. For all panels only months with more than 80% data availability per station are included in the calculation. The hatching in (a) indicates incomplete data for 2012. Source: Redl et al. (2015).

The annual cycle is unimodal with a maximum in August (Fig. 4.1b), which is contradictory to the bimodal annual cycle of precipitation with a summer minimum at the same stations (cf. Fig. 2.2). This temporal coincidence of the maximum in convective activity with the minimum in precipitation measured at the surface indicates that the majority of convective precipitation during the summer months evaporates before the surface is reached. The average number of cases per month from May to September is 2.3. Emmel et al. (2010) also identified August as the most active month, but found fewer cases for June and July. These differences are also evident for a subsample for the years 2002–2006 (not shown) and could be related to mid-latitude cyclones and their frontal systems with embedded convection creating ambiguous cases during early summer. Such convection embedded in cloud bands is harder to detect in IR-images. The maximum in August coincides with a maximum in mid-level moisture transport from tropical

West Africa. These **Tropical-extra-Tropical Interactions (TEI)** were analyzed by Knippertz (2003) based on mid-tropospheric backward trajectories. It could be shown that the majority of the precipitation that fell in August and September at the synoptic station of Ouarzazate (60265), which is in the vicinity of the **IMPETUS** station network, is related to TEI. In these months, the mid-level moisture transport combined with orographic forcing frequently triggers convection over the Atlas Mountains (Knippertz et al. 2003). The number of cases per year and station differs significantly, even between neighboring stations (Fig. 4.1c), which is likely a consequence of the complex terrain surrounding the stations. This finding is in agreement with Emmel et al. (2010), who also identified EMY and JHB as the stations most often affected by cold pools.

The **IMPETUS** station network covers only a very small area of the Saharan flank of the Atlas Mountains. With these stations alone, it is difficult to draw conclusions about the whole region and about how representative the **IMPETUS** stations are for a larger region in North Africa. The **ISD** dataset described in section 2.3 helps to overcome this issue. It includes stations with sufficient data availability for Morocco, Algeria, and Tunisia. The larger distances between the stations make it less likely to detect the same cold pool event at more than one station. This is especially relevant for stations without direct neighbors like Béchar (60571) or Tiaret (60511) where the number of detected events per year is reduced by up to 54% due to the requirement of a second station. Also, Ouarzazate (60265), which has no direct neighbor on the same side of the High Atlas, is affected with a reduction of 35% or 2.5 events per year. Both the coarser spatial station network and the coarser temporal resolution (30 min to 1 h) of the observations influences the comparability between the results achieved with both datasets. Nevertheless, the coarser temporal resolution was taken into account by adapted thresholds for ΔT_d (see section 3.1.1). Even if this introduces uncertainty for single cases, averages over longer time periods should be reasonable. An example is Ouarzazate (60265), which is located close to BSK and ARG. For all three stations the algorithm detects 4 to 5 cases per year (Figs. 4.1c and f). The analyzed time period is too short to calculate a smooth annual cycle from a single station, but as for the **IMPETUS** stations, the majority of events at Ouarzazate is also detected from May to September (50 of 61 events).

The number of cases per year for the **ISD** stations is 36.9 with 5.9 cases per month from May to September (Figs. 4.1d–e). The absolute numbers are larger compared to the **IMPETUS** stations due to the larger area covered. The pattern of the inter-annual variability shows similarities in terms of relatively active and inactive years, but also deviations like for 2003, which was relatively inactive using **ISD**, but not for the **IMPETUS** stations. Other interesting aspects of the **ISD** dataset are: (1) The region south of the Saharan Atlas and the Aurès Mountains is

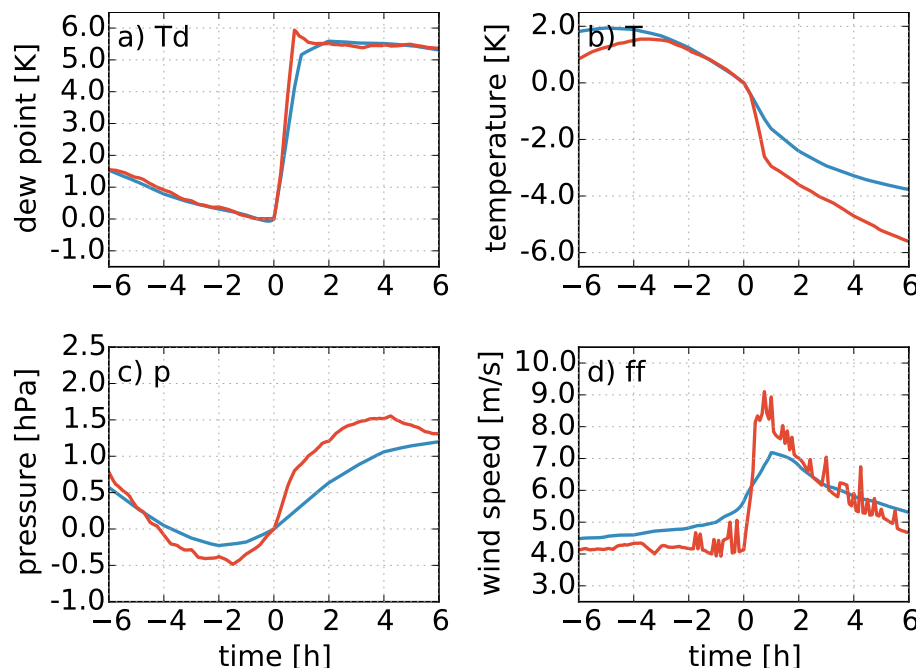


Figure 4.2.: Composite of variables measured by the **IMPETUS** (red) and **ISD** (blue) stations around the arrival of the leading edge ($time = 0$). Shown are relative changes for (a) dew point temperature, (b) temperature, (c) pressure (only from EMY and IRK), and (d) absolute values of the wind speed.

more frequently affected by cold pool events than the region south of the High and Anti Atlas (Fig. 4.1f, see Fig. 2.1 for geographic names). Consequently, the **IMPETUS** station network cannot be considered to be representative for the whole south of the Atlas region. (2) The annual cycle for the **IMPETUS** stations (Fig. 4.1b) differs from the annual cycle for the larger region covered by the **ISD** dataset (Fig. 4.1e) where the convective activity starts earlier in course of the year. The number of cold pools observed in May in the **ISD** station dataset already reaches more than two-thirds of the maximum number in August. May is less active for the **IMPETUS** stations with about 40% of the August maximum. The retarded increase in the vicinity of the High Atlas is possibly explained by the relocation of the Saharan Heat Low to the border region between Algeria and Mali. The associated mid-level anti-cyclonic flow transports moisture along its western side which has the strongest effect over the High Atlas region (cf. Knippertz et al. 2003; Knippertz 2003). On the contrary, extra-tropical cyclonic activity might lead to an elevated level of cold pool activity. However, a comprehensive analysis of the regional differences should include moisture transport at different levels for individual cases, as well as synoptic forcings and is not within the scope of this study.

Average characteristics of the cold pool events detected by the automated algorithm in both datasets are shown in Fig. 4.2. Characteristics at the **IMPETUS** stations are in good agreement with findings of Emmel et al. (2010), except for the pressure which was not analyzed there. The

clearest indicator is the jump in T_d (Fig. 4.2a), which of course is influenced by the threshold applied to this variable. Accordingly, cases with an increase below 4 K in 30 min (or 2.5–3.5 K for *ISD*) are not included. Nevertheless, the evolution of this variable shows an interesting aspect, it remains on an elevated level after the passage of the leading edge with an average increase of about 5.5 K. The increase itself is steeper due to the shorter measurement interval of the *IMPETUS* stations compared to the *ISD* stations. Also, the short peak immediately following the leading edge is visible in *IMPETUS* data only, but the mean value for the following hours is nearly identical for both datasets, which supports the assumption that quite similar events are detected. This persistent and significant increase is a particular feature of cold pools in (semi)-arid environments. *Provod et al. (2015)*, who analyzed 38 cold pool events observed during the monsoon season 2006 in Niamey, found increased levels of moisture only for cases preceding the monsoon onset, i.e., in relatively dry environment. The temperature decrease is less pronounced compared to the increase in T_d (Fig. 4.2b), but larger for the *IMPETUS* stations. This is possibly related to the geographic positions of the stations; more of the *ISD* stations are located deeper in the desert and possibly hit by cold pools later in the night. The diurnal cycle has a maximum around 18 UTC for both datasets, but for the *ISD* stations a larger fraction of the total number of cases is recorded in the second half of the night between 0 and 6 UTC ($\approx 20\%$ vs. $\approx 7\%$ for *IMPETUS*, Fig. 4.3). In such cases, a surface inversion would already be stronger and the effect of downward mixing at the leading edge more important. The decreases in the hours after the passage of the leading edge are likely the usual night-time cooling and only to a lesser extent related to the cold pool. *Provod et al. (2015)* found for the cases in Niamey a somewhat larger temperature decrease of 5.3 K (without excluding cases with precipitation reaching the surface).

The increase in surface pressure (p_{sfc}) is again more pronounced for the *IMPETUS* stations. Unlike T_d , p_{sfc} rises more slowly, after about 4 h an increase of 1.5 hPa is on average detected for the *IMPETUS* stations (Fig. 4.2c). This value is in agreement with the smaller decrease of temperature, which is also

smaller than for the cases in Niamey, where a mean value of 1.9 hPa was found. The increase in wind speed is, like T_d , most pronounced at the leading edge. The increase of about 5 ms^{-1} for the *IMPETUS*

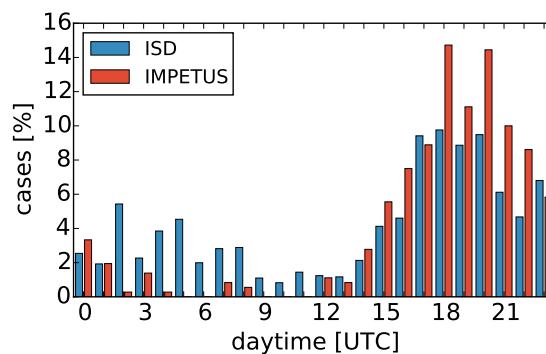


Figure 4.3.: Diurnal cycle of cold pool occurrence at the *IMPETUS* (red) and *ISD* (blue) stations.

stations (Fig. 4.2d) is again smaller than the values found in Niamey (6.5 ms^{-1}). However, the absolute values exceed the 7 ms^{-1} threshold often used for the estimation of the **Dust Uplift Potential (DUP)** (Equation 1.3). Accordingly, cold pools detected at the **IMPETUS** stations are strong enough to cause dust uplift over at least 2 h at points they pass. Moreover, the stations are located at or close to Lac Iriki, a salt lake fed by the river Drâa that is one of the most active dust sources south of the Atlas Mountains (Ashpole and Washington 2013). The absolute wind speed at the **ISD** stations is lower, again potentially caused by their locations, but likely also by the longer measurement intervals. Anyway, the mean cold pool detected at an **ISD** station also exceeds the 7 ms^{-1} threshold for dust emission.

4.2. Satellite Only Climatology

It was shown in the last section that the High and Anti Atlas are less often affected by convective cold pool events than regions farther east, but some uncertainty remains in this statement as the spatial density and the temporal resolution of the station data are relatively low. Therefore, an additional climatology independent of station data was created based on microwave satellite data alone. The climatology covers the region shown in Fig. 4.4 and was created on a regular $0.5^\circ \times 0.5^\circ$ grid with data from the years 2002 to 2014. For each grid cell and each day only the satellite overpass closest to 18 UTC (maximum in diurnal cycle of convection) was used, which avoids any influences of the varying number of satellites over time, since only one overpass per day was used. For each grid cell the occurrence of deep convection was counted. If at least one of the satellite pixels within a grid cell fulfilled the threshold criterion (see sections 3.1.2 and 3.1.3), this grid cell was assigned a one, otherwise a zero for this day. Finally, long-term monthly means of these counts were calculated. Fig. 4.4 shows their annual evolution. The maximum activity is, consistent with the station datasets, during the West African monsoon months of May to September (Figs. 4.4e–i). The differences in the spatial distribution of convection between May and June explain the differences between the average number of cases for these months in the **ISD** and **IMPETUS** datasets. In May convection over the High Atlas, where the majority of events for the **IMPETUS** stations originate, is significantly less frequently detected than over the Aurès Mountains where, given the distribution of stations, the majority of the events for the **ISD** stations originate.

Starting from June, the whole Atlas Mountains from Morocco to Tunisia are frequently affected by deep convection, for each grid cell on about 2–3% of the days. These values are, as one would expect, smaller than in the Sahel region. There, regions with orographic forc-

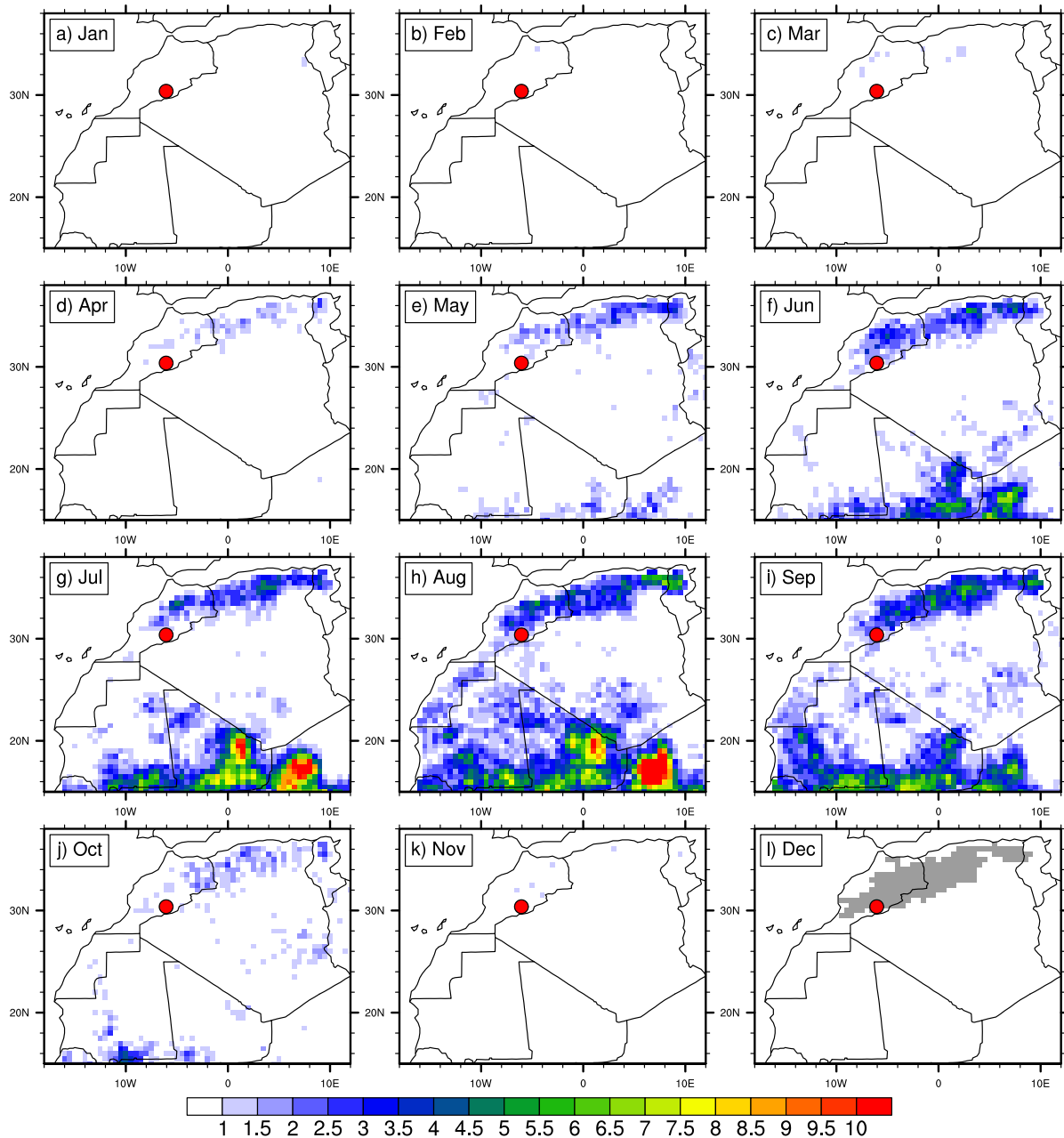


Figure 4.4.: Annual cycle of convective events in Northwest Africa. Shown is the percentage of days when a convective event was detected within one grid cell in the satellite overpass closest to 18 UTC from 2002 to 2014. The gray color in (l) marks grid points with an elevation of more than 700 m and indicates the area used for the calculation of the Atlas Mountains Convection Index (AMCI). The red dot indicates the location of the IMPETUS station network. Source: Redl et al. (2015).

ing like the Adrar des Ifoghas at the border between Mali and Algeria or the Air Massif in northern Niger are affected up to three times more often, as is best visible in July and August (Figs. 4.4g–h). Interestingly, these hotspots for deep convection in the Sahel are located north of the zone with constantly high values of CAPE in the ERA-Interim re-analysis (cf. Fig. 1.7). The relative frequency of convective events north and south of the SHL is in good agreement with a climatology of dust uplift events based on data from SEVIRI, created by Ashpole and Washington

(2013). There, on average 5–20 dust uplift events from June to August are detected south of the Saharan Atlas and the Aurès Mountains. In the foothills of the Mountains in the central Sahara up to 50 events are detected in the same period. Comparing these numbers to Figs. 4.1f and 4.4f–h encourages the assumption that a large proportion of dust uplift in Northwest Africa is related to cold pool events.

Despite the agreement in seasonal and geographical behavior between satellite-only and station climatology, there seems to be a significant difference in the absolute number of detected threshold exceedances. For the months May to September, the *ISD* station climatology indicates deep convection that generates cold pools at about 20% of the days per month while the values per grid cell in this period are much lower. The reason for this discrepancy is that the satellite-only climatology is by design a climatology of the occurrence of deep convective cells and not of convective cold pool events with large horizontal extent. Figure 2.4 illustrates that only the cores of convective systems are visible in the microwave image. The example shown is one of the strongest events in the whole period, but only a small number of pixels (10.9%) exceed the threshold for the gradient in brightness temperature. Nevertheless, a comparison with the *IMPETUS* station data reveals that the occurrence of deep convection can serve as a proxy for cold pool events. For the period 2002 to 2012, 84 events with deep convection were found in a circle of 100 km radius around the *IMPETUS* stations, 38 of which (45%) were strong enough to fulfill the station criteria.

The spatial distribution of cold pool events in northwest Africa resembles the pattern in biases of dew point temperature in the *ECMWF* operational analysis shown in the introduction (cf. Figs. 1.1, 4.1, and 4.4). Also, the temporal evolution of the biases, which is in close agreement with the annual cycle of cold pool events, suggests a causal connection. Knowing the dates of the events, a further refinement of the bias calculation is possible. It turns out, that 78% of all detected cases at stations from 2011 to 2012 are followed by a negative bias in dew point temperature averaged over 12 h past the detection. For 31% of the cases, the average bias exceeds -4 K. Interestingly, *ERA-Interim* shows a slightly better performance irrespective of its lower resolution. There, 68% of cases are followed by a negative bias, 27% exceed -4 K.

4.3. Atlas Mountains Convection Index

Part of the motivation for this study is the question of the frequency of strong convective cold pool events over the Atlas Mountains. This question was addressed here through the introduction of an Atlas Mountains Convection Index (hereafter referred to as *AMCI*). This index

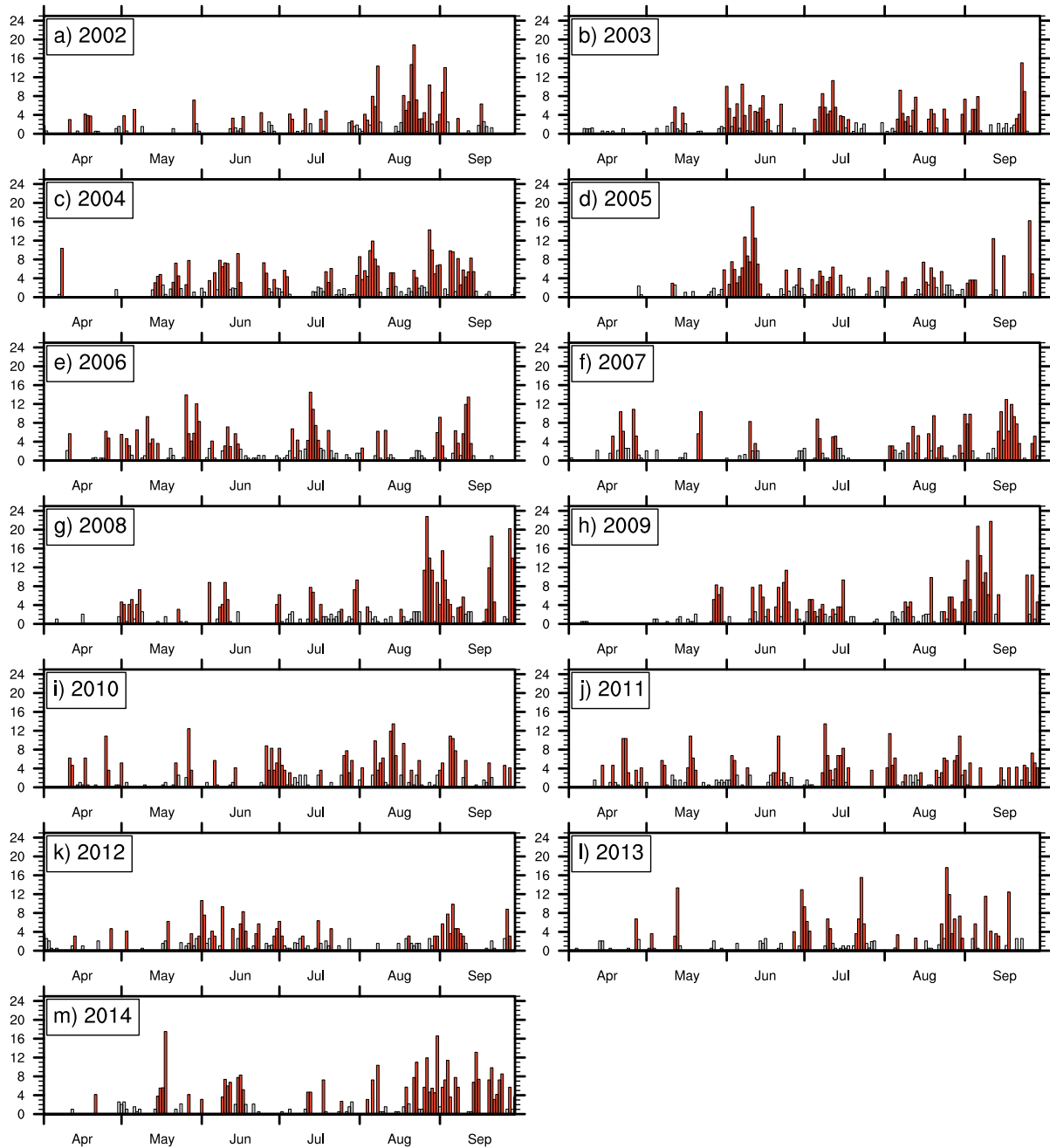


Figure 4.5.: Atlas Mountains Convection Index (AMCI, section 4.3): Percentage of the area of the Atlas Mountains with an elevation of more than 700 m (gray area in Fig. 4.4i) with convection for the years 2002 to 2014 and the months April to September. The red bars indicate days when the chosen threshold of 2.6% is exceeded. Source: Redl et al. (2015).

was calculated from all grid cells of the climatology that are located over the Atlas Mountains and whose elevation exceeds 700 m (see Fig. 4.4i). Virtually all convection in this region occurs in terrain above this level. The elevation threshold was selected somewhat larger than for the manipulation of the microphysics in WRF (see section 3.2.2), as it was there intended to remove also smaller events at the margins of the mountains. On a daily basis, the AMCI contains the percentage of grid cells with deep convection and is thus a measure for the size

4. Climatology of Convective Cold Pool Events

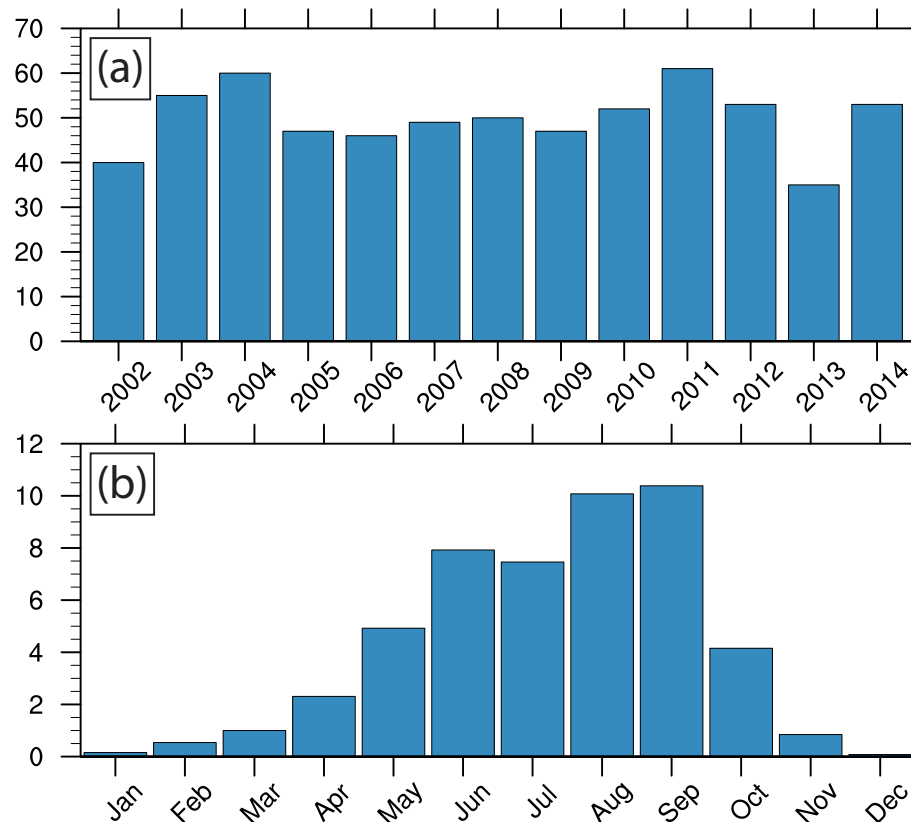


Figure 4.6.: (a) Number of convective events per year and (b) annual cycle calculated from the [Atlas Mountains Convection Index \(AMCI, section 4.3\)](#) with a threshold of 2.6%. Source: [Redl et al. \(2015\)](#).

of the convective events over the Atlas Mountains. The time series of this index (Fig. 4.5) shows the frequent occurrence of deep convection over the Atlas Mountains with a wide range of values. There are many events with small values, most likely weaker, unorganized systems with spatially restricted, smaller cold pools. Long lived events are created when cold pools from several cells merge and are therefore associated with higher values. In order to find a meaningful threshold, the [IMPE-TUS](#) station data were considered again. For two thirds of the cases selected from this dataset by the cold pool detection algorithm, the [AMCI](#) values exceed 2.6%. Thus, values above this threshold are assumed to belong to significant cold pool events. As with both station climatologies (Figs. 4.1a and d), the year-to-year variability of this parameter (Fig. 4.6a) shows no clear trend over the analyzed time period. The relative changes in the number of events detected in consecutive years differ from those found in the station climatologies. This is likely related to the irregular distribution of the stations. The annual cycle of the [AMCI](#) (Fig. 4.6b) shows the same general shape as the annual cycle from the [ISD](#) station dataset, but with a slightly larger number of cases per month, which is of course highly dependent on the selected threshold. Another difference is the yearly maximum, which is found in September in [AMCI](#) and in August in both station datasets. The maxi-

mum activity of convection in September is located over the Tell and the Saharan Atlas Mountains in northern Algeria (Fig. 4.4i), an area which is not well covered by the station datasets.

In addition to the frequency of occurrence, another interesting aspect of the AMCI time series is the temporal clustering of events. Particularly stronger events (that exceed the 2.6% threshold) seldom occur in isolation. Instead, these events tend to be clustered into multi-day episodes. Strong events usually occur on two consecutive days and are embedded into five-day long convectively active periods. This finding is in agreement with an analysis of dust episodes in May and June 2006 south of the Atlas Mountains by Knippertz et al. (2009b), which lasted four to eight days and were attributed to synoptic-scale features such as lee cyclones and upper-level troughs. To verify the subjective impression of clustering for the AMCI, a method common in wind storm analysis was applied, the so called dispersion statistic (Mailier et al. 2006):

$$\psi = \text{Var}(n)/E(n) - 1 \quad (4.1)$$

where $E(n)$ is the mean and $\text{Var}(n)$ is the variance of n . Equation 4.1 yields 0 for a homogeneous Poisson process, $\psi > 0$ corresponds to processes that are more clustered than random, and $\psi < 0$ corresponds to processes that are more regular than random. In this case, n is a time series of the number of convective events ($\text{AMCI} > 2.6\%$) in ten-day periods. To avoid the influence of the annual cycle, only the months between June and September were used in the calculation. As expected from visual inspection of Fig. 4.5, not all years show a statistically significant clustering, but when applied to the whole time series the dispersion statistic is $\psi = 0.57$, which is statistically significant at the 99.9% level. An answer to the question why some years show a more pronounced clustering than others would have to include an analysis of synoptic situations. However, this is not within the scope of this study.

5. Impact of Convective Cold Pools on the Saharan Heat Low

The most important results presented in this chapter have been published in the Journal of Geophysical Research: [Redl et al. \(2016\)](#).

5.1. Case Selection

Cases for the sensitivity experiments were selected based on the cold pool climatology presented in chapter 4. A basic condition was that the [IMPETUS](#) and Fennec stations are available for model evaluation, which restricts the time span to the years 2011 and 2012. The climatology for the [IMPETUS](#) stations (red dots in Fig. 2.1) contains 12 cases for 2011 and 7 cases for 2012. The selection was further limited by a screening of Meteosat [SEVIRI](#) 'Desert Dust' images. In order to enable a direct comparison between model output and satellite images, only cases where the leading edge of the cold pool was not covered by high-level clouds were selected. Control runs with [WRF](#) were created for the remaining eight cases. In two of them, the cold pool in the first night developed in satisfactory agreement with the satellite observations. Details of these two cases are discussed in section 5.2 and 5.3.

5.2. Description of Case 1: 2011-06-20 to 2011-06-24

The selected days are part of a convectively active period in the second half of June 2011. In this period convection over the Atlas Mountains was detected on ten consecutive days by microwave satellites (Fig. 4.5). The strongest convective cold pool event was observed in the middle of this period on 20 June. This day was selected as start date of the model run in order to reproduce this major event as close to reality as possible.

The situation preceding this convective event is shown in Fig. 5.1. On 18 June a long wave ridge located at about 20°W at 500 hPa is moving slowly eastward (Fig. 5.1c), reaching 0°W on 20 June (Figs. 5.1f and i).

5. Impact of Convective Cold Pools on the Saharan Heat Low

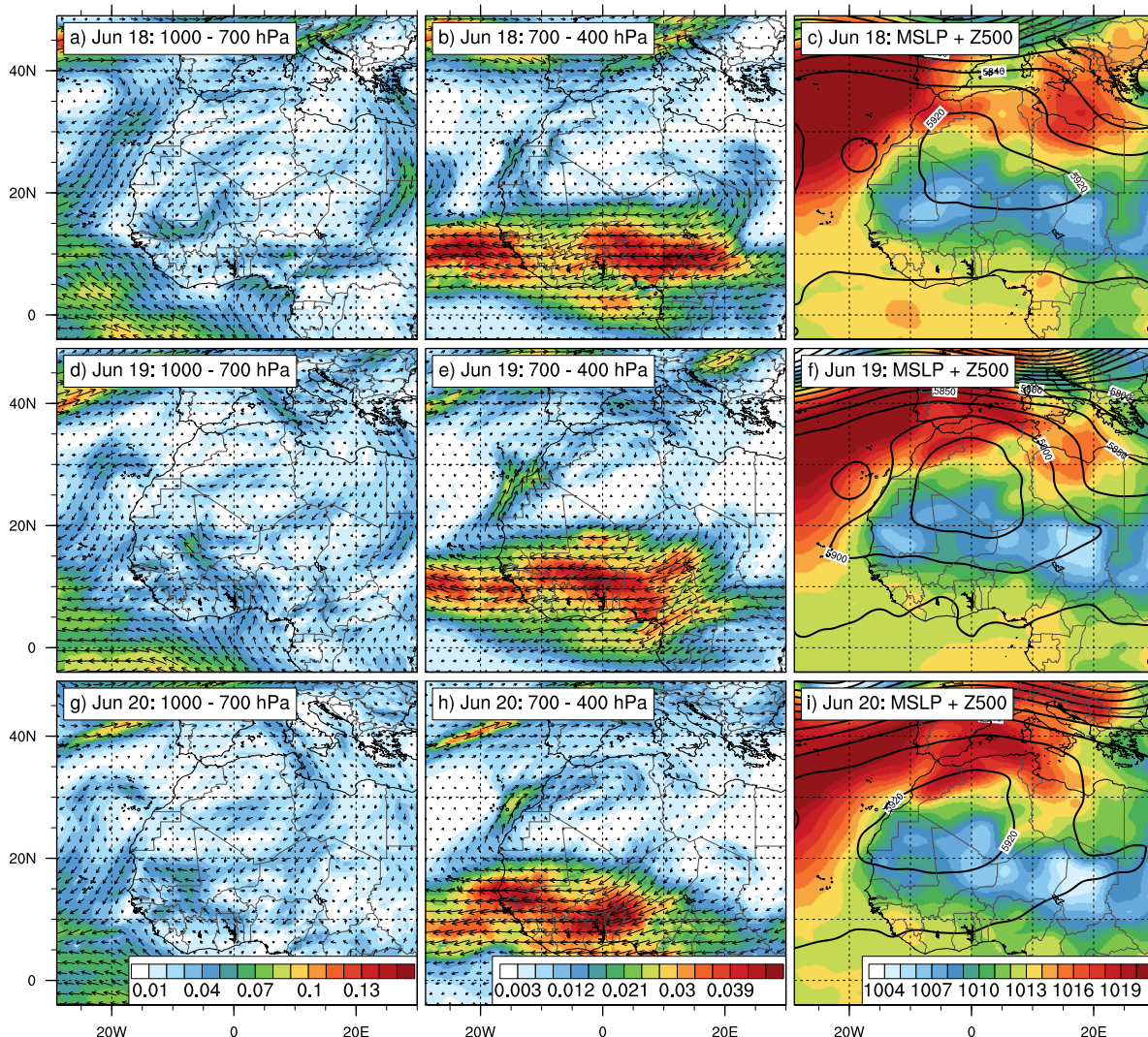


Figure 5.1.: Synoptic situation preceding the 20 June 2011 case, shown by means of the **ECMWF** operational analysis. Left column: moisture flux averaged over model layers with a nominal height between 1000 and 700 hPa in $\text{kg m}^{-2}\text{s}^{-1}$; center column: moisture flux averaged over model layers with a nominal height between 700 and 400 hPa in $\text{kg m}^{-2}\text{s}^{-1}$; right column: sea level pressure in hPa (shading) and 500 hPa geopotential height in gpm (black lines). Adapted from [Redl et al. \(2016\)](#).

At the same time the geopotential maximum above the SHL is moving westward. [Engelstaedter et al. \(2015\)](#) analyze aircraft measurements of the SHL on 22 June and note that this movement leads to a position significantly westward of the climatological mean. In this situation, the anti-cyclonic flow above the SHL is directed towards the High Atlas. The northward moisture flux averaged between 700 and 400 hPa shows values between 10 and 25 $\text{g m}^{-2}\text{s}^{-1}$ for 18–20 June (Fig. 5.1, center column). A small cut-off low, visible in the 500-hPa geopotential height map on 18 and 19 June, appears to amplify this northward flux. Located over the Canary Islands, it increases the east–west gradient in geopotential and accordingly also the northward transport of mid-level moisture. Note that this type of mid-level moisture flux out of the tropics has been shown to be instrumental in outbreaks of summer-time

5.2. Description of Case 1: 2011-06-20 to 2011-06-24

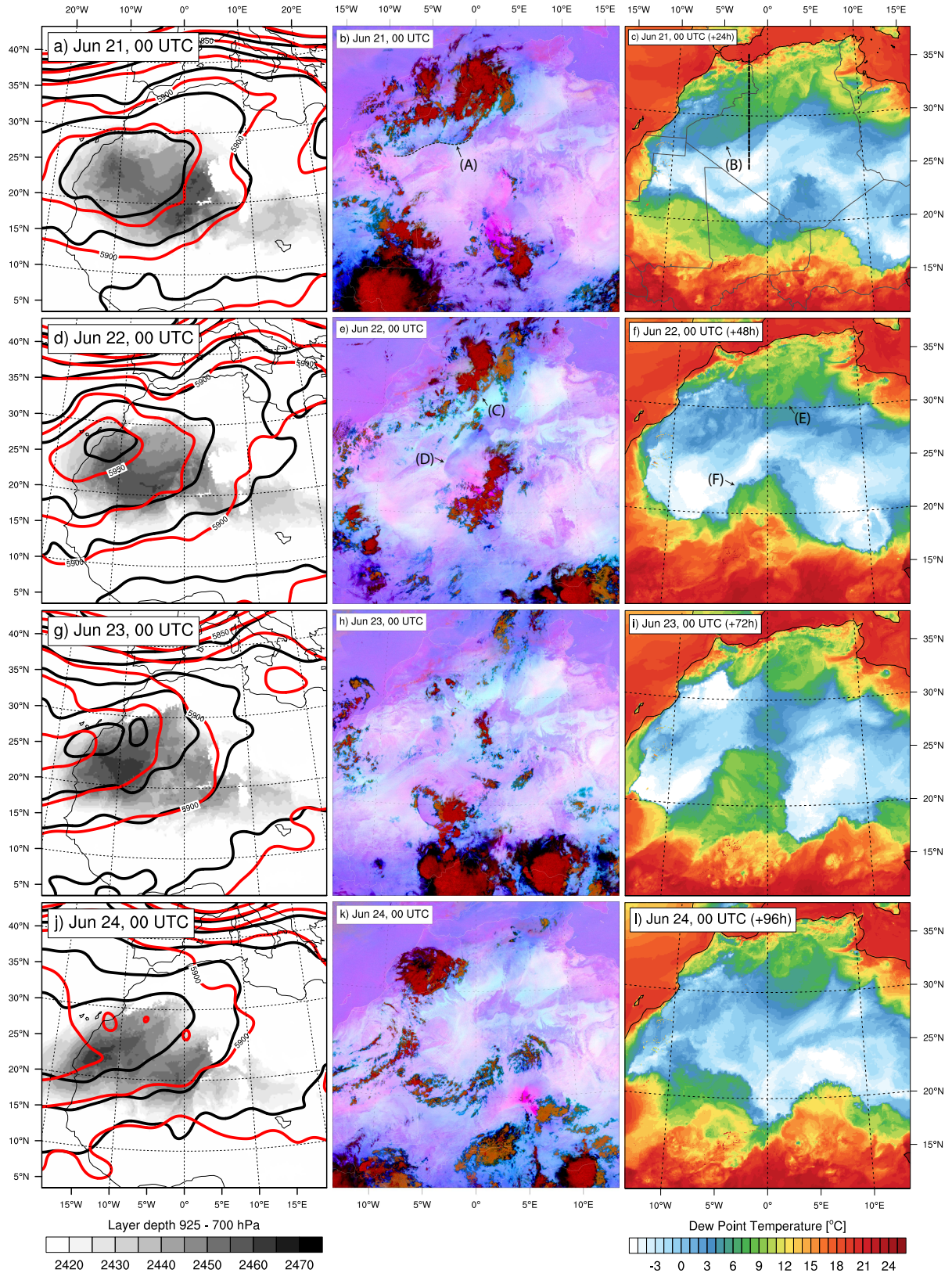


Figure 5.2.: Evolution of case 1. Left column: Geopotential height in 300 hPa from **WRF** (black lines) and **ECMWF** operational analysis (red lines) together with layer depth between 925 and 700 hPa from **WRF**. Center column: **Meteosat SEVIRI** 'Desert Dust' product. Right column: 2 m dew point temperature from **WRF**. Uppermost row: initialization time +24 h, bottom row: initialization time +96 h. The bold dashed line in (c) indicates the location of the cross section shown in Fig. 5.15. Source: Redl et al. (2016).

5. Impact of Convective Cold Pools on the Saharan Heat Low

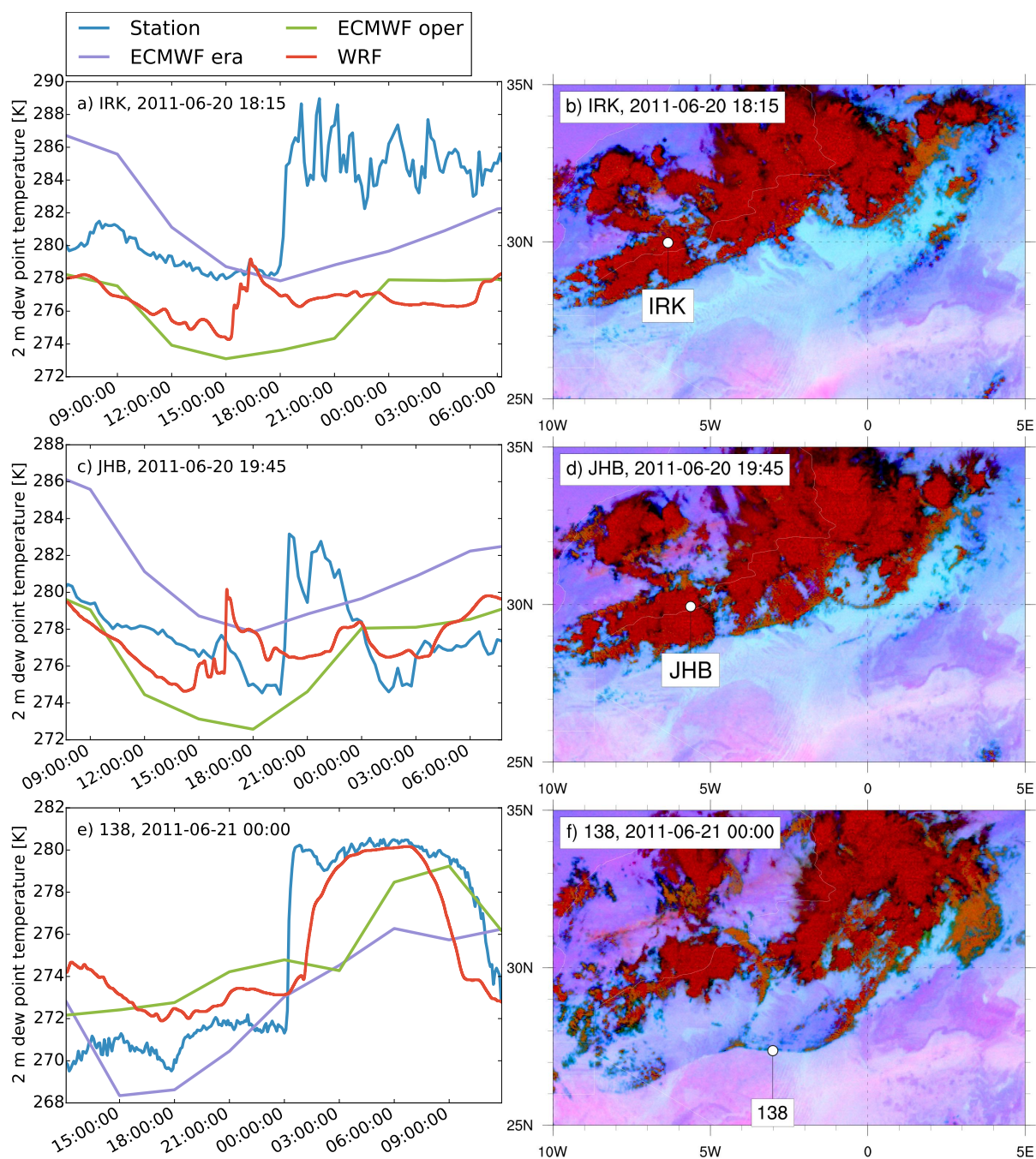


Figure 5.3.: Passage of the leading edge of cold pools at ground stations during the first simulation day of case 1. Left column: 2 m observation of dew point with simulated values from WRF, ERA-Interim, and ECMWF operational analysis. Right column: Time of the passage in Meteosat SEVIRI 'Desert Dust' product with respective station locations marked. Station numbers and abbreviations are shown in Fig. 3.5b Source: Redl et al. (2016).

convection over the Atlas Mountains in Knippertz et al. (2003). The low-level moisture flux between 1000 and 700 hPa (Fig. 5.1, left column) does not provide an additional hint on the moisture source of the event on 20 June.

The model run for this episode is initialized on 20 June, 00 UTC and integrated over 96 h until 24 June, 00 UTC. Each 00 UTC time step in this period is shown in Fig. 5.2. On the first simulation day convec-

tion is evident over the Atlas Mountains in both the model and satellite observations between 12 and 13 UTC. The development begins with individual cells and the corresponding cold pools merge during the following hours. At 18:15 UTC the system has already formed one connected cold pool with a southward moving leading edge reaching from approx. 9°W to 2°E (Fig. 5.3b). Some individual cells are located close to the IMPETUS station network. Satellite images (Figs. 5.3b and d) indicate that the stations were not hit by the connected southward moving part of the cold pool, but by smaller individual cold pools covered by high level clouds. The time shift between cold pool detection at the stations IRK (Fig. 5.3a) and JHB (Fig. 5.3b) and the increase in T_d in WRF at the same locations indicate that WRF is not able to reproduce the individual cells in strength and position. However, at 00 UTC the connected large cold pool, well visible in 2 m T_d from WRF (Figs. 5.2c, label B), matches the satellite observation in position and propagation speed reasonably well (Figs. 5.2b, label A). At this time, Fennec AWS 138 was hit by the leading edge (Figs. 5.3e and f). T_d at this station increased by about 9 K. In WRF the cold pool arrives delayed by about 1 h, leading to an increase in T_d of about 8 K. This indicates that WRF reproduces the overall characteristics of the event, but with a slightly weaker cold pool.

The ECMWF operational analysis, which is used to drive WRF, only partially reproduces the cold pool (Fig. 5.3e). Compared to measurements at IRK and JHB, the analysis is too dry by up to 4 K in T_d between 12 and 15 UTC (Figs. 5.3a and c). As one might expect from the weaker cold pool in WRF, the model is also too dry during this time.

On the second simulation day a somewhat smaller convective system forms over the Saharan and Tell Atlas at the border between Morocco and Algeria (Figs. 5.2e, label C). This event is also visible in 2 m T_d from WRF (Figs. 5.2f, label E), but with a less clear-cut leading edge. For the same day, satellite imagery shows a large cold pool formed in the central Sahara at about 23°N (Figs. 5.2e, label D). WRF reproduces this event, but too far south (Figs. 5.2e, label F). With increasing integration time, deviations to the analysis grow with some significant displacements of convective systems and contours of geopotential height in the last two integration days (Fig. 5.2g–l).

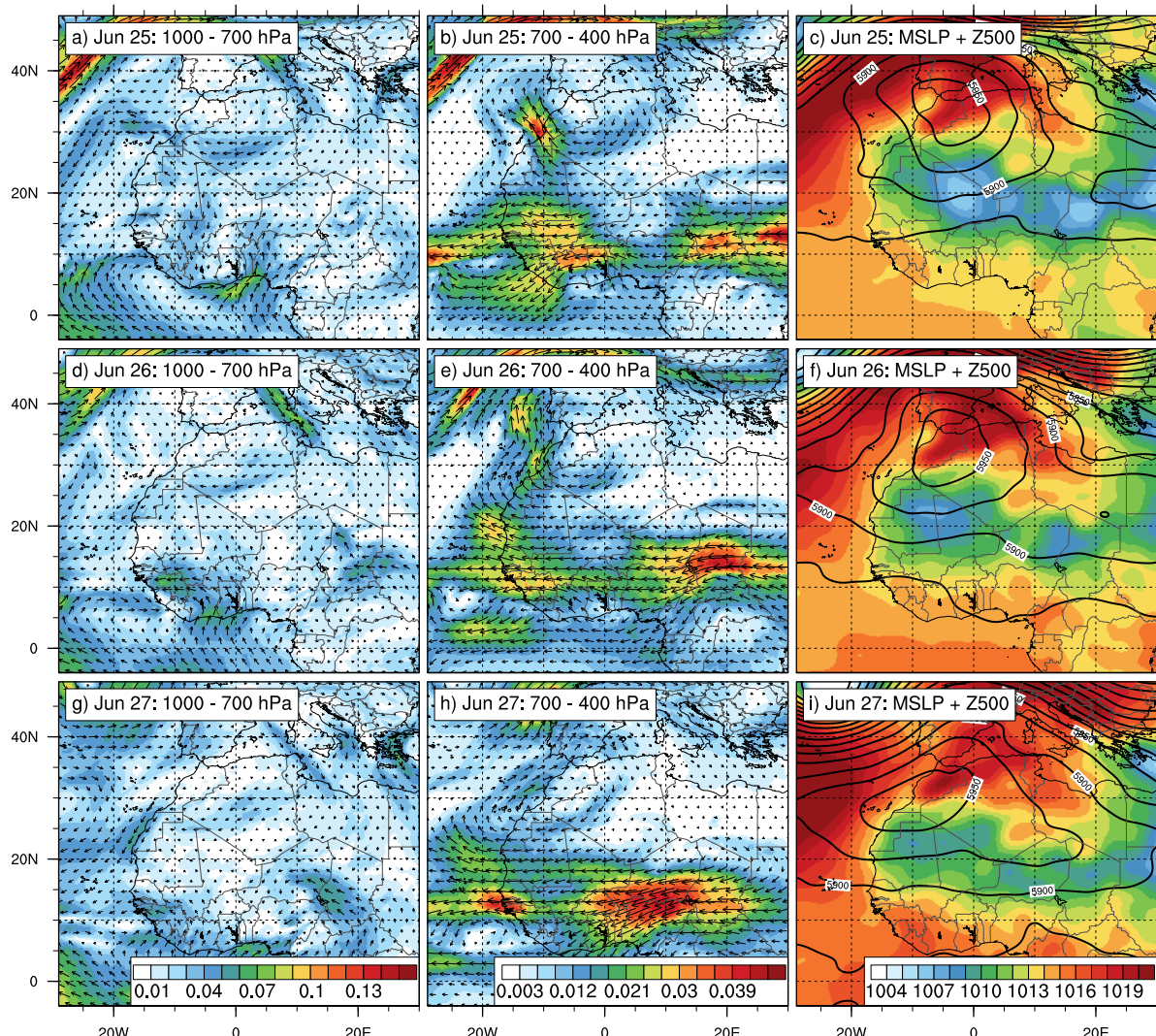


Figure 5.4.: Synoptic situation preceding the 27 June 2012 case. Panels as in Fig. 5.1. Source: Redl et al. (2016).

5.3. Description of Case 2: 2012-06-27 to 2012-07-01

Like the first case, the selected days are also part of a longer convectively active period (Fig. 4.5). For the start date of 27 June, microwave images do not indicate the strongest convective activity during this period, but a very clear cold pool is evident in IR images.

The situation leading up to this case is shown in Fig. 5.4. Similar to the first case, a long-wave ridge slowly moves eastward but the flow at 500 hPa has a stronger meridional component (Fig. 5.4, right column). On 25 and 26 June, the ridge is almost stationary at about 5°W and then moves to about 0°W on 27 June. The maximum geopotential height at 500 hPa is found over the High and Saharan Atlas Mountains co-located with a surface high on 25 and 26 June (Figs. 5.4c and f). The core of the SHL, as visible in surface pressure, moves westward during the two days preceding the event and elongates zonally to span from 10 to

5.3. Description of Case 2: 2012-06-27 to 2012-07-01

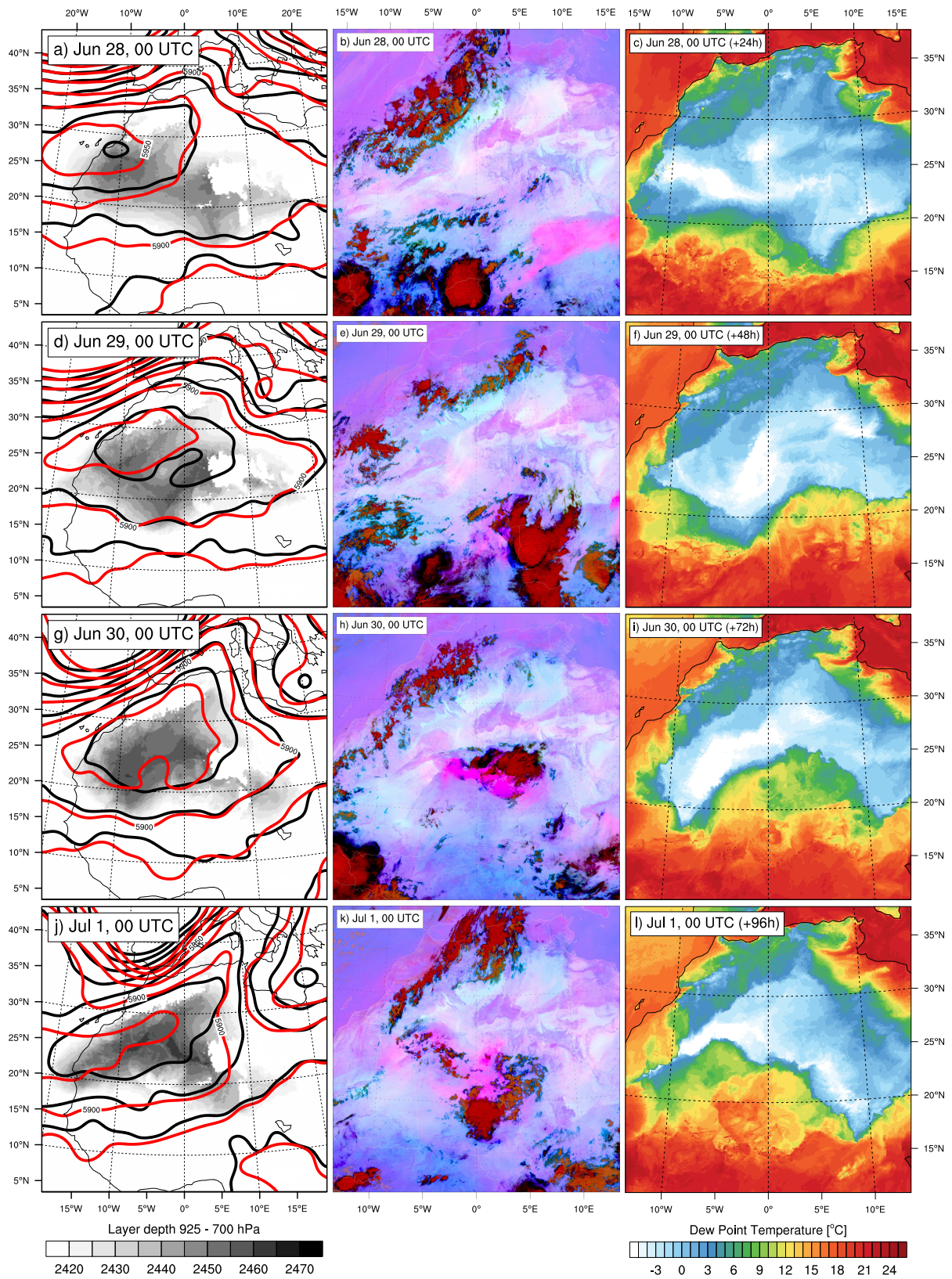


Figure 5.5.: Evolution of case 2, as in Fig. 5.2. Source: Redl et al. (2016).

5. Impact of Convective Cold Pools on the Saharan Heat Low

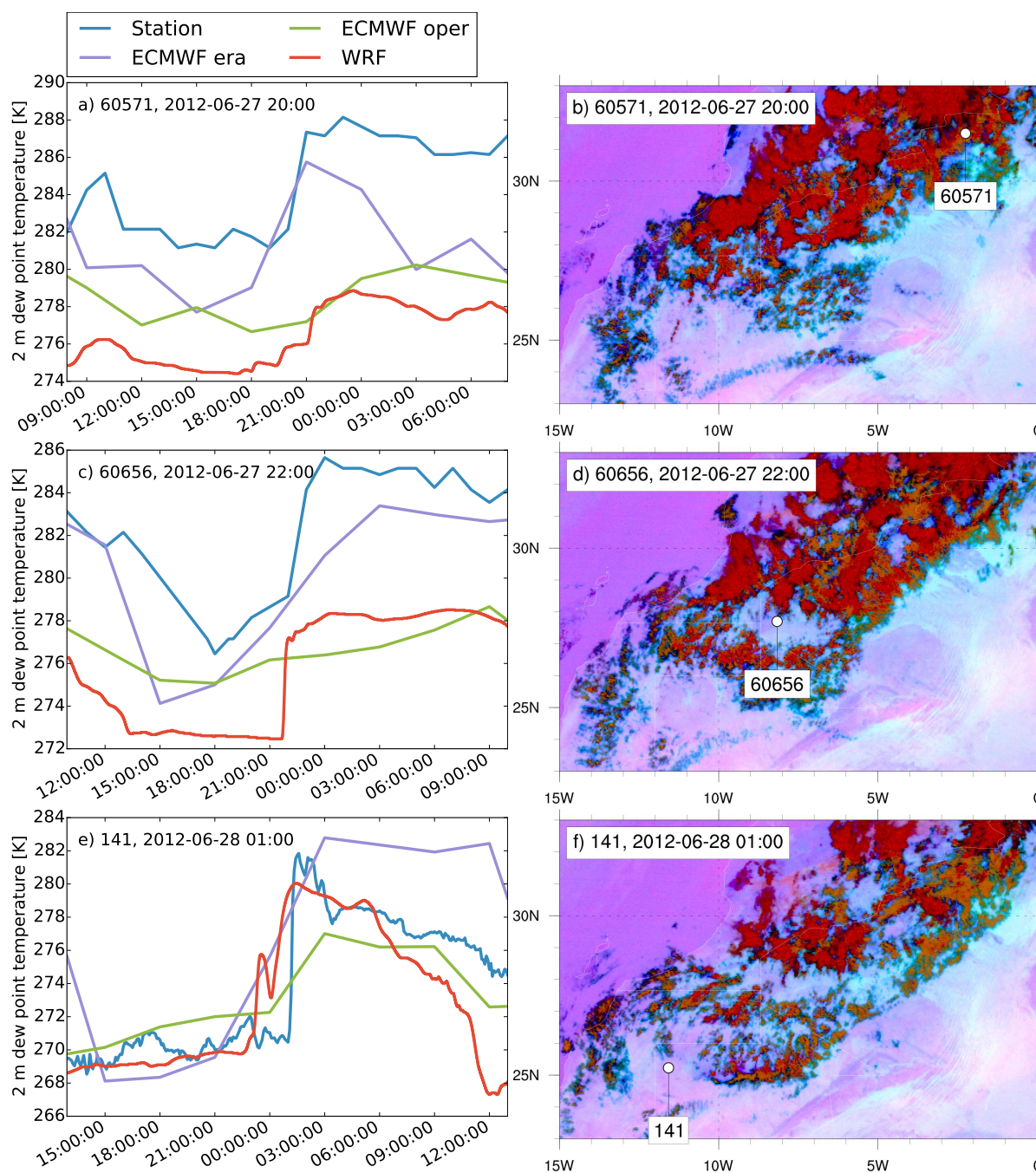


Figure 5.6.: Passage of the leading edge of cold pools at ground stations for the first simulation day of case 2, as in Fig. 5.3. Source: Redl et al. (2016).

0°W at about 23°N. In this situation, two different moisture sources are potentially feeding the convection over the Atlas Mountains: Firstly, as in the first case, northward transported moisture on the western flank of the mid-level anti-cyclonic flow (Fig. 5.4, center column); secondly, moisture from the Mediterranean Sea transported at mid-levels across Algeria at the eastern flank of the northward shifted anti-cyclone. The latter is visible in the averaged moisture flux between 700 and 400 hPa (Fig. 5.4b) and to a lesser extent between 1000 and 700 hPa on 25 June (Fig. 5.4a).

The model run for this episode was initiated on 27 June at 00 UTC and integrated over 96 h until 1 July, 00 UTC. The evolution of the simulation during the whole period is shown in Fig. 5.5. As in the first case, the development of new convective cells over the Atlas Mountains starts on the first day between 12 and 13 UTC. This time, however, the cells are more scattered throughout the region. Nevertheless, cold pools of individual cells merge again to build one large system. Unfortunately that is less visible on IR satellite images (Fig. 5.6, left column). At 20 UTC the synoptic station of Béchar (Algeria, 60571) reports a steep increase in T_d of about 6 K, indicating the arrival of the cold pool (Fig. 5.6a). WRF also shows an increase in T_d at this location, but delayed by about 1 h and weaker. Also, it is worthy of note that WRF has a significant dry bias compared to the observation of about 7 K before the event and 10 K afterwards, most likely related to the dry bias in the driving ECMWF analysis. At 22 UTC a cold pool reaches the synoptic station of Tindouf (Algeria, 60565) (Figs. 5.6c and d). Again, WRF shows a significant dry bias there of about 6 K before the event, but the timing is almost perfect. Later at about 01 UTC the Fennec AWS 141 is reached by the merged cold pool (Figs. 5.6e and f). The observed increase in T_d of about 10 K is reproduced by WRF, although not with a perfect timing. In the corresponding IR satellite image (Fig. 5.6f) the leading edge of the cold pool is hardly visible close to the station, possibly due to high levels of CWV as discussed in Brindley et al. (2012), but the arc-shaped clouds to the east of the station indicate its position.

As in the first case, the ECMWF analysis partially reproduces the cold pool (Fig. 5.6e), but much less pronounced compared to observations. Interestingly ERA-Interim, which is included for comparison in Figs. 5.3 and 5.6, reproduces the increase in T_d better than the operational analysis. The differences between analysis and re-analysis demonstrate the difficulty to simulate these events, especially in data-sparse regions like Northwest-Africa.

In the following days, the ridge moved farther eastward, which brought the subsequent trough closer to the Moroccan coast, as is well reproduced by WRF. Even after 96 integration hours, the deviation of WRF's 500 hPa geopotential field from the analysis remains small (Fig. 5.5, left column). Convection over the Atlas Mountains reaching from West Sahara / south Morocco to north Algeria is observed during all simulated days and well reproduced by WRF (Fig. 5.5, center and right column).

5. Impact of Convective Cold Pools on the Saharan Heat Low

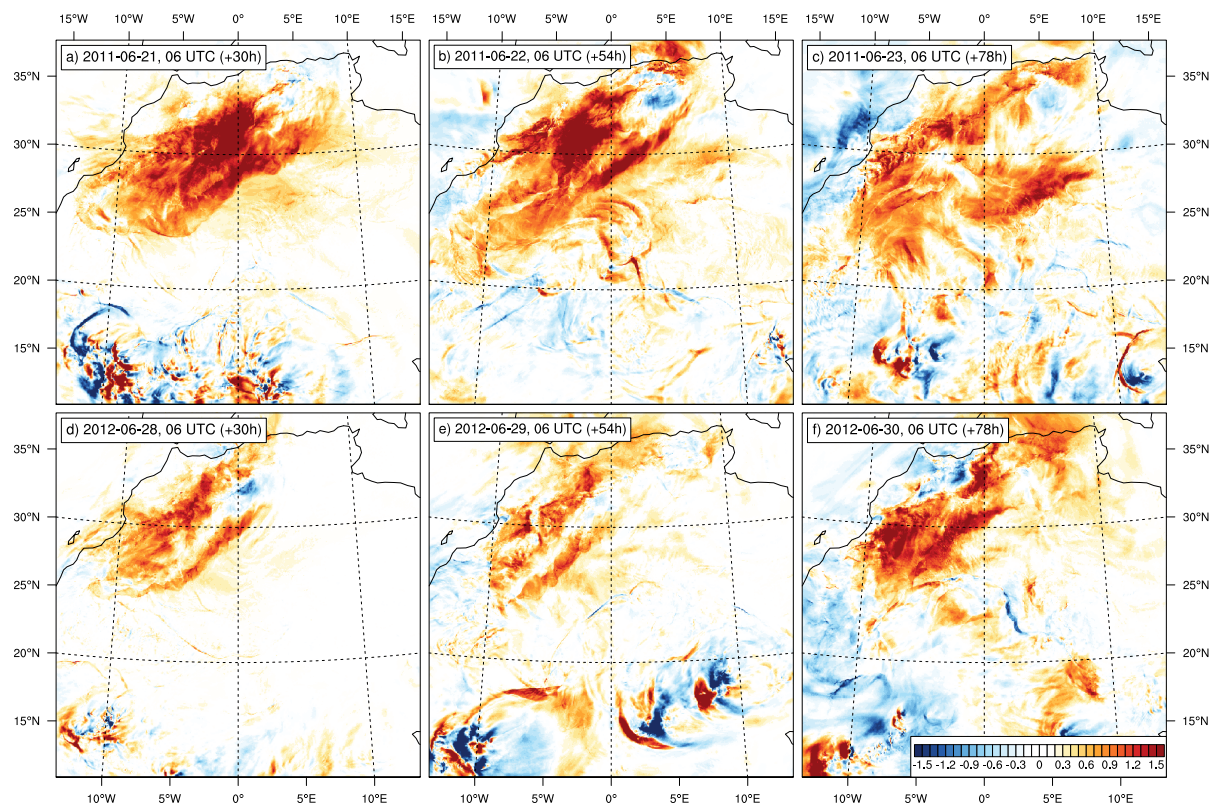


Figure 5.7.: Difference in Mean sea level pressure (MSLP) between the control and the no cold-pool runs in hPa. Upper row: case 2011-06-20, lower row: case 2012-06-27. Source: Redl et al. (2016).

5.4. Impact on Surface Pressure

The two cases described above are used to illustrate impacts of the cold pools on the SHL. In both cases the propagation of the cold pools is directed from the Atlas Mountains towards the SHL. Their leading edge becomes visible in a reduction of the layer depth between 925 and 700 hPa (Figs. 5.2 and 5.5, left column), which is often used as an indicator for the SHL position, strength, and extent (see section 1.1). The influence on the surface pressure (P_{sfc}) is analyzed using differences between the control and no cold-pool runs (section 3.2.2, third experiment).

The most pronounced effect in P_{sfc} is visible in the morning hours after the cold pool event, before the air gets heated by solar radiation and mixes vertically. All 06 UTC dates from both cases are shown in Fig. 5.7. For case 1, the first morning shows the largest effect (Fig. 5.7a). Excluding grid cells south of 20°N, an increase of at least 1 hPa (1.5 hPa) is found over an area of approx. 580,000 km² (186,000 km²) (for comparison: Morocco without Western Sahara has a size of 446,550 km²). The second case starts with a weaker increase in P_{sfc} , but the consecutive convective events produce an increase of at least 1 hPa over an area of approx. 392,000 km² on the third day (Fig. 5.7f). Relative to the pressure difference between the southern foothills of the Atlas Mountains

and the SHL core of about 5–6 hPa (Figs. 5.1 and 5.4), the magnitude of the cold-pool induced changes are substantial. That means, that the pressure gradient is increased by up to one third over a period lasting several days, which must alter the ventilation of the SHL. However, a direct effect on the SHL core around 20°N during the considered time period is not found in either of the two cases. Albeit, given the regularity of these events, it is plausible that an insufficient representation of Atlas cold pools can create a biased mean state of the SHL.

5.5. Cold Pools as Moisture Source for the Desert

Cold pools generated from MCSs in the Sahel account for nearly one third of the meridional moisture flux towards the SHL (Garcia-Carreras et al. 2013). Here, the accumulated contribution of the cold pools originating from the Atlas Mountains during both case studies is calculated using the tracer variable Q_{ev} introduced in section 3.2.3.

During the whole 96 h time period evaporation of rain over the Atlas Mountains is added and consumption by condensation is removed from Q_{ev} . The results for the end of both cases are shown vertically integrated in Fig. 5.8. For the first case study Q_{ev} shows larger values, consistent with the larger signal in surface pressure. Maximum values over north Algeria originate from fresh cold pools on the last simulation day (23 June). Values of 5–9 kg m⁻² are found over an area of approx. 142,000 km². Aged cold pools from preceding days are spread over a larger area of nearly 10⁶ km² with at least 1 kg m⁻². For the second case the total amount of moisture released over four days is smaller with an area of approx. 621,000 km² above 1 kg m⁻². For both cases the affected area is impressive, but the seemingly small integrated water vapor signals need to be seen relative to typical Saharan values, whose annual means range only from 10–20 kg m⁻² (Fink et al. 2016). For both cases, Q_{ev} values between 5–9 kg m⁻² occur where total CWV ranges from 16 to 41 kg m⁻². Averaged over this area, evaporated rain accounts for approx. one fifth of the total CWV.

5.6. Modification of Surface Radiation Balance

As discussed in section 5.5, Atlas cold pools transport a significant amount of moisture into the SHL. Increasing low-level water vapor in turn has been proposed to have a warming effect (Evan et al. 2015), especially at night-time. Here, we therefore analyze differences in long-wave radiation between the control and no cold-pool runs concentrating on 00 UTC in the first simulation night for both cases. Although cold

5. Impact of Convective Cold Pools on the Saharan Heat Low

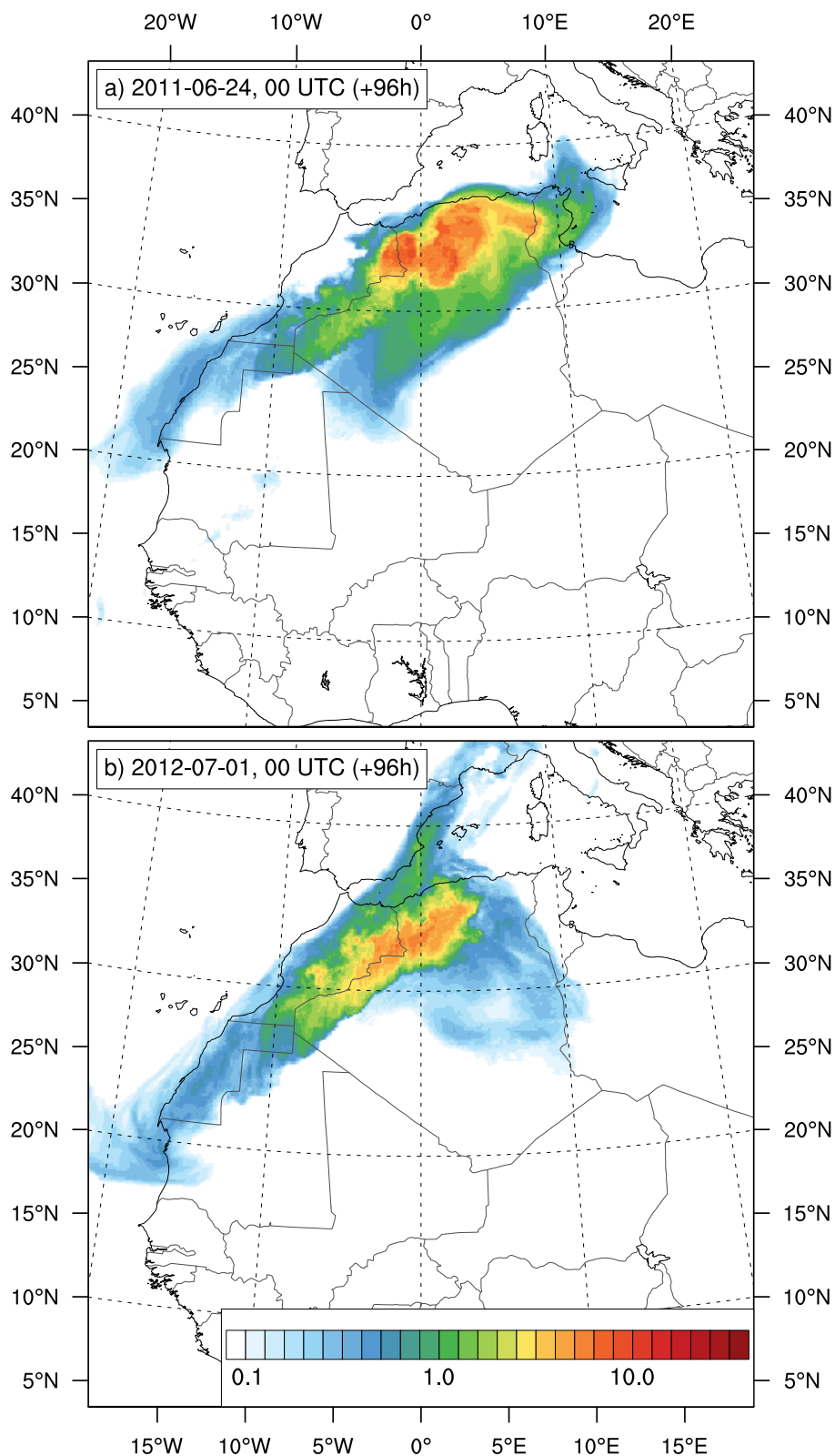


Figure 5.8.: Vertically integrated water vapor created by evaporation of rain at the end of the control runs in kg m^{-2} . (a) case 1, (b) case 2. Source: Redl et al. (2016).

pools are usually related to significant dust uplift, this aspect is here not taken into account for the radiation balance.

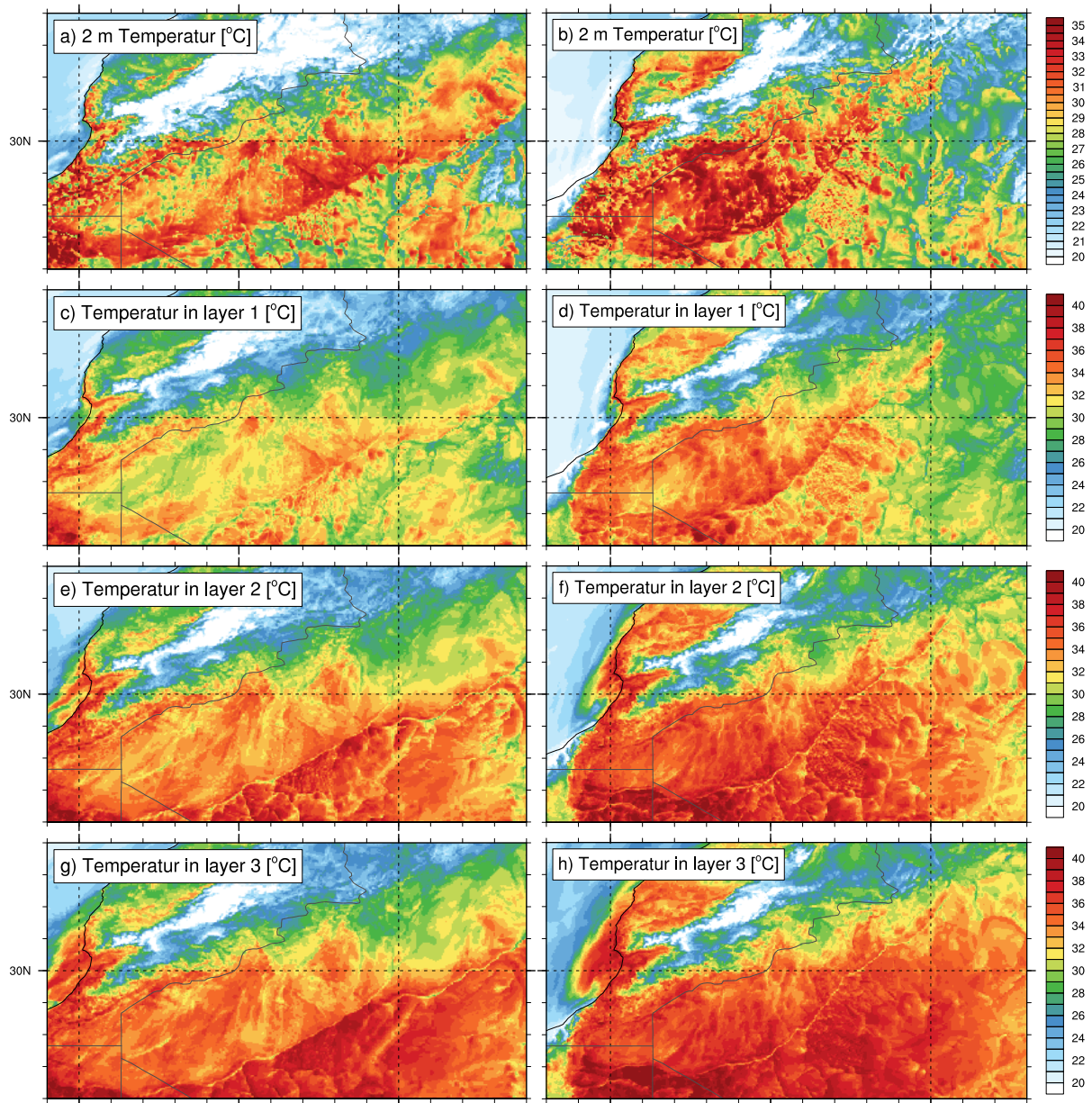


Figure 5.9.: Absolute values of air temperature in 2 m, layers 1 (approx. 0–43 m above ground), 2 (approx. 43–89 m above ground), and 3 (approx. 89–141 m above ground). Left column: case 2011-06-20, right column: case 2012-06-27. For both cases: initialization time +24 h (00 UTC of first night). Source: Redl et al. (2016).

The 2 m temperature in the region of the cold pool tends to be higher than in the surrounding desert (Figs. 5.9a and b). This at first sight counter-intuitive result has two main explanations. Firstly, the cold pool is covered by clouds (Figs. 5.10a and b) and therefore experiences less radiative cooling than the surrounding desert. Secondly, the enhanced turbulence within the cold pool and especially at its leading edge (e.g., Sun et al. 2002) mixes relatively warmer air from above the nocturnal inversion downward (Knippertz et al. 2007). There are no upper-air observations available to verify this, but model output shows a very sharp surface inversion for both cases (Fig. 5.9 and Fig. 5.11), limited to the lowest two model layers (approx. 0–89 m above ground). For the first

5. Impact of Convective Cold Pools on the Saharan Heat Low

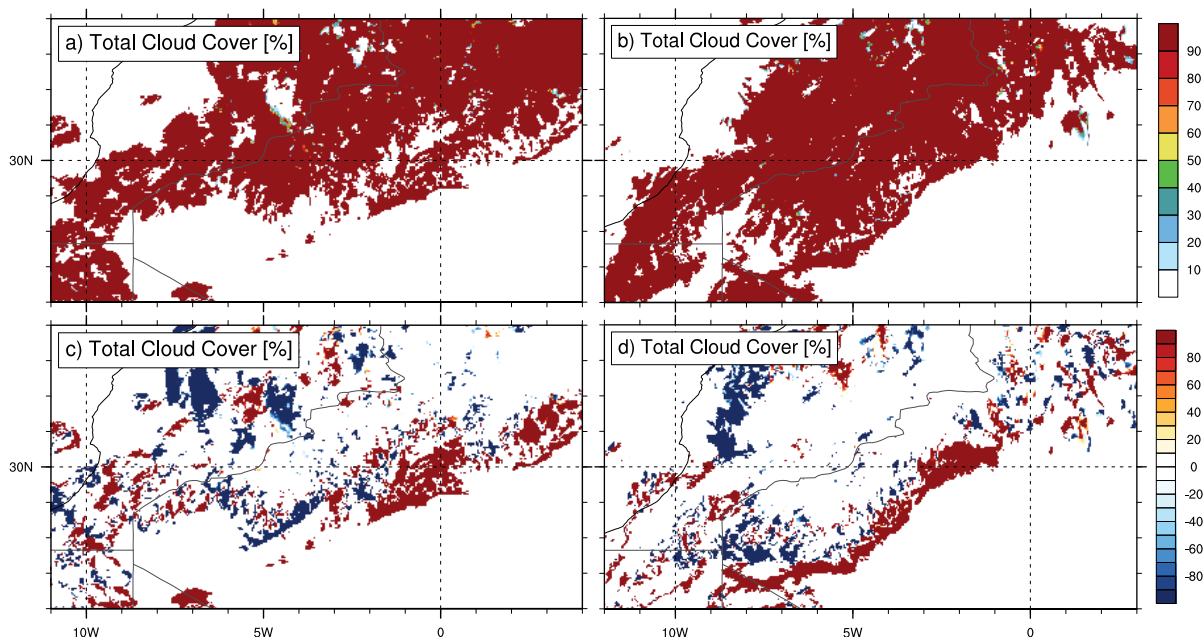


Figure 5.10.: Impact of cold pool on cloud cover. (a–b) absolute values of total cloud cover in control run, and (c–d) difference in cloud cover (control run – no-cold pool). Left column: case 2011-06-20, right column: case 2012-06-27. For both cases: initialization time +24 h (00 UTC of first night). Source: Redl et al. (2016).

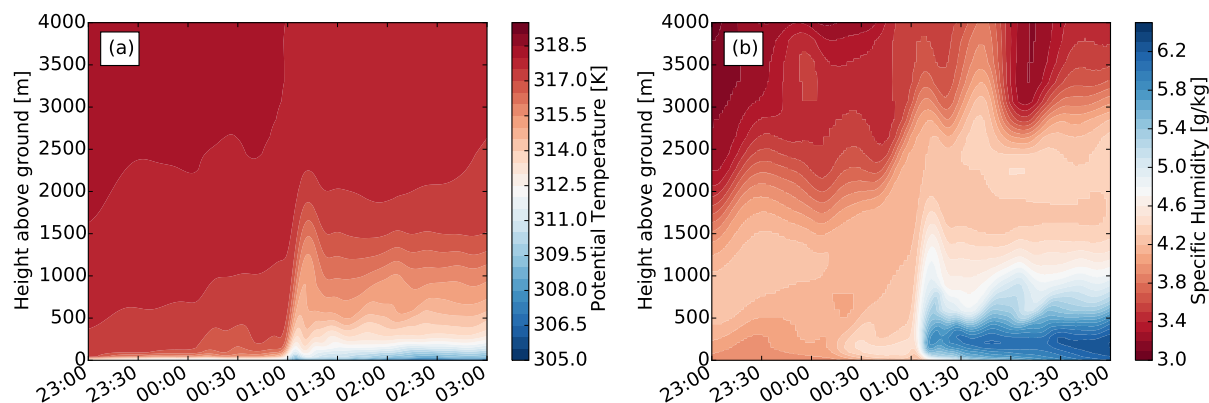


Figure 5.11.: Time series of (a) potential temperature and (b) specific humidity extracted from the control run of the first case at the location of the Fennec AWS 138. Source: Redl et al. (2016).

case, the residual layer above is well mixed with potential temperatures around 317 K (Fig. 5.11a). This near-surface inversion gets broken up by the cold pool, leading to increased temperatures at the surface. From the second layer upwards, however, the cold pool is colder than its surrounding as expected (Figs. 5.9e and f), which is mainly due to its formation through evaporative cooling. Temperature differences between the control and no cold-pool runs (Figs. 5.12a and b) show that closer to the mountains, the effect of evaporative cooling dominates leading to colder temperatures with the cold pool included, while farther into the desert the breaking up of the surface inversion dominates leading to warmer temperatures. For both cases the surface temperature signals show a very close structural match to those in up-welling long wave radiation (LW_{up}), which reaches positive values as high as 40 Wm^{-2} near the leading edge (Figs. 5.12c and d).

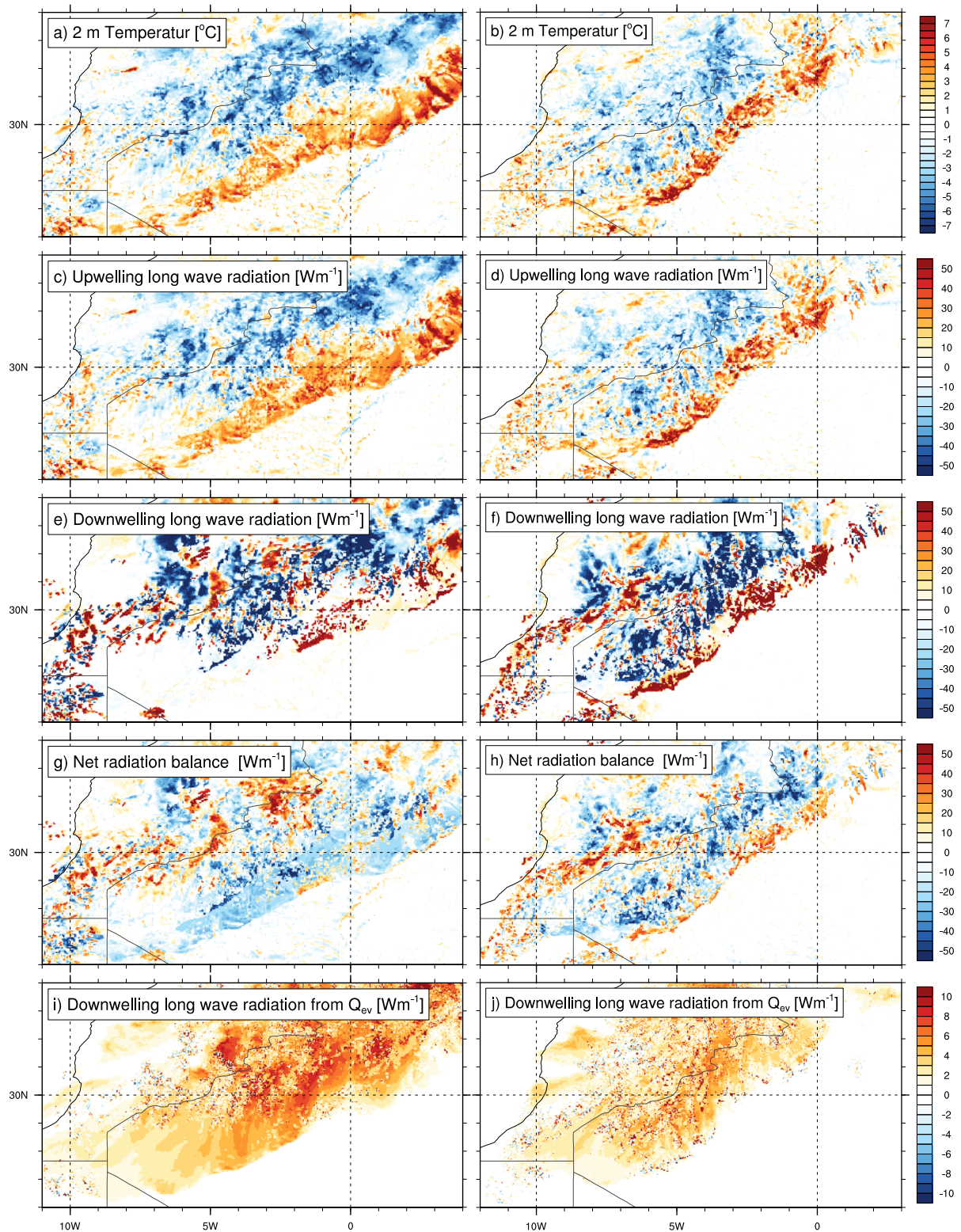


Figure 5.12.: Impact of cold pool on radiation balance and surface temperature, shown are differences (control run - no-cold pool). Left column: case 2011-06-20, right column: case 2012-06-27. For both cases: initialization time +24 h (00 UTC of first night). Source: Redl et al. (2016).

5. Impact of Convective Cold Pools on the Saharan Heat Low

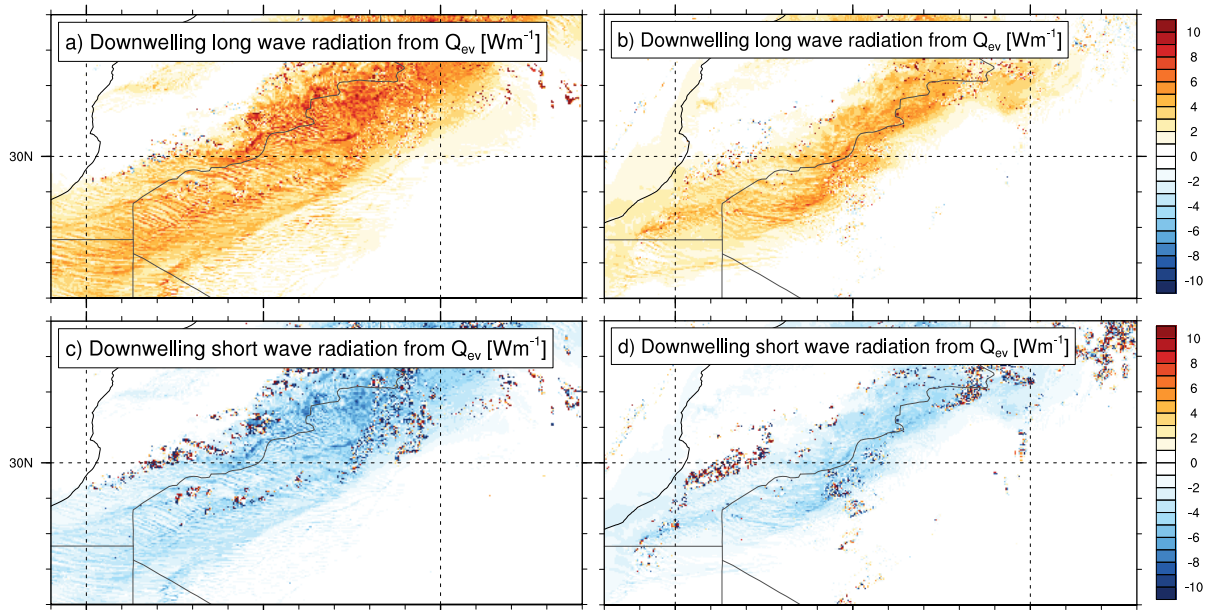


Figure 5.13.: Impact of moisture from evaporation of rain. Left: case 2011-06-20, right column: case 2012-06-27. For both cases: initialization time +36 h (12 UTC of following). Source: Redl et al. (2016).

An additional effect is the formation of arc clouds above the leading edge (Figs. 5.10c and d), which reduces radiative cooling in the control run for both cases, as reflected by positive differences in downwelling long-wave radiation (LW_{down}) relative to the no-cold pool experiments (Figs. 5.12e and f). For the second case, this cloud formation is well visible in infrared satellite images (Fig. 5.6f), but seems to be somewhat overestimated by WRF for the first case (cf. Fig. 5.3f).

What remains after the development of the day-time convective boundary layer is the additional moisture from rain evaporation, which usually gets mixed vertically much deeper than the original cold pool. The Saharan PBL can reach up to 550 hPa (Garcia-Carreras et al. 2015). Accordingly, the mixing ratio gets reduced, but the vertically integrated amount, which is relevant for LW_{down} , remains unchanged. The tracer variable Q_{ev} (see section 3.2.3) can be used to show the radiative effect of the cold pools independent of their dynamics. To do this, WRF runs were started at 00 UTC after subtracting the tracer from the full field: $Q_{modified} = Q_v - Q_{ev}$. The model was then integrated over one time step only for both original and modified water vapor fields.

Figure 5.12i and j show that the contribution of the additional moisture to the night-time radiation balance is 5–10 Wm^{-2} . Despite integration over one time step only, changes in cloud fraction occur at some grid points, leading to larger differences locally. During the following day, the magnitude of the forcing is slightly reduced, as Q_{ev} is spread horizontally over a larger area. For the first case, the area with more than 1 Wm^{-2} is increased from 0.8×10^6 to 1.2×10^6 km² from 00 to 12 UTC. In the same time the area with more than 5 Wm^{-2} decreases slightly from 229,000 to 197,000 km². The development for

the second case is comparable, but the affected area is smaller (only 36,200 km² above 5 Wm⁻² at 12 UTC). At day-time, the short-wave part of the radiation balance needs to be accounted for, too. The additional moisture has a negative impact on the same order of magnitude, but does not fully cancel out the long-wave signal (Fig. 5.13). A linear regression analysis between Q_{ev} and down-welling components of the radiation balance from both cases yields a 00 UTC value of +1.27 W kg⁻¹ in LW_{down} and 12 UTC values of +2.11 W kg⁻¹ in LW_{down} versus -1.88 W kg⁻¹ in down-welling short-wave radiation (SW_{down}). The latter values are in very good agreement with observations (+2.0 W kg⁻¹ in LW_{down} vs. -1.8 W kg⁻¹ in SW_{down}) from the Fennec super-site BBM (Marsham et al. 2015).

For both cases, the contribution of Q_{ev} to the radiation balance remains stable throughout the whole integration period, as deep convection on consecutive days compensates consumption of Q_{ev} through cloud and rain formation. The dynamical effects clearly dominate during the first night of a fresh cold pool, especially close to its origin. Nevertheless, this is very likely overcompensated during following days as the moisture remains in the atmosphere. A typical value of 5 Wm⁻² at night is likely too small to be relevant for short model runs, but becomes important for reliable climate projections, as it is in the same order of magnitude as the anthropogenic forcing.

5.7. Representation of Cold Pools with Low Resolution

Due to large computational costs, the horizontal resolution of 3 km used for the control runs and the no-cold pool runs discussed above is too fine for most regional climate projections, where typical grid spacings range from 0.22° to 0.44°. This requires the use of parameterized convection, which is known to have negative impacts on the representation of cold pools (Marsham et al. 2013a). Here this effect is quantified for the first case based on differences between the 3-km control run and model runs with 0.22° resolution and different convection schemes (Table 3.3). After 30 integration hours (06 UTC), the runs show significant differences in 2 m T_d to the control run and to a lesser extent to each other (Fig. 5.14). Higher T_d in the control run between 25°N and 30°N show an underestimation of the moisture transport associated with the leading edge of the cold pool for all schemes, while differences farther north are small or even negative. The differences south of 20°N are caused by convection in the Sahel region.

The Betts-Miller-Janjic (BMJ) and Grell-Freitas (GF) convection schemes (Figs. 5.14b and c) show particularly large deviations, while

5. Impact of Convective Cold Pools on the Saharan Heat Low

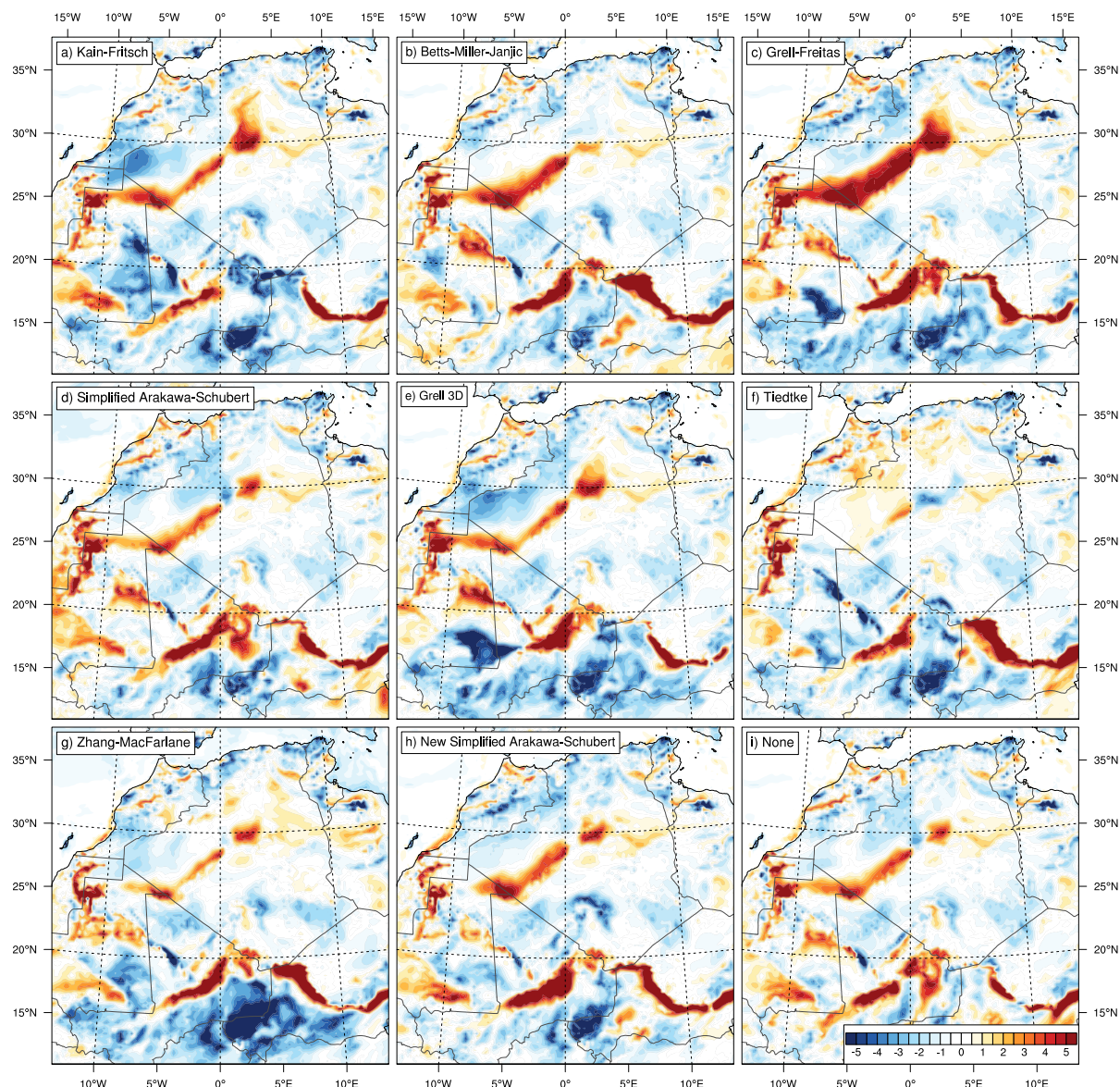


Figure 5.14.: Differences in 2 m dew point temperature between the 3 km control run and low resolution model runs (0.22°) with different convection parameterizations at 21 June, 06 UTC (+30 h) case 1. Positive values indicate wetter conditions in the control run. Source: Redl et al. (2016).

for example Tiedtke or Zhang-McFarlane (ZMF) (Figs. 5.14f and g) look surprisingly close to the control run. The leading edge of the cold pool at 06 UTC is located within the box $10^\circ\text{W}-0^\circ\text{W}$, $24^\circ\text{N}-30^\circ\text{N}$. For the GF (Tiedtke) scheme, the **Root-Mean-Square Error (RMSE)** over this box is 3.11 K (0.96 K) with a maximum bias of 7.84 K (3.88 K). This is contrary to a case study by Reinfried et al. (2009), in which Tiedtke underestimates an Atlas cold pool with a significantly worse performance than Kain-Fritsch (KF). Here, domain-wide **RMSEs** have a much smaller range from 1.89 to 2.17 K. Interestingly, using no parameterization for convection at all (Fig. 5.14i), which is not recommended for a rather coarse grid-spacing of 0.22° , leads to the smallest domain-wide **RMSE** of 1.75 K. While no general conclusions should be drawn from this result alone, it is in line with findings from Marsham et al. (2013a), Birch

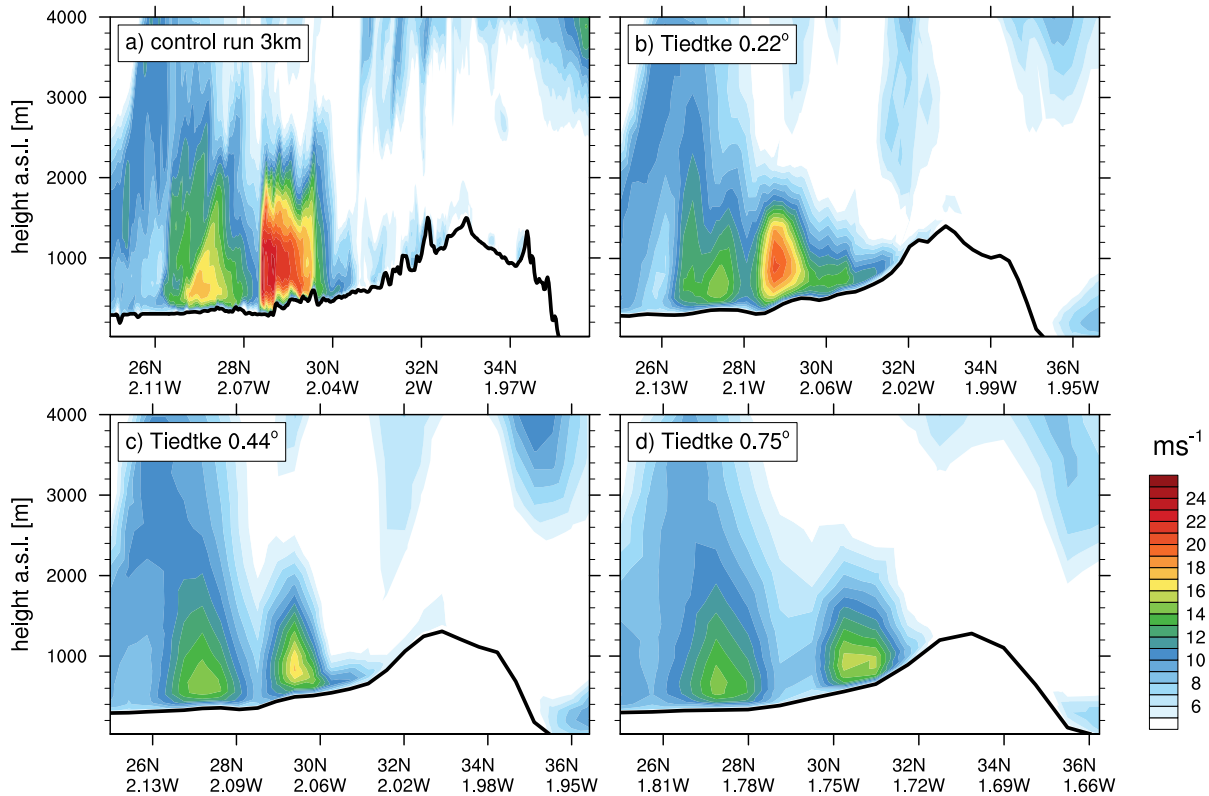


Figure 5.15.: Vertical cross-section through the cold pool of case 1 with different horizontal resolutions at 21 June 00 UTC. The location of the cross section is shown in Fig. 5.2c and Fig. 5.16a. (a) Control run, (b–d) using the Tiedtke scheme. Source: Redl et al. (2016).

et al. (2014), and Stein et al. (2015) for 12-km runs and emphasizes the need for improved schemes.

Even though all parameterization schemes produce significant biases, they do not completely fail to reproduce the cold pool in agreement with work by Reinfried et al. (2009) and Bou Karam et al. (2014). Here, this aspect is further analyzed in vertical cross sections almost parallel to the low-level wind vector at the leading edge of the cold pool in an earlier state of the simulation at 00 UTC. For these cross sections the experiment was repeated with 0.44° and 0.75° resolution, always using the Tiedtke convection scheme, which performed best in the 0.22° -experiment. In addition to the leading edge, the wind distribution highlights a second interesting feature, namely a **Night-time Low-Level Jet (NLLJ)**, somewhat south of the leading edge of the cold pool (Fig. 5.15a). The maximum wind speed within the cold pool of 24.1 ms^{-1} is reached in an altitude of about 640 m above the surface at 28.4°N . With the first decrease in horizontal resolution to 0.22° , the leading edge of the cold pool is still well visible (Fig. 5.15b). The maximum is found in the correct latitude, but somewhat smoothed to 20.4 ms^{-1} and about 140 m closer to the surface. Decreasing the resolution further to 0.44° leads to more smoothing and a maximum of 17.2 ms^{-1} . This time, the location of the maximum is about 1° farther in the north, indicating wrong timing of the event or wrong propagation speed. Also,

5. Impact of Convective Cold Pools on the Saharan Heat Low

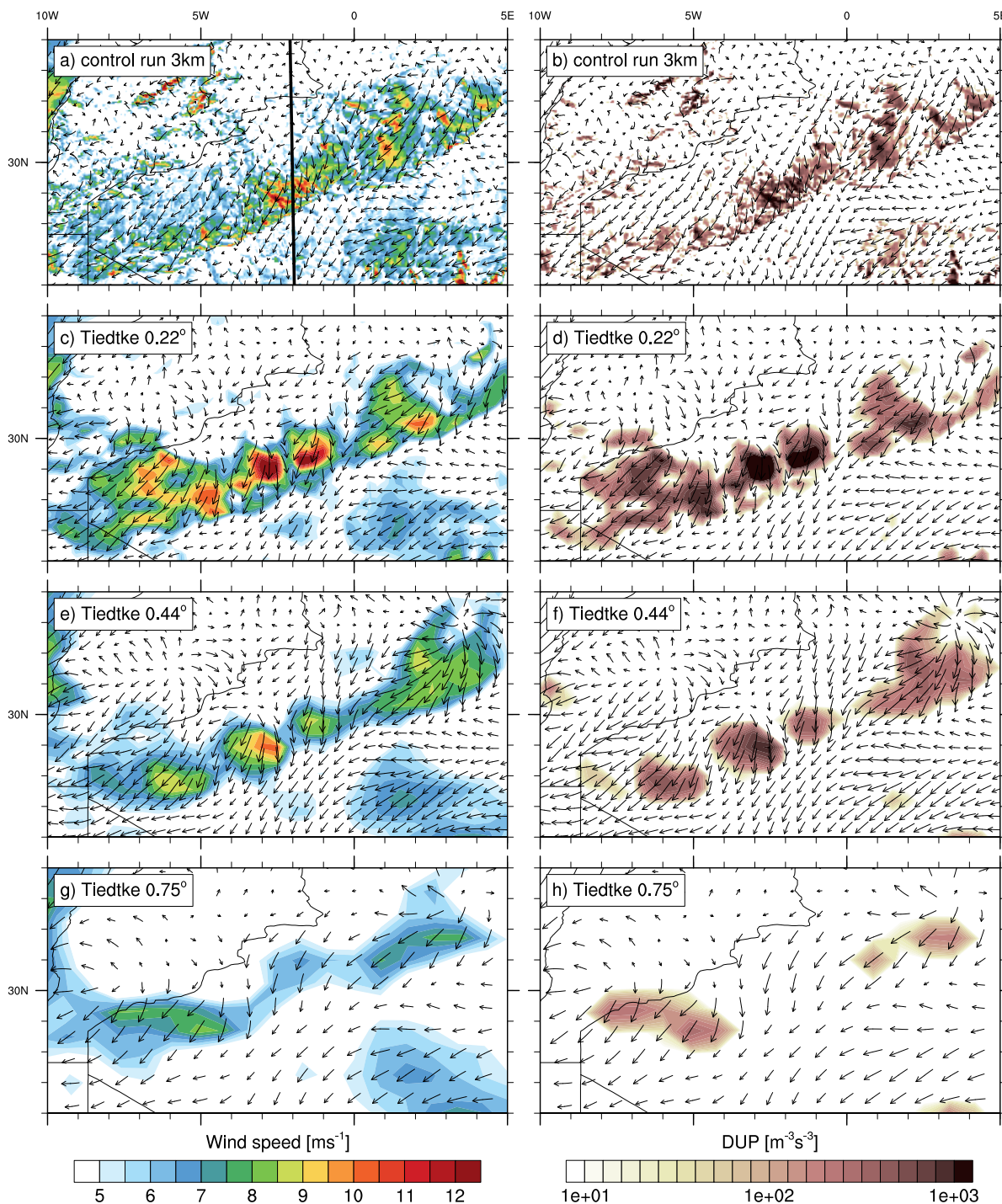


Figure 5.16.: Horizontal wind speed in 10 m (left column) and Dust Uplift Potential (DUP) (right column) for the cold pool of case 1 with different horizontal resolutions at 21 June 00 UTC. The bold black line in (a) indicates the location of the cross section shown in Fig. 5.15.

the maximum is found about 300 m closer to the surface compared to the control run. At 0.75° resolution (for example used for ERA-Interim), the wind speed maximum of the cold pool is still visible but reduced to 15.5 ms^{-1} and now significantly replaced northward to 30.2°N . The NLLJ, which is not related to the convective event, is present at all horizontal resolutions at the same location. The wind speed there is also

higher in the 3-km control run, but nearly unchanged for all lower resolutions.

The reduced wind speed has consequences for the mobilization of dust, which depends on the exceedance of a certain threshold. In this experiment, WRF was not used with an online dust emission scheme, but the Dust Uplift Potential (DUP, Equation 1.3) was applied to model output to estimate the ability of the simulated cold pools to uplift dust. A threshold of 7 ms^{-1} , the 10 m wind speed, and the vegetation fraction of WRF are used in this calculation. Unexpectedly, the wind field in 10 m from the 0.22° -experiment is not only smoothed compared to the control run but shows also larger maxima (cf. Figs. 5.16a and c). This is potentially caused by the lower elevation of the maximal wind speed in the cold pool above. The resultant DUP averaged over the area shown in Fig. 5.16 is about 131% of the DUP from the control run (cf. Figs. 5.16b and d). In the calculation of the DUP, the 3rd power of the wind speed is used. Thus, a few grid points with large values in the control run can compensate larger areas with small values in the 0.22° -experiment, which explains a visual impression of an even larger deviation between both experiments. More dust uplift with coarser resolution is not in agreement with previous studies. Reinfried et al. (2009) found a significantly reduced dust uplift in a case study with a resolution of 14 km, albeit caused by a not reproduced cold pool. Marsham et al. (2011) analyzed a ten-day simulation with 4, 12, and 40 km resolution. In the diurnal cycle starting from about 13 UTC, the 12 km run with parametrized convection had a significantly reduced DUP when compared to the 4 km run. The disagreement here is possibly only an isolated case, but could also be related to the Atlas Mountains, which provide a robust trigger for convection. For the 0.44° (Figs. 5.16e–f) and the 0.75° -experiment (Figs. 5.16g–h) the expected reduction in wind speed and DUP is found. The DUP of the 0.44° -experiment (0.75° -experiment) is about 53% (16%) of the control run. For 18–06 UTC means, a very similar ranking of DUP is found, which indicates that the results are not biased by a slightly different timing of the cold pool in the different resolutions.

From these results, it can be concluded that convectively generated cold pools cause model biases in dynamical variables that grow with decreasing horizontal resolution. Especially for the two coarsest resolutions analyzed here, i.e. 0.44° – 0.75° , these biases are reflected very pronounced in potential to uplift dust, which hampers realistic estimates unless appropriate parametrizations are in use (e.g., Pantillon et al. 2015).

6. Summary, Discussion, and Outlook

Large scale cold pools are a regular feature of convective events in (semi)-arid regions around the globe. They are especially known for the type of dust storm they create, namely the haboobs. The importance of these events for dust uplift received much attention, but their feedback on synoptic to continental scale dynamics is less well known and was not described for Northwest Africa before. This study has investigated whether, and to which extent, convectively driven cold pools originating from the Atlas Mountains can be seen as an additional pathway of ventilation for the SHL, whose characteristics are a key area of current research regarding the WAM (Janicot et al. 2015). The question was split into two parts, the analysis of the regularity and spatial distribution by means of an automated detection algorithm, and the detailed diagnosis of two example cases by means of sensitivity experiments with the WRF model. Combining the results of both steps helps to understand biases in state-of-the-art analysis and re-analysis products.

6.1. Spatio-Temporal Variability of Cold Pool Activity

The first part of the study has investigated the possibility to create long-term climatologies of convective cold pool events based on routine surface observations and microwave satellite data, both freely available worldwide. The main findings from this part are:

- The presented method is well suitable for the objective, automated, and reproducible creation of long-term climatologies of the rather complex quantity of convective cold pool occurrence.
- The method is applicable to surface observations of different temporal resolution. It was shown that comparable results are achievable with automated weather stations, which offer a high temporal resolution, and with WMO standard reports from synoptic stations and airports, which at best offer a temporal resolution of 30 minutes.
- It was further shown that results obtained only from satellite information are a reasonable proxy for the occurrence of surface

cold pool events in semi-arid regions. This is particularly relevant for applications in remote areas like deserts, which lack a dense surface station network. But it should be noted that at least some surface stations are necessary to estimate a relation between convection detected by satellites and the occurrence of cold pools. This relationship may vary from region to region.

- The algorithm was applied to Northwest Africa and the time period from 2002 to 2014. In the region south of the Atlas Mountains from Morocco to Tunisia the regularity of cold pool events could be demonstrated. For the months May to September, 2.3 (IMPETUS stations) to 5.9 (ISD stations) events were detected. Using satellite information only, it was further shown that convective events in the region of study are not regularly or randomly distributed in time, but tend to cluster into convective periods of five days, which often include strong events at two consecutive days.

Some sources of uncertainty remain with the presented method. The number of cases depends, at least to some extent, on the chosen thresholds for station and satellite data and also on data availability. Instrument failures on the ground, as well as on the satellites, could result in missed cases. Also, false positives are possible in complex synoptic situations where deep convection is embedded in a frontal system. In such cases, the method cannot distinguish between the leading edge of a cold front and a cold pool, as both have characteristics of density currents. However, the created climatologies are a valuable source of information for model evaluation. A direct comparison is possible when a satellite simulator like RTTOV-SCATT (Bauer et al. 2006) or ARTS (Buehler et al. 2005a) is applied to the model output.

Applying the developed cold pool climatology algorithm to other regions with documented occurrence of haboobs can help to address the open question of the relative importance of these events (Williams 2008; Engelstaedter and Washington 2008) for total dust emission, especially when the created climatologies are combined with observations of dustiness or model experiments investigating individual cases. Steps forward for this research question with regard to the Sahara were recently made for cold surges (Fiedler et al. 2015) and Night-time Low-Level Jets (NLLJs) (Fiedler et al. 2013) on the climatological time scale. The algorithm presented here potentially adds a climatological perspective to studies investigating relative importance of cold pools on shorter time-scales like Heinold et al. (2013) or Marsham et al. (2013b).

Even if the method is designed to be as universal as possible, it is still not effortless to use it in other regions. In addition to the large amount of necessary satellite data to be processed, the criteria for the screening of station data need to be reviewed and potentially adapted. The

leading edge of cold pools is always characterized by high wind speed, but its passage is not necessarily accompanied by an increase in dew point temperature in wetter environments (Parker et al. 2005; Provod et al. 2015). The US deserts in the Southwest and the Great Plains are expected to be particularly suitable due to the relatively dense METAR station network with hourly or higher-resolved observations. The available Doppler radar network could be used as an additional source of information.

6.2. Impact of Cold Pools on the Saharan Heat Low

For Northwest Africa, the importance of convective cold pools is already emphasized by the regularity of their occurrence but gains additional weight through the clustering in several-days long periods. Cold pools typically form in the afternoon and spread over hundreds of kilometers until the early morning hours. In the second part of this study, two cold-pool periods were selected to explore to what extent the associated changes in temperature, moisture, surface pressure, clouds, and radiation affect the strength and position of the SHL, a notoriously ill-reproduced part of the WAM system due to limited observations and often large model biases. The analysis is based on sensitivity experiments and a moisture tracking approach based on numerical simulations using the WRF model in convection-permitting and coarser resolutions. The main findings from this part are:

- Surface pressure is significantly increased by 1–1.5 hPa along the northern fringes of the SHL over the length of the convective period.
- A significant amount of moisture is transported into the desert by cold pools, such that about one fifth of CWV comes from evaporated rain after large convective cold pool events.
- Effects of a very recent cold pool event on the night-time radiation balance are dominated by dynamic effects. The cold pool removes energy from the lower troposphere through cold air advection, but more importantly by the turbulent downward transport of sensible heat to the surface and resulting increased up-welling long-wave radiation. However, arc clouds often form above the leading edge of the cold pool and reflect a part of the increased up-welling radiation back.
- Beyond these initial effects, the additional moisture injected into the SHL becomes important due to its greenhouse gas effect. Down-welling long-wave radiation is increased by about 5 Wm^{-2} at day and night, which at day-time is partly compensated by reduced short-wave radiation.

- The representation of convective cold pool events deteriorates with decreasing horizontal resolution and the use of a parameterization for deep convection. Even with a relatively coarse grid spacing of 0.22° a run without convection parameterization outperformed eight runs with different parameterization schemes.

Despite the marked impacts of cold pools, the increase in surface pressure did not directly affect the core of the SHL in both cases, probably because the integration time was not long enough for the increased pressure gradient to unfold its full impact. In longer model runs, growing errors due to missing or ill-represented cold pools can be expected. For tropical West Africa, [Marsham et al. \(2013a\)](#) and [Birch et al. \(2014\)](#) showed that the effect of misrepresented convection due to parameterizations can already be substantial after only one integration day with significant changes in the location and timing of deep convection. The latter is less significant over the Atlas region, where the mountains provide a stable trigger for convection, such that the effect of coarse resolution and parameterizations are comparatively less important.

[Evan et al. \(2015\)](#) related the deepening of the SHL during the past decades and the simultaneous recovery from the Sahel drought in the 1970s to an increasing amount of water vapor in lower levels in the SHL region. The results presented here suggest that cold pool events from the Atlas Mountains form an important contribution to the availability of water vapor in this region. The misrepresentation of convective cold pools with low resolution and parameterized convection is possibly one of the reasons why [Evan et al. \(2015\)](#) found a too weak positive trend in Sahel precipitation for the past decades in [Coupled Model Intercomparison Project Phase 5 \(CMIP5\)](#) models. However, the additional moisture from cold pools usually comes in combination with dust emitted at their leading edge. Both quantities are highly correlated to each other and counteract each other with respect to the radiation balance ([Marsham et al. 2015](#)). The lower simulated wind speeds found with cold pools from parameterized convection in experiments with low resolution lead to a significantly underestimated dust emission. It is therefore possible that this underestimation and the related higher short-wave down-welling radiation compensates part of the effect of lower long-wave down-welling due to a reduced water vapor mixing ratio.

The underestimated dust emission is not evident for the resolution of 0.22° , but very clear for 0.44° and 0.75° . This is not in agreement with previous studies in which parametrized convection lead to significantly reduced dust emission already at resolutions of 12–14 km ([Reinfried et al. 2009](#); [Marsham et al. 2011](#)). This discrepancy highlights the uncertainties arising from parametrization schemes without proper consideration of convective cold pools and fits well to the examples of the

ECMWF (re)-analysis shown in the introduction (Fig. 1.1), where some cold pools are reproduced satisfactory and some not at all.

6.3. Future Perspectives

Studies with focus on the variability of the SHL on the synoptic to sub-monthly time scale found the leading mode of variability in the 10–30 days band to be related to upper-level troughs at the northern flank of the SHL. Even though not examined in closer detail, the return period of convective episodes identified by the climatology algorithm also seems to belong to the same frequency band. This, and also the synoptic situations discussed in both of the case studies, suggests that the convective episodes are related to mid-latitude upper-level troughs as well. Possibly, a part of the SHL variability in this frequency band even originates from the influence of cold pools. A composite analysis, based on the AMCI, could help to identify synoptic situations with an increased probability of convective cold pool occurrence. Knowledge of such situations can support operational forecasters who can not rely solely on uncertain model forecasts.

The frequent occurrence of cold pools at the southern flank of the SHL along the ITD is a source of large biases due to misrepresentation of these events in (re)-analysis products, especially in the distribution of moisture (Roberts et al. 2014). Results presented here suggest that biases at the northern flank are related to the same process, especially as the spatio-temporal evolution of these biases closely resembles the evolution of the cold pool activity. Accordingly, the quantification of cold pool occurrence in other comparable regions would not only be beneficial for future studies focusing on dust emission, but also for the understanding of biases in moisture distribution and cloudiness. Once regions with above-average activity of cold pools are identified, target-oriented implementation of operational upper air observations or ground based remote sensing could help to improve forecast and analysis products. For the model representation of the SHL, a positive impact could be expected from additional observations at the southern flank of the Atlas Mountains, e.g., in Tindouf (60656), Béchar (60571), Laghouat (60545), and Tozeur (60760). However, as shown during AMMA, additional observations can reduce uncertainties in the initial state of a model, but advantages are not preserved for forecasts without improved representation of physical processes (Fink et al. 2011).

The methods of cold pool removal have been labeled ‘unphysical’ in section 3.2. Surprisingly perhaps, this unphysical setup is quite close to many regional model experiments conducted to investigate the WAM. Examples are Marsham et al. (2013a) or Birch et al. (2014), both focused on Sahel convection with the same model setup. Their northern

domain boundary did cut through the Atlas Mountains, which means that boundary conditions are provided by a larger scale model not able to represent convective cold pools realistically. Accordingly, the outflow of convective events outside their domain is missing. Resultant biases in the pressure gradient and moisture distribution may cause a biased state of the SHL. Another example is Klein et al. (2015), where authors analyzed the impact of different parametrizations schemes on the representation of the WAM using WRF while their domain reached northward to about 26°N only. This common practice of small domains in regional modeling is owed to high computational costs, but possible effects are usually not discussed. A follow-up study could investigate dynamical consequences of not including strong orographic triggers for deep convection like the Atlas Mountains in longer model runs. Results are potentially relevant for the regional down-scaling of climate projections.

Generally, the results presented here add to a growing body of work that helps to understand the long-standing problem of misrepresentation of the WAM and its variability in many models and across timescales. Cold pools in the Sahel and, as shown here for the first time, from the Atlas Mountains and their insufficient representation should be in the focus of future attempts to improve models for weather prediction and climate projections in northern Africa. Recently, some effects of cold pools have been added to existing parameterization schemes such as dust emission (Pantillon et al. 2015) or effects on temperature and moisture (Grandpeix and Lafore 2010). But these can not fully represent possible upscale effects of cold pools on the SHL, which in turn may feedback on the convection itself. Improved climate projections for the WAM are only achievable if all aspects are taken into account. This also includes a proper representation of the complex Saharan boundary layer, which ultimately distributes moisture and dust on the continental scale (Garcia-Carreras et al. 2015). Developments of new parametrization schemes as well as existing weather and climate models should be assessed by means of long-term observational datasets, such as the climatology presented here.

A. Appendix

A.1. Noise Detection in Microwave Satellite Data

Convection screening in microwave satellite data was initially done by searching for positive *BTD* between the 183.3 ± 1 and 183.3 ± 3 as well as 183.3 ± 1 and 183.3 ± 7 channels, following [Hong \(2005\)](#) and [Xu et al. \(2009\)](#). Comparison with the cold pool climatology created by [Emmel et al. \(2010\)](#) for 2002–2006, gave no reason to concern about the reliability of this method. However, extending the period resulted in a number of obvious false alarms caused by noise in one or more of the 183.3 GHz channels. Information published on the [Polar Orbiting Environmental Satellites \(POES\)](#) spacecraft status page¹ contain reports about instrument failures, but are not conclusive about the usability of the data. Also, quality flags included in raw data files obtained from [CLASS](#) do not indicate irregularities related to noise, not even for significantly noise affected overpasses, like the one shown in Fig. A.3. An

¹POES spacecraft status page: <http://www.ospo.noaa.gov/Operations/POES/status.html>

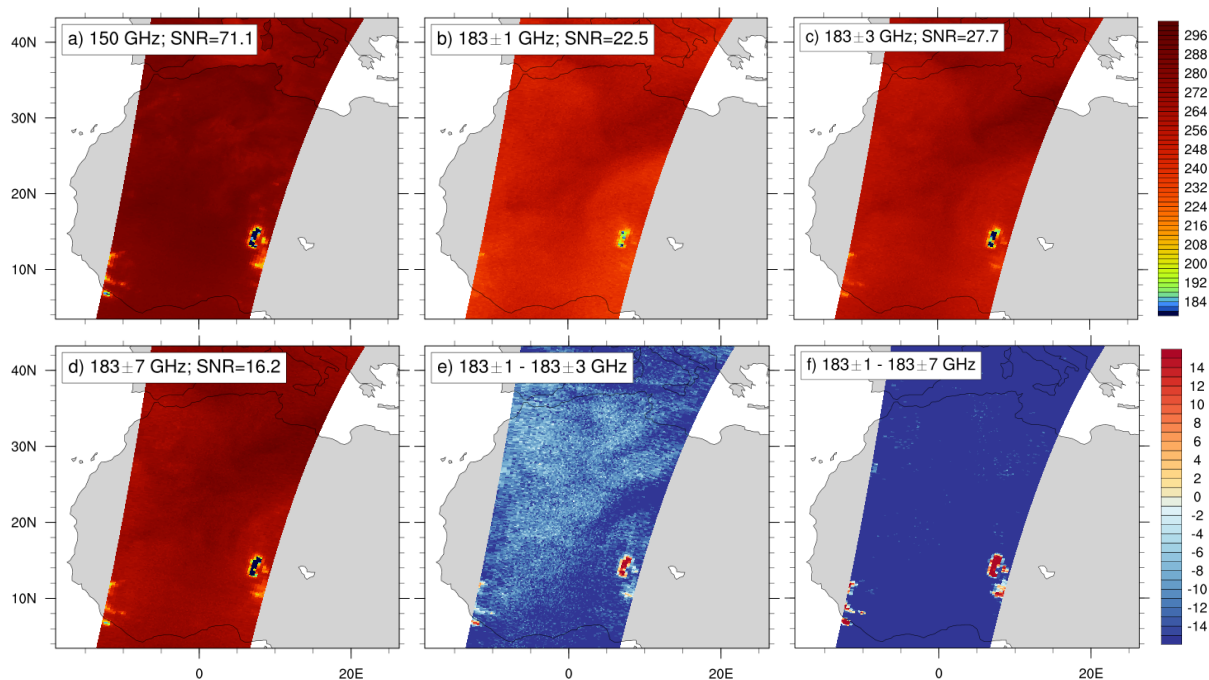


Figure A.1.: Example for data with a signal-to-noise ratio around 20 in 183.3 GHz channels. Satellite: NOAA-16, date: 2007-08-04 04:10 UTC. Panels: (a–d) brightness temperatures in K (upper label bar), (e–f) brightness temperature differences in K (lower label bar).

A. Appendix

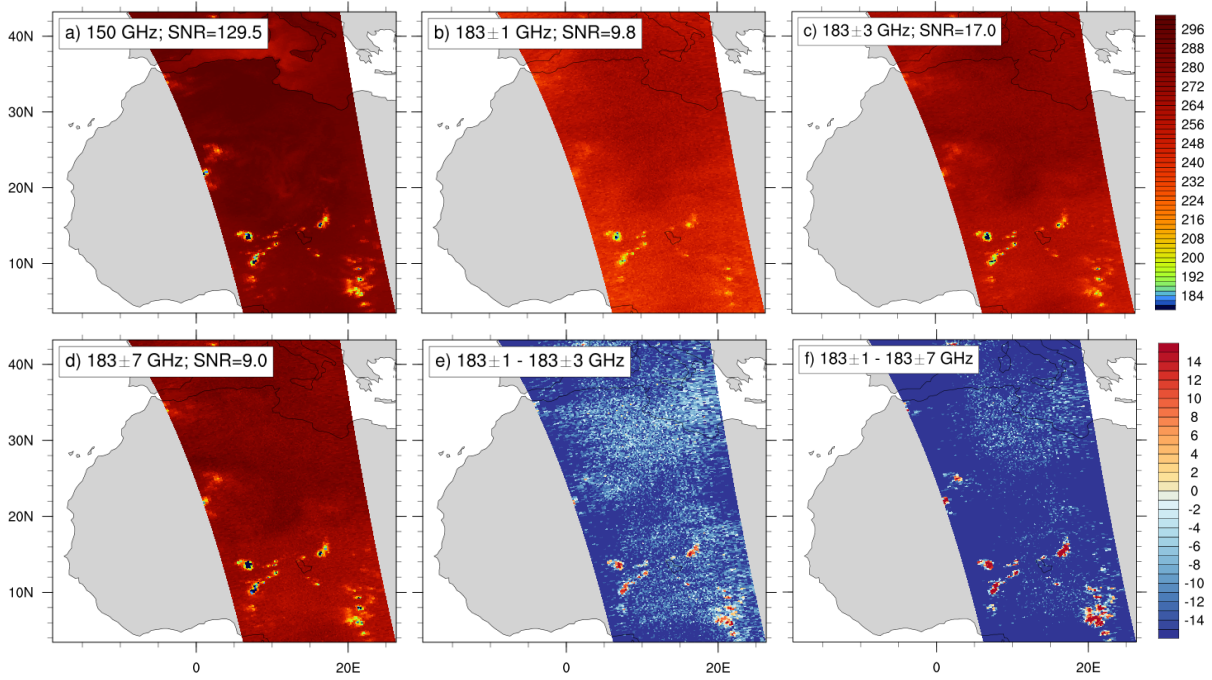


Figure A.2.: Example for data with a signal-to-noise ratio around 10 in 183.3 GHz channels. Satellite: NOAA-16, date: 2008-08-04 15:49 UTC. Panels as in Fig. A.1.

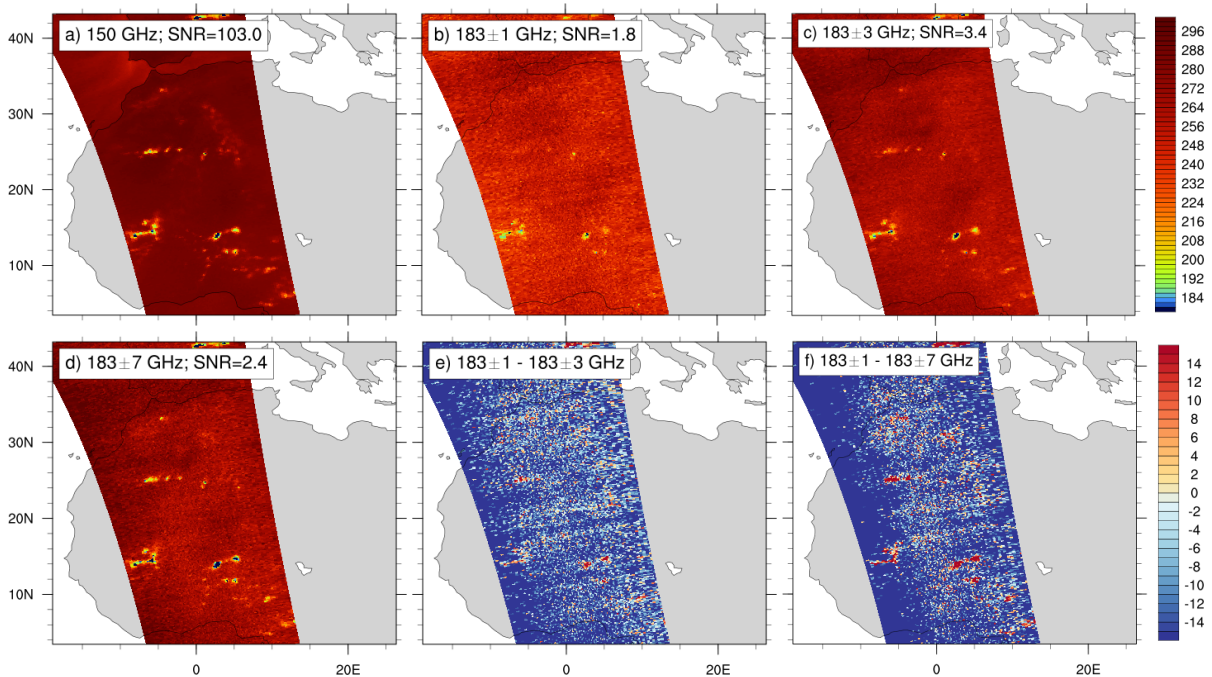


Figure A.3.: Example for data with a signal-to-noise ratio around 2 in 183.3 GHz channels. Satellite: NOAA-16, date: 2010-08-01 18:31 UTC. Panels as in Fig. A.1.

inspection by eye of individual overpasses would have been possible, but inappropriate as part of an otherwise automated algorithm.

The issue was addressed by the application of an algorithm developed for estimation of noise induced variance in photographs. It is described in detail in [Immerkær \(1996\)](#), here only information necessary for reproduction without complete mathematical derivation are given.

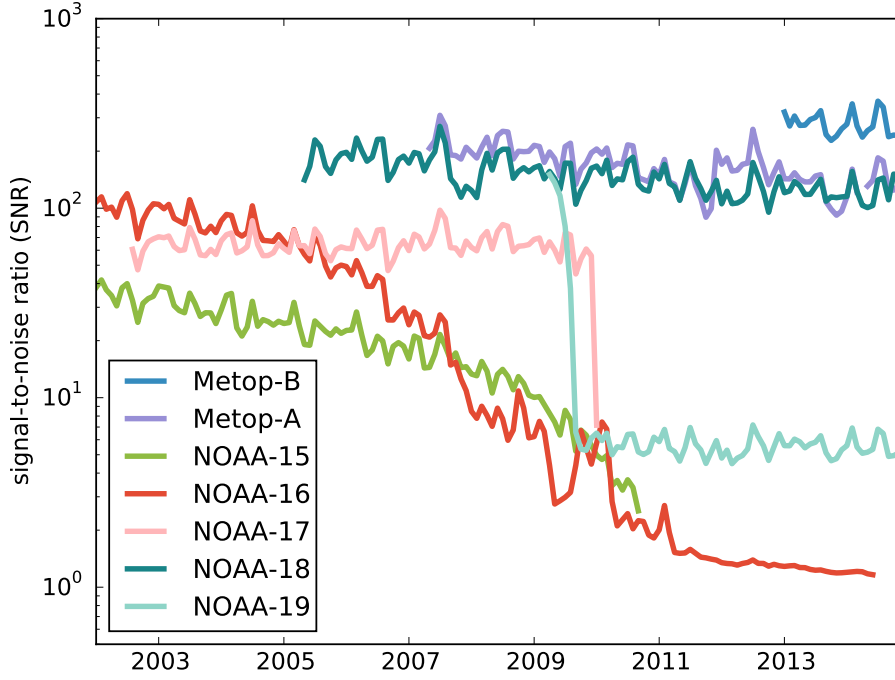


Figure A.4.: Temporal evolution of the signal-to-noise ratio (SNR) in the 183.3 ± 1 GHz channel for all used satellites in the period of study.

The idea behind the algorithm is that structures in an image are well visible in the Laplacian (L), which is commonly used for edge detection. On a discrete grid, two alternative operators are available for the estimation:

$$L_1 = \begin{bmatrix} 0 & 1 & 0 \\ 1 & -4 & 1 \\ 0 & 1 & 0 \end{bmatrix} \quad \text{and} \quad L_2 = \begin{bmatrix} 0.5 & 0 & 0.5 \\ 0 & -2 & 0 \\ 0.5 & 0 & 0.5 \end{bmatrix} \quad (\text{A.1})$$

Applying both to the image and subtracting the respective results cancels out the large structures with noise being retained. The operators L_1 and L_2 can be combined for computational efficiency to:

$$N = 2(L_2 - L_1) = \begin{bmatrix} 1 & -2 & 1 \\ -2 & 4 & -2 \\ 1 & -2 & 1 \end{bmatrix} \quad (\text{A.2})$$

This operator is applied to an image (I_{input}) with width W and height H in a two-dimensional linear convolution. Accordingly, the value of a pixel at the position $[x, y]$ in the resultant image is calculated by:

$$I_{result}[x, y] = \sum_{i=-1}^1 \sum_{j=-1}^1 I_{input}[x+i, y+j] \times N[i, j] \quad (\text{A.3})$$

$$\equiv I_{input}[x, y] * N \quad (\text{A.4})$$

where N is indexed from -1 to 1. The assumption of normal distributed noise with zero mean and variance σ^2 results in the computation of the

standard deviation of noise with derivation listed in [Immerkær \(1996\)](#):

$$\sigma_{noise} = \sqrt{\frac{\pi}{2}} \frac{1}{6(W-2)(H-2)} \sum_{x=2}^{W-1} \sum_{y=2}^{H-1} ||[x,y] * N| \quad (\text{A.5})$$

The outermost pixels in each direction are not taken into account for simplicity as not all direct neighbors are available.

The variance of noise calculated in this way was used to estimate the **Signal-to-Noise Ratio (SNR)**

$$SNR = \frac{\sigma_{image}^2}{\sigma_{noise}^2} \quad (\text{A.6})$$

for all satellite overpasses. In the calculation, pixels with $BT_{150/157 \text{ GHz}} \leq 240 \text{ K}$ were ignored to avoid small convective cells to be detected as noise, the 150/157 GHz channel is by itself never significantly affected by noise and therefore suitable for this mask.

Noise becomes visible by the naked eye for **SNR** values around 20 (Figs. [A.1b–d](#)), but suspicious positive **BTDs** are not yet visible at this level of noise (Figs. [A.1e–f](#)). **SNRs** around 10 make a more noisy impression, but convective cells are still well defined (Figs. [A.2b–d](#)). However, looking at **BTDs** between 183.3 ± 1 and 183.3 ± 3 GHz in this example (Fig. [A.2e](#)) shows a few pixels with positive values in presumably convection free areas in North Africa. The same is not yet visible in the differences between 183.3 ± 1 and 183.3 ± 7 GHz but irrespective of that, false detection of convection with this level of noise seems not unlikely. The examples are from the satellite NOAA-16; the quality of measurements from this satellite in the 183.3 GHz channels degraded further in the following years (Figs. [A.3](#) and [A.4](#)). Using this satellite would have resulted in unreliable convection screening and a positive trend in occurrence frequency of cold pools in the climatology due to an increasing number of false alarms over time.

Fig. [A.4](#) shows the temporal evolution of the **SNR** for all satellites during the period analyzed for the cold pool climatology. Considering only values above 20 to be unproblematic results in a significant reduction of available data. Unfortunately all AMSU-B instruments (NOAA-15–17) as well as the MHS instrument aboard NOAA-19 dropped below this value during the investigated period. Except for NOAA-19, all MHS instruments are almost free of noise ($SNR > 100$) with only marginal degradation over time. Convection screening based on the 183.3 GHz channels is accordingly a valid option for future studies.

References

- Agusti-Panareda, A., A. Beljaars, C. Cardinali, I. Genkova, and C. Thorncroft, 2010: Impacts of Assimilating AMMA Soundings on ECMWF Analyses and Forecasts. *Weather Forecast.*, **25** (4), 1142–1160, doi:10.1175/2010WAF2222370.1.
- Allen, C. J. T., R. Washington, and S. Engelstaedter, 2013: Dust emission and transport mechanisms in the central Sahara: Fennec ground-based observations from Bordj Badji Mokhtar, June 2011. *J. Geophys. Res. Atmos.*, **118** (12), 6212–6232, doi:10.1002/jgrd.50534.
- Allen, C. J. T., R. Washington, and A. Saci, 2015: Dust detection from ground-based observations in the summer global dust maximum: Results from Fennec 2011 and 2012 and implications for modeling and field observations. *J. Geophys. Res. Atmos.*, **120** (3), 897–916, doi:10.1002/2014JD022655.
- Ashpole, I., and R. Washington, 2013: A new high-resolution central and western Saharan summertime dust source map from automated satellite dust plume tracking. *J. Geophys. Res. Atmos.*, **118** (13), 6981–6995, doi:10.1002/jgrd.50554.
- Atkinson, N. C., 2001: Calibration, monitoring and validation of AMSU-B. *Adv. Sp. Res.*, **28** (1), 117–126, doi:10.1016/S0273-1177(01)00312-X.
- Bauer, P., E. Moreau, F. Chevallier, and U. O’Keeffe, 2006: Multiple-scattering microwave radiative transfer for data assimilation applications. *Q. J. R. Meteorol. Soc.*, **132** (617), 1259–1281, doi:10.1256/qj.05.153.
- Bennartz, R., and P. Bauer, 2003: Sensitivity of microwave radiances at 85-183 GHz to precipitating ice particles. *Radio Sci.*, **38** (4), doi:10.1029/2002RS002626.
- Birch, C. E., D. J. Parker, J. H. Marsham, D. Copley, and L. Garcia-Carreras, 2014: A seamless assessment of the role of convection in the water cycle of the West African Monsoon. *J. Geophys. Res. Atmos.*, **119** (6), 2890–2912, doi:10.1002/2013JD020887.
- Birch, C. E., D. J. Parker, J. H. Marsham, and G. M. Devine, 2012: The effect of orography and surface albedo on stratification in the summertime Saharan boundary layer: Dynamics and implications for dust transport. *J. Geophys. Res.*, **117** (D5), D05 105, doi:10.1029/2011JD015965.
- Black, T. L., 1994: The New NMC Mesoscale Eta Model: Description and Forecast Examples. *Weather Forecast.*, **9** (2), 265–278, doi:10.1175/1520-0434(1994)009<0265:TNNMEM>2.0.CO;2.
- Booth, B. B. B., N. J. Dunstone, P. R. Halloran, T. Andrews, and N. Bellouin, 2012: Aerosols implicated as a prime driver of twentieth-century North Atlantic climate variability. *Nature*, **484** (7393), 228–232, doi:10.1038/nature10946.
- Bou Karam, D., E. Williams, M. Janiga, C. Flamant, M. McGraw-Herdeg, J. Cuesta, A. Auby, and C. Thorncroft, 2014: Synoptic-scale dust emissions over the Sahara Desert initiated by a moist convective cold pool in early August 2006. *Q. J. R. Meteorol. Soc.*, **140** (685), 2591–2607, doi:10.1002/qj.2326.
- Brindley, H., P. Knippertz, C. Ryder, and I. Ashpole, 2012: A critical evaluation of the ability of the Spinning Enhanced Visible and Infrared Imager (SEVIRI) thermal infrared red-green-blue rendering to identify dust events: Theoretical analysis. *J. Geophys. Res.*, **117** (D7), D07 201, doi:10.1029/2011JD017326.
- Buehler, S. A., P. Eriksson, T. Kuhn, A. von Engeln, and C. Verdes, 2005a: ARTS, the atmospheric radiative transfer simulator. *J. Quant. Spectrosc. Radiat. Transf.*, **91** (1), 65–93, doi:10.1016/j.jqsrt.2004.05.051.
- Buehler, S. A., M. Kuvatov, and V. O. John, 2005b: Scan asymmetries in AMSU-B data. *Geophys. Res. Lett.*, **32** (24), 1–4, doi:10.1029/2005GL024747.
- Burns, B., X. Wu, and G. Diak, 1997: Effects of precipitation and cloud ice on brightness temperatures in AMSU moisture channels. *IEEE Trans. Geosci. Remote Sens.*, **35** (6), 1429–1437, doi:10.1109/36.649797.

- Chauvin, F., R. Roehrig, and J.-P. Lafore, 2010: Intraseasonal Variability of the Saharan Heat Low and Its Link with Midlatitudes. *J. Clim.*, **23** (10), 2544–2561, doi:10.1175/2010JCLI3093.1.
- Chen, W., and D. W. Fryrear, 2002: Sedimentary characteristics of a haboob dust storm. *Atmos. Res.*, **61** (1), 75–85, doi:10.1016/S0169-8095(01)00092-8.
- Chomette, O., M. Legrand, and B. Marticorena, 1999: Determination of the wind speed threshold for the emission of desert dust using satellite remote sensing in the thermal infrared. *J. Geophys. Res.*, **104**, 31 207, doi:10.1029/1999JD900756.
- Christensen, J., and Coauthors, 2013: Climate Phenomena and their Relevance for Future Regional Climate Change. *Climate Change 2013: The Physical Science Basis. Contribution of Working Group I to the Fifth Assessment Report of the Intergovernmental Panel on Climate Change*, T. Stocker, D. Qin, G.-K. Plattner, M. Tignor, S. Allen, J. Boschung, A. Nauels, Y. Xia, V. Bex, and P. Midgley, Eds., Cambridge University Press, Cambridge, United Kingdom and New York, NY, USA.
- Cohen, A. E., M. C. Coniglio, S. F. Corfidi, and S. J. Corfidi, 2007: Discrimination of Mesoscale Convective System Environments Using Sounding Observations. *Weather Forecast.*, **22** (5), 1045–1062, doi:10.1175/WAF1040.1.
- Coniglio, M. C., D. J. Stensrud, and L. J. Wicker, 2006: Effects of Upper-Level Shear on the Structure and Maintenance of Strong Quasi-Linear Mesoscale Convective Systems. *J. Atmos. Sci.*, **63** (4), 1231–1252, doi:10.1175/JAS3681.1.
- Cook, K. H., and E. K. Vizy, 2015: Detection and Analysis of an Amplified Warming of the Sahara Desert. *J. Clim.*, **28** (16), 6560–6580, doi:10.1175/JCLI-D-14-00230.1.
- Corfidi, S. F., 2003: Cold Pools and MCS Propagation: Forecasting the Motion of Downwind-Developing MCSs. *Weather Forecast.*, **18** (6), 997–1017, doi:10.1175/1520-0434(2003)018<0997:CPAMPF>2.0.CO;2.
- Couvreux, F., F. Guichard, O. Bock, B. Campistron, J.-P. Lafore, and J.-L. Redelsperger, 2010: Synoptic variability of the monsoon flux over West Africa prior to the onset. *Q. J. R. Meteorol. Soc.*, **136** (S1), 159–173, doi:10.1002/qj.473.
- Cowie, S. M., J. H. Marsham, and P. Knippertz, 2015: The importance of rare, high-wind events for dust uplift in northern Africa. *Geophys. Res. Lett.*, doi:10.1002/2015GL065819.
- Cuesta, J., J. H. Marsham, D. J. Parker, and C. Flamant, 2009: Dynamical mechanisms controlling the vertical redistribution of dust and the thermodynamic structure of the West Saharan atmospheric boundary layer during summer. *Atmos. Sci. Lett.*, **10** (1), 34–42, doi:10.1002/asl.207.
- Dee, D. P., and Coauthors, 2011: The ERA-Interim reanalysis: configuration and performance of the data assimilation system. *Q. J. R. Meteorol. Soc.*, **137** (656), 553–597, doi:10.1002/qj.828.
- Dong, B., and R. Sutton, 2015: Dominant role of greenhouse-gas forcing in the recovery of Sahel rainfall. *Nat. Clim. Chang.*, **5** (August), 1–9, doi:10.1038/nclimate2664.
- Druryan, L. M., 2011: Studies of 21st-century precipitation trends over West Africa. *Int. J. Climatol.*, **31** (10), 1415–1424, doi:10.1002/joc.2180.
- Emanuel, K. A., 1994: *Atmospheric Convection*. Oxford University Press, New York, 508 pp.
- Emmel, C., P. Knippertz, and O. Schulz, 2010: Climatology of convective density currents in the southern foothills of the Atlas Mountains. *J. Geophys. Res.*, **115** (D11), D11 115, doi:10.1029/2009JD012863.
- Engelstaedter, S., and R. Washington, 2008: Atmospheric controls on the annual cycle of North African dust. *J. Geophys. Res. Atmos.*, **113** (D23), doi:10.1029/2008JD010275.
- Engelstaedter, S., R. Washington, C. Flamant, D. J. Parker, C. J. T. Allen, and M. C. Todd, 2015: The Saharan heat low and moisture transport pathways in the central Sahara-Multi-aircraft observations and Africa-LAM evaluation. *J. Geophys. Res. Atmos.*, **120** (10), 4417–4442, doi:10.1002/2015JD023123.
- Engerer, N. A., D. J. Stensrud, and M. C. Coniglio, 2008: Surface Characteristics of Observed Cold Pools. *Mon. Weather Rev.*, **136** (12), 4839–4849, doi:10.1175/2008MWR2528.1.
- Evan, A. T., C. Flamant, S. Fiedler, and O. Doherty, 2014: An analysis of aeolian dust in climate models. *Geophys. Res. Lett.*, **41**, 5996–6001, doi:10.1002/2014GL060545.
- Evan, A. T., C. Flamant, C. Lavaysse, C. Kocha, and A. Saci, 2015: Water Vapor-Forced Greenhouse Warming over the Sahara Desert and the Recent Recovery from the Sahelian Drought. *J. Clim.*, **28** (1), 108–123, doi:10.1175/JCLI-D-14-00039.1.

- Evan, A. T., D. J. Vimont, A. K. Heidinger, J. P. Kossin, and R. Bennartz, 2009: The Role of Aerosols in the Evolution of Tropical North Atlantic Ocean Temperature Anomalies. *Science*, **324** (5928), 778–781, doi:10.1126/science.1167404.
- Eymard, L., F. Karbou, S. Janicot, N. Chouaib, and F. Pinsard, 2010: On the use of Advanced Microwave Sounding Unit-A and -B measurements for studying the monsoon variability over West Africa. *J. Geophys. Res.*, **115** (D20), D20 115, doi:10.1029/2009JD012935.
- Farquharson, J. S., 1937: Haboobs and instability in the sudan. *Q. J. R. Meteorol. Soc.*, **63** (271), 393–414, doi:10.1002/qj.49706327111.
- Fiedler, S., M. L. Kaplan, and P. Knippertz, 2015: The importance of Harmattan surges for the emission of North African dust aerosol. *Geophys. Res. Lett.*, doi:10.1002/2015GL065925.
- Fiedler, S., K. Schepanski, B. Heinold, P. Knippertz, and I. Tegen, 2013: Climatology of nocturnal low-level jets over North Africa and implications for modeling mineral dust emission. *J. Geophys. Res. Atmos.*, **118** (12), 6100–6121, doi:10.1002/jgrd.50394.
- Fink, A. H., and A. Reiner, 2003: Spatiotemporal variability of the relation between African Easterly Waves and West African Squall Lines in 1998 and 1999. *J. Geophys. Res.*, **108** (D11), 4332, doi:10.1029/2002JD002816.
- Fink, A. H., D. G. Vincent, and V. Ermert, 2006: Rainfall Types in the West African Sudanian Zone during the Summer Monsoon 2002. *Mon. Weather Rev.*, **134** (8), 2143–2164, doi:10.1175/MWR3182.1.
- Fink, A. H., and Coauthors, 2011: Operational meteorology in West Africa: observational networks, weather analysis and forecasting. *Atmos. Sci. Lett.*, **12** (1), 135–141, doi:10.1002/as1.324.
- Fink, A. H., T. Engel, V. Ermert, R. van der Linden, M. Schneidewind, R. Redl, E. Afiesimama, W. Thiaw, C. Yorke, and M. Evans, 2016: Mean climate and seasonal cycle. *Meteorology of Tropical West Africa: The Forecasters' Handbook*, D. J. Parker, and M. Diop-Kane, Eds., Wiley, Chichester, UK, in press.
- Fitzpatrick, R. G. J., C. L. Bain, P. Knippertz, J. H. Marsham, and D. J. Parker, 2015: The West African Monsoon Onset: A Concise Comparison of Definitions. *J. Clim.*, **28** (22), 8673–8694, doi:10.1175/JCLI-D-15-0265.1.
- Flamant, C., J.-P. Chaboureaud, D. J. Parker, C. M. Taylor, J.-P. Cammas, O. Bock, F. Timouk, and J. Pelon, 2007: Airborne observations of the impact of a convective system on the planetary boundary layer thermodynamics and aerosol distribution in the inter-tropical discontinuity region of the West African Monsoon. *Q. J. R. Meteorol. Soc.*, **133** (626), 1175–1189, doi:10.1002/qj.97.
- García-Carreras, L., and Coauthors, 2013: The impact of convective cold pool outflows on model biases in the Sahara. *Geophys. Res. Lett.*, **40** (8), 1647–1652, doi:10.1002/grl.50239.
- García-Carreras, L., and Coauthors, 2015: The Turbulent Structure and Diurnal Growth of the Saharan Atmospheric Boundary Layer. *J. Atmos. Sci.*, **72** (2), 693–713, doi:10.1175/JAS-D-13-0384.1.
- García-Serrano, J., F. J. Doblas-Reyes, R. J. Haarsma, and I. Polo, 2013: Decadal prediction of the dominant West African monsoon rainfall modes. *J. Geophys. Res. Atmos.*, **118** (11), 5260–5279, doi:10.1002/jgrd.50465.
- Goff, R. C., 1976: Vertical Structure of Thunderstorm Outflows. *Mon. Weather Rev.*, **104** (11), 1429–1440, doi:10.1175/1520-0493(1976)104<1429:VSOT0>2.O.CO;2.
- Goldberg, M. D., D. S. Crosby, and L. Zhou, 2001: The Limb Adjustment of AMSU-A Observations: Methodology and Validation. *J. Appl. Meteorol.*, **40** (1), 70–83, doi:10.1175/1520-0450(2001)040<0070:TLA0AA>2.O.CO;2.
- Grams, C. M., S. C. Jones, J. H. Marsham, D. J. Parker, J. M. Haywood, and V. Heuveline, 2010: The Atlantic inflow to the Saharan heat low: observations and modelling. *Q. J. R. Meteorol. Soc.*, **136** (S1), 125–140, doi:10.1002/qj.429.
- Grandpeix, J.-Y., and J.-P. Lafore, 2010: A Density Current Parameterization Coupled with Emanuel's Convection Scheme. Part I: The Models. *J. Atmos. Sci.*, **67** (4), 881–897, doi:10.1175/2009JAS3044.1.
- Gregory, D., J.-J. Morcrette, C. Jakob, A. C. M. Beljaars, and T. Stockdale, 2000: Revision of convection, radiation and cloud schemes in the ECMWF integrated forecasting system. *Q. J. R. Meteorol. Soc.*, **126** (566), 1685–1710, doi:10.1002/qj.49712656607.

- Grell, G. A., J. Dudhia, and D. R. Stauffer, 1995: A Description of the Fifth-Generation Penn State/NCAR Mesoscale Model (MM5). *NCAR Tech. Note*, NCAR/TN-398+STR.
- Guichard, F., L. Kergoat, E. Mougou, F. Timouk, F. Baup, P. Hiernaux, and F. Lavenu, 2009: Surface thermodynamics and radiative budget in the Sahelian Gourma: Seasonal and diurnal cycles. *J. Hydrol.*, **375** (1-2), 161–177, doi:10.1016/j.jhydrol.2008.09.007.
- Hallworth, M. A., H. E. Huppert, and M. Ungarish, 2001: Axisymmetric gravity currents in a rotating system: Experimental and numerical investigations. *J. Fluid Mech.*, **447**, 1–29, doi:10.1017/S0022112001005523.
- Heinold, B., P. Knippertz, J. H. Marsham, S. Fiedler, N. S. Dixon, K. Schepanski, B. Laurent, and I. Tegen, 2013: The role of deep convection and nocturnal low-level jets for dust emission in summertime West Africa: Estimates from convection-permitting simulations. *J. Geophys. Res. Atmos.*, **118** (10), 4385–4400, doi:10.1002/jgrd.50402.
- Hobby, M., and Coauthors, 2013: The Fennec Automatic Weather Station (AWS) Network: Monitoring the Saharan Climate System. *J. Atmos. Ocean. Technol.*, **30** (4), 709–724, doi:10.1175/JTECH-D-12-00037.1.
- Hong, G., 2005: Detection of tropical deep convective clouds from AMSU-B water vapor channels measurements. *J. Geophys. Res.*, **110** (D5), D05 205, doi:10.1029/2004JD004949.
- Hourdin, F., and Coauthors, 2010: AMMA-Model Intercomparison Project. *Bull. Am. Meteorol. Soc.*, **91** (1), 95–104, doi:10.1175/2009BAMS2791.1.
- Immerkær, J., 1996: Fast Noise Variance Estimation. *Comput. Vis. Image Underst.*, **64** (2), 300–302, doi:10.1006/cviu.1996.0060.
- Janicot, S., F. Kamga, J.-P. Lafore, M. Biasutti, P. Knippertz, C. M. Taylor, and C. Thorncroft, 2015: Key research and prediction challenges for West and Central Africa. *CLIVAR Exch.*, **19** (66), 10–15.
- Janjić, Z. I., R. Gall, and M. E. Pyle, 2010: Scientific Documentation for the NMM Solver. *NCAR Tech. Note*, NCAR/TN-477+STR, doi:10.5065/D6MW2F3Z.
- Jones, C., F. Giorgi, and G. Asrar, 2011: The Coordinated Regional Downscaling Experiment: CORDEX; An international downscaling link to CMIP5. *CLIVAR Exch.*, **16** (56), 34–40.
- Kadow, C., S. Illing, O. Kunst, and U. Cubasch, 2014: A Hybrid Evaluation System Framework (Shell & Web) with Standardized Access to Climate Model Data and Verification Tools for a Clear Climate Science Infrastructure on Big Data High Performance Computers. *AGU Fall Meet.*, San Francisco, URL <https://agu.confex.com/agu/fm14/meetingapp.cgi/Paper/30238>.
- Klein, C., D. Heinzeller, J. Bliefernicht, and H. Kunstmann, 2015: Variability of West African monsoon patterns generated by a WRF multi-physics ensemble. *Clim. Dyn.*, doi:10.1007/s00382-015-2505-5.
- Knippertz, P., 2003: Tropical-Extratropical Interactions Causing Precipitation in Northwest Africa: Statistical Analysis and Seasonal Variations. *Mon. Weather Rev.*, **131** (12), 3069–3076, doi:10.1175/1520-0493(2003)131<3069:TICPIN>2.0.CO;2.
- Knippertz, P., 2008: Dust emissions in the West African heat trough – the role of the diurnal cycle and of extratropical disturbances. *Meteorol. Zeitschrift*, **17** (5), 553–563, doi:10.1127/0941-2948/2008/0315.
- Knippertz, P., C. Deutscher, K. Kandler, T. Müller, O. Schulz, and L. Schütz, 2007: Dust mobilization due to density currents in the Atlas region: Observations from the Saharan Mineral Dust Experiment 2006 field campaign. *J. Geophys. Res.*, **112** (D21), D21 109, doi:10.1029/2007JD008774.
- Knippertz, P., and A. H. Fink, 2008: Dry-Season Precipitation in Tropical West Africa and Its Relation to Forcing from the Extratropics. *Mon. Weather Rev.*, **136** (9), 3579–3596, doi:10.1175/2008MWR2295.1.
- Knippertz, P., and A. H. Fink, 2009: Prediction of Dry-Season Precipitation in Tropical West Africa and Its Relation to Forcing from the Extratropics. *Weather Forecast.*, **24** (4), 1064–1084, doi:10.1175/2009WAF2222221.1.
- Knippertz, P., A. H. Fink, A. Reiner, and P. Speth, 2003: Three Late Summer/Early Autumn Cases of Tropical-Extratropical Interactions Causing Precipitation in Northwest Africa. *Mon. Weather Rev.*, **131** (1), 116–135, doi:10.1175/1520-0493(2003)131<0116:TLSEAC>2.0.CO;2.

- Knippertz, P., and M. C. Todd, 2010: The central west Saharan dust hot spot and its relation to African easterly waves and extratropical disturbances. *J. Geophys. Res.*, **115** (D12), D12 117, doi:10.1029/2009JD012819.
- Knippertz, P., J. Trentmann, and A. Seifert, 2009a: High-resolution simulations of convective cold pools over the northwestern Sahara. *J. Geophys. Res.*, **114** (D8), D08 110, doi:10.1029/2008JD011271.
- Knippertz, P., and Coauthors, 2009b: Dust mobilization and transport in the northern Sahara during SAMUM 2006 - a meteorological overview. *Tellus B*, **61** (1), 12–31, doi:10.1111/j.1600-0889.2008.00380.x.
- Kocha, C., P. Tulet, J. P. Lafore, and C. Flamant, 2013: The importance of the diurnal cycle of Aerosol Optical Depth in West Africa. *Geophys. Res. Lett.*, **40** (4), 785–790, doi:10.1002/grl.50143.
- Labrot, T., L. Lavanant, K. Whyte, N. Atkinson, and P. Brunel, 2011: AAPP documentation scientific description, NWPSAF-MF-UD-001. Tech. rep., NWP SAF Satellite Application Facility for Numerical Weather Prediction. URL http://nwpsaf.eu/deliverables/aapp/NWPSAF-MF-UD-001_Science.pdf.
- Lafore, J.-P., and Coauthors, 2011: Progress in understanding of weather systems in West Africa. *Atmos. Sci. Lett.*, **12** (1), 7–12, doi:10.1002/asl.335.
- Lafore, J. P., and Coauthors, 2016: Deep convection. *Meteorology of Tropical West Africa: The Forecasters' Handbook*, D. J. Parker, and M. Diop-Kane, Eds., Wiley, Chichester, UK, in press.
- Lavaysse, C., 2015: Warming trends: Saharan desert warming. *Nat. Clim. Chang.*, **5** (9), 807–808, doi:10.1038/nclimate2773.
- Lavaysse, C., A. Diedhiou, H. Laurent, and T. Lebel, 2006: African Easterly Waves and convective activity in wet and dry sequences of the West African Monsoon. *Clim. Dyn.*, **27** (2-3), 319–332, doi:10.1007/s00382-006-0137-5.
- Lavaysse, C., C. Flamant, S. Janicot, and P. Knippertz, 2010: Links between African easterly waves, midlatitude circulation and intraseasonal pulsations of the West African heat low. *Q. J. R. Meteorol. Soc.*, **136** (S1), 141–158, doi:10.1002/qj.555.
- Lavaysse, C., C. Flamant, S. Janicot, D. J. Parker, J.-P. Lafore, B. Sultan, and J. Pelon, 2009: Seasonal evolution of the West African heat low: a climatological perspective. *Clim. Dyn.*, **33** (2-3), 313–330, doi:10.1007/s00382-009-0553-4.
- Lensky, I. M., and D. Rosenfeld, 2008: Clouds-Aerosols-Precipitation Satellite Analysis Tool (CAPSAT). *Atmos. Chem. Phys.*, **8** (22), 6739–6753, doi:10.5194/acp-8-6739-2008.
- Linden, P. F., and J. E. Simpson, 1985: Microbursts: a hazard for aircraft. *Nature*, **317** (6038), 601–602, doi:10.1038/317601a0.
- Mailier, P. J., D. B. Stephenson, C. A. T. Ferro, and K. I. Hodges, 2006: Serial Clustering of Extratropical Cyclones. *Mon. Weather Rev.*, **134** (8), 2224–2240, doi:10.1175/MWR3160.1.
- Marsham, J. H., N. S. Dixon, L. Garcia-Carreras, G. M. S. Lister, D. J. Parker, P. Knippertz, and C. E. Birch, 2013a: The role of moist convection in the West African monsoon system: Insights from continental-scale convection-permitting simulations. *Geophys. Res. Lett.*, **40** (9), 1843–1849, doi:10.1002/grl.50347.
- Marsham, J. H., P. Knippertz, N. S. Dixon, D. J. Parker, and G. M. S. Lister, 2011: The importance of the representation of deep convection for modeled dust-generating winds over West Africa during summer. *Geophys. Res. Lett.*, **38**, 2–7, doi:10.1029/2011GL048368.
- Marsham, J. H., D. J. Parker, C. M. Grams, C. M. Taylor, and J. M. Haywood, 2008: Uplift of Saharan dust south of the intertropical discontinuity. *J. Geophys. Res. Atmos.*, **113** (21), 1–14, doi:10.1029/2008JD009844.
- Marsham, J. H., D. J. Parker, M. C. Todd, J. R. Banks, H. E. Brindley, L. Garcia-Carreras, a. J. Roberts, and C. L. Ryder, 2015: The contrasting roles of water and dust in controlling daily variations in radiative heating of the summertime Saharan Heat Low. *Atmos. Chem. Phys. Discuss.*, **15** (14), 19 447–19 476, doi:10.5194/acpd-15-19447-2015.
- Marsham, J. H., and Coauthors, 2013b: Meteorology and dust in the central Sahara: Observations from Fennec supersite-1 during the June 2011 Intensive Observation Period. *J. Geophys. Res. Atmos.*, **118** (10), 4069–4089, doi:10.1002/jgrd.50211.
- Marticorena, B., and G. Bergametti, 1995: Modeling the atmospheric dust cycle: 1. Design of a soil-derived dust emission scheme. *J. Geophys. Res.*, **100** (D8), 16 415, doi:10.1029/95JD00690.

- Martin, E. R., C. Thorncroft, and B. B. Booth, 2014: The multidecadal atlantic SST-sahel rainfall teleconnection in CMIP5 simulations. *J. Clim.*, **27** (2), 784–806, doi: [10.1175/JCLI-D-13-00242.1](https://doi.org/10.1175/JCLI-D-13-00242.1).
- Mathon, V., H. Laurent, and T. Lebel, 2002: Mesoscale Convective System Rainfall in the Sahel. *J. Appl. Meteorol.*, **41** (11), 1081–1092, doi: [10.1175/1520-0450\(2002\)041<1081:MCSRIT>2.0.CO;2](https://doi.org/10.1175/1520-0450(2002)041<1081:MCSRIT>2.0.CO;2).
- Miller, S. D., A. P. Kuciauskas, M. Liu, Q. Ji, J. S. Reid, D. W. Breed, A. L. Walker, and A. A. Mandoos, 2008: Haboob dust storms of the southern Arabian Peninsula. *J. Geophys. Res. Atmos.*, **113** (1), 1–26, doi: [10.1029/2007JD008550](https://doi.org/10.1029/2007JD008550).
- Narendra Babu, A., J. B. Nee, and K. K. Kumar, 2010: Seasonal and diurnal variation of convective available potential energy (CAPE) using COSMIC/FORMOSAT-3 observations over the tropics. *J. Geophys. Res.*, **115** (D4), D04 102, doi: [10.1029/2009JD012535](https://doi.org/10.1029/2009JD012535).
- Offer, Z. Y., and D. Goossens, 2001: Ten years of aeolian dust dynamics in a desert region (Negev desert, Israel): analysis of airborne dust concentration, dust accumulation and the high-magnitude dust events. *J. Arid Environ.*, **47** (2), 211–249, doi: [10.1006/jare.2000.0706](https://doi.org/10.1006/jare.2000.0706).
- Pantillon, F., P. Knippertz, J. Marsham, and C. Birch, 2015: A parameterization of convective dust storms for models with mass-flux convection schemes. *J. Atmos. Sci.*, 150407121742006, doi: [10.1175/JAS-D-14-0341.1](https://doi.org/10.1175/JAS-D-14-0341.1).
- Parker, D. J., and Coauthors, 2005: The diurnal cycle of the West African monsoon circulation. *Q. J. R. Meteorol. Soc.*, **131** (611), 2839–2860, doi: [10.1256/qj.04.52](https://doi.org/10.1256/qj.04.52).
- Parker, D. J., and Coauthors, 2008: The Amma Radiosonde Program and its Implications for the Future of Atmospheric Monitoring Over Africa. *Bull. Am. Meteorol. Soc.*, **89** (7), 1015–1027, doi: [10.1175/2008BAMS2436.1](https://doi.org/10.1175/2008BAMS2436.1).
- Pohlmann, H., and Coauthors, 2013: Improved forecast skill in the tropics in the new MiKlip decadal climate predictions. *Geophys. Res. Lett.*, **40** (21), 5798–5802, doi: [10.1002/2013GL058051](https://doi.org/10.1002/2013GL058051).
- Prospero, J. M., 2002: Environmental characterization of global sources of atmospheric soil dust identified with the NIMBUS 7 Total Ozone Mapping Spectrometer (TOMS) absorbing aerosol product. *Rev. Geophys.*, **40** (1), 1002, doi: [10.1029/2000RG000095](https://doi.org/10.1029/2000RG000095).
- Provod, M., J. H. Marsham, D. J. Parker, and C. E. Birch, 2015: A characterization of cold pools in the West African Sahel. *Mon. Weather Rev.*, doi: [10.1175/MWR-D-15-0023.1](https://doi.org/10.1175/MWR-D-15-0023.1).
- Rácz, Z., and R. K. Smith, 1999: The dynamics of heat lows. *Q. J. R. Meteorol. Soc.*, **125** (553), 225–252, doi: [10.1002/qj.49712555313](https://doi.org/10.1002/qj.49712555313).
- Raman, A., A. F. Arellano, and J. J. Brost, 2014: Revisiting haboobs in the southwestern United States: An observational case study of the 5 July 2011 Phoenix dust storm. *Atmos. Environ.*, **89**, 179–188, doi: [10.1016/j.atmosenv.2014.02.026](https://doi.org/10.1016/j.atmosenv.2014.02.026).
- Redelsperger, J.-L., C. D. Thorncroft, A. Diedhiou, T. Lebel, D. J. Parker, and J. Polcher, 2006: African Monsoon Multidisciplinary Analysis: An International Research Project and Field Campaign. *Bull. Am. Meteorol. Soc.*, **87** (12), 1739–1746, doi: [10.1175/BAMS-87-12-1739](https://doi.org/10.1175/BAMS-87-12-1739).
- Redl, R., A. H. Fink, and P. Knippertz, 2015: An Objective Detection Method for Convective Cold Pool Events and Its Application to Northern Africa. *Mon. Weather Rev.*, **143** (12), 5055–5072, ©American Meteorological Society. Used with permission. doi: [10.1175/MWR-D-15-0223.1](https://doi.org/10.1175/MWR-D-15-0223.1).
- Redl, R., P. Knippertz, and A. H. Fink, 2016: Weakening and Moistening of the Summertime Saharan Heat Low through Convective Cold Pools from the Atlas Mountains. *J. Geophys. Res. Atmos.*, **121**, ©American Geophysical Union. Used with permission. doi: [10.1002/2015JD024443](https://doi.org/10.1002/2015JD024443).
- Reinfried, F., I. Tegen, B. Heinold, O. Hellmuth, K. Schepanski, U. Cubasch, H. Huebener, and P. Knippertz, 2009: Simulations of convectively-driven density currents in the Atlas region using a regional model: Impacts on dust emission and sensitivity to horizontal resolution and convection schemes. *J. Geophys. Res.*, **114** (D8), D08 127, doi: [10.1029/2008JD010844](https://doi.org/10.1029/2008JD010844).
- Riehl, H., and J. S. Malkus, 1958: On the Heat Balance in the Equatorial Trough Zone. *Geophysica*, **6**.
- Riemann-Campe, K., K. Fraedrich, and F. Lunkeit, 2009: Global climatology of Convective Available Potential Energy (CAPE) and Convective Inhibition (CIN) in ERA-40 reanalysis. *Atmos. Res.*, **93** (1–3), 534–545, doi: [10.1016/j.atmosres.2008.09.037](https://doi.org/10.1016/j.atmosres.2008.09.037).

- Rivera Rivera, N. I., T. E. Gill, M. P. Bleiweiss, and J. L. Hand, 2010: Source characteristics of hazardous Chihuahuan Desert dust outbreaks. *Atmos. Environ.*, **44** (20), 2457–2468, doi:10.1016/j.atmosenv.2010.03.019.
- Roberts, A. J., and P. Knippertz, 2014: The formation of a large summertime Saharan dust plume: Convective and synoptic-scale analysis. *J. Geophys. Res. Atmos.*, **119** (4), 1766–1785, doi:10.1002/2013JD020667.
- Roberts, A. J., J. H. Marsham, and P. Knippertz, 2014: Disagreements in Low-level Moisture between (Re)Analyses over Summertime West Africa. *Mon. Weather Rev.*, 141006071214009, doi:10.1175/MWR-D-14-00218.1.
- Rodríguez-Fonseca, B., and Coauthors, 2011: Interannual and decadal SST-forced responses of the West African monsoon. *Atmos. Sci. Lett.*, **12** (1), 67–74, doi:10.1002/asl.308.
- Roehrig, R., F. Chauvin, and J.-P. Lafore, 2011: 10–25-Day Intraseasonal Variability of Convection over the Sahel: A Role of the Saharan Heat Low and Midlatitudes. *J. Clim.*, **24** (22), 5863–5878, doi:10.1175/2011JCLI3960.1.
- Ryder, C. L., and Coauthors, 2013: Optical properties of Saharan dust aerosol and contribution from the coarse mode as measured during the Fennec 2011 aircraft campaign. *Atmos. Chem. Phys.*, **13** (1), 303–325, doi:10.5194/acp-13-303-2013.
- Sanogo, S., A. H. Fink, J. A. Omotosho, A. Ba, R. Redl, and V. Ermert, 2015: Spatio-temporal characteristics of the recent rainfall recovery in West Africa. *Int. J. Climatol.*, **35**, 4589–4605, doi:10.1002/joc.4309.
- Schmetz, J., P. Pili, S. Tjemkes, D. Just, J. Kerkmann, S. Rota, and A. Ratier, 2002: An Introduction to Meteosat Second Generation (MSG). *Bull. Am. Meteorol. Soc.*, **83** (7), 977–992, doi:10.1175/1520-0477(2002)083<0977:AITMSG>2.3.CO;2.
- Schulz, O., 2008: The IMPETUS Climate Monitoring Network. *IMPETUS Atlas Morocco*, O. Schulz, and M. Judex, Eds., 3rd ed., Department of Geography, University of Bonn, Bonn, chap. 7, 17–8.
- Schuster, R., A. H. Fink, and P. Knippertz, 2013: Formation and Maintenance of Nocturnal Low-Level Stratus over the Southern West African Monsoon Region during AMMA 2006. *J. Atmos. Sci.*, **70** (8), 2337–2355, doi:10.1175/JAS-D-12-0241.1.
- Simpson, J. E., 1987: *Gravity Currents: in the Environment and the Laboratory*. Ellis Horwood Limited, 244 pp.
- Skamarock, W. C., and Coauthors, 2008: A Description of the Advanced Research WRF Version 3. *NCAR Tech. Note*, NCAR/TN-475+STR, doi:10.5065/D68S4MVH.
- Smith, A., N. Lott, and R. Vose, 2011: The Integrated Surface Database: Recent Developments and Partnerships. *Bull. Am. Meteorol. Soc.*, **92** (6), 704–708, doi:10.1175/2011BAMS3015.1.
- Speth, P., M. Christoph, and B. Diekkrüger, Eds., 2010: *Impacts of Global Change on the Hydrological Cycle in West and Northwest Africa*. Springer Berlin Heidelberg, Berlin, Heidelberg, doi:10.1007/978-3-642-12957-5.
- Stein, T. H., D. J. Parker, R. J. Hogan, C. Birch, C. E. Holloway, G. Lister, J. H. Marsham, and S. J. Woolnough, 2015: The representation of the West-African Monsoon vertical cloud structure in the Met Office Unified Model: An evaluation with CloudSat. *Q. J. R. Meteorol. Soc.*, n/a–n/a, doi:10.1002/qj.2614.
- Strong, C. L., K. Parsons, G. H. McTainsh, and a. Sheehan, 2011: Dust transporting wind systems in the lower Lake Eyre Basin, Australia: A preliminary study. *Aeolian Res.*, **2** (4), 205–214, doi:10.1016/j.aeolia.2010.11.001.
- Sultan, B., and S. Janicot, 2003: The West African Monsoon Dynamics. Part II: The “Preonset” and “Onset” of the Summer Monsoon. *J. Clim.*, **16** (21), 3407–3427, doi:10.1175/1520-0442(2003)016<3407:TWAMDP>2.0.CO;2.
- Sun, J., S. Burns, and D. Lenschow, 2002: Intermittent turbulence associated with a density current passage in the stable boundary layer. *Boundary-Layer Meteorol.*, **105** (2), 199–219, doi:10.1023/A:1019969131774.
- Sutton, L. J., 1925: Haboobs. *Q. J. R. Meteorol. Soc.*, **51** (213), 25–30, doi:10.1002/qj.49705723906.
- Takemi, T., 2005: Explicit Simulations of Convective-Scale Transport of Mineral Dust in Severe Convective Weather. *J. Meteorol. Soc. Japan*, **83A**, 187–203, doi:10.2151/jmsj.83A.187.

- Thorncroft, C. D., and M. Blackburn, 1999: Maintenance of the African easterly jet. *Q. J. R. Meteorol. Soc.*, **125** (555), 763–786, doi:10.1002/qj.49712555502.
- Todd, M. C., and Coauthors, 2013: Meteorological and dust aerosol conditions over the western Saharan region observed at Fennec Supersite-2 during the intensive observation period in June 2011. *J. Geophys. Res. Atmos.*, **118** (15), 8426–8447, doi:10.1002/jgrd.50470.
- Vizy, E. K., and K. H. Cook, 2009: A mechanism for African monsoon breaks: Mediterranean cold air surges. *J. Geophys. Res.*, **114** (D1), D01 104, doi:10.1029/2008JD010654.
- Wang, W., and Coauthors, 2013: *WRF-ARW Version 3.5 Modeling System User's Guide*. 411 pp.
- Wark, D. Q., R. H. Brown, D. H. Josephson, and G. W. Withee, 1993: Adjustment of TIROS Operational Vertical Sounder Data to a Vertical View, Technical Report NESDIS 64. Tech. rep., NOAA, 36 pp.
- Washington, R., and Coauthors, 2012: Fennec – The Saharan Climate System. *CLIVAR Exch.*, **17** (60), 31–33, URL <http://www.clivar.org/node/240>.
- Weisman, M. L., and R. Rotunno, 2004: "A Theory for Strong Long-Lived Squall Lines" Revisited. *J. Atmos. Sci.*, **61** (4), 361–382, doi:10.1175/1520-0469(2004)061<0361:ATFSLS>2.0.CO;2.
- Williams, E. R., 2008: Comment on "Atmospheric controls on the annual cycle of North African dust" by S. Engelstaedter and R. Washington. *J. Geophys. Res.*, **113** (D23), 1–3, doi:10.1029/2008JD009930.
- WMO, 2010: *Manual on Codes, International Codes, Vol. I.1, Part A - Alphanumeric Codes*, WMO-No. 306, Vol. I.1. World Meteorological Organization, Geneva, Switzerland, 506 pp.
- Xu, X., H. Georg, and S. Zhang, 2009: An algorithm to detect tropical deep convective clouds through AMSU-B water vapor channels. *J. Ocean Univ. China*, **8** (1), 9–14, doi:10.1007/s11802-009-0009-9.
- Xue, Y., and Coauthors, 2010: Intercomparison and analyses of the climatology of the West African Monsoon in the West African Monsoon Modeling and Evaluation project (WAMME) first model intercomparison experiment. *Clim. Dyn.*, **35** (1), 3–27, doi:10.1007/s00382-010-0778-2.
- Zhang, G., and N. a. McFarlane, 1995: Sensitivity of climate simulations to the parameterization of cumulus convection in the Canadian climate centre general circulation model. *Atmosphere-Ocean*, **33** (3), 407–446, doi:10.1080/07055900.1995.9649539.
- Zhang, G. J., 2009: Effects of entrainment on convective available potential energy and closure assumptions in convection parameterization. *J. Geophys. Res. Atmos.*, **114** (7), 1–12, doi:10.1029/2008JD010976.
- Zipser, E. J., 1977: Mesoscale and Convective-Scale Downdrafts as Distinct Components of Squall-Line Structure. *Mon. Weather Rev.*, **105** (12), 1568–1589, doi:10.1175/1520-0493(1977)105<1568:MACDAD>2.0.CO;2.

Acronyms

AAPP	ATOVS and AVHRR preprocessing package. 28
AEJ	African Easterly Jet. 4, 5, 18
AEW	African Easterly Wave. 2, 4, 5, 9, 10, 17, 18
AFWA	Air Force Weather Agency. 39
AMCI	Atlas Mountains Convection Index. 54–57, 85
AMMA	African Monsoon Multidisciplinary Analyses. 1, 4, 10, 85
AMS	American Meteorological Society. 14
AMSU-B	Advanced Microwave Sounding Unit-B. 27, 35, 37
ARW	Advanced Research WRF. 40
AWS	Automated Weather Station. 2, 19, 21–23, 25, 32, 33, 67, 72
BT	Brightness Temperature. 25, 36
BTD	Brightness Temperature Difference. 25, 87, 90
CAPE	Convective Available Potential Energy. 11, 12, 53
CCDF	Complementary Cumulative Censity Function. 38
CES	Central Evaluation System. 7
CIN	Convective Inhibition. 11, 12
CLASS	NOAA Comprehensive Large Array-Data Stewardship System. 28, 87
CMIP5	Coupled Model Intercomparison Project Phase 5. 84
CWV	Column Water Vapor. 11, 26, 27, 69, 83
DCAPE	Downdraft Convective Available Potential Energy. 12
DUP	Dust Uplift Potential. 15, 16, 52, 78, 79
ECMWF	European Centre for Medium-Range Weather Forecasts. 2, 3, 10, 21, 22, 29, 54, 60–62, 67, 85
EJ	Easterly Jet. 5
ESA	European Space Agency. 25

EUMETSAT	European Organisation for the Exploitation of Meteorological Satellites. 25 , 27
FAA	Federal Aviation Administration. 39
GEWEX	Global Energy and Water Exchanges. 8
GPM	Global Precipitation Measurement. 28
GTS	Global Telecommunication System. 24
HLE	Heat Low East. 9
HLW	Heat Low West. 9
IFS	Integrated Forecast System. 29
IMPETUS	Integrated Approach to the Efficient Management of Scarce Water Resources in West Africa. 22 , 25 , 31–34 , 47–54 , 56 , 59 , 63 , 82
IOP	Intensive Observation Period. 22
IPCC	Intergovernmental Panel on Climate Change. 17
IR	Infrared. 15 , 18 , 48 , 67
ISD	Integrated Surface Database. 24 , 48–52 , 54 , 56 , 82
ITCZ	Inter-Tropical Convergence Zone. 8
ITD	Inter-Tropical discontinuity. 4 , 5 , 7 , 85
LES	Large eddy simulation. 39
LFC	Level of Free Convection. 11
LH	Latent Heat. 41
MARS	Meteorological Archival and Retrieval System. 29
MCS	Mesoscale Convective System. 2 , 4 , 16–18 , 41 , 44 , 69
METAR	Aerodrome routine meteorological reports. 24 , 83
MHS	Microwave Humidity Sounder. 27 , 35 , 37
MSG	Meteosat Second Generation. 25
MSLP	Mean sea level pressure. 68
NCAR	National Center for Atmospheric Research. 39 , 40
NCDC	National Climatic Data Center. 24
NCEP	National Centers for Environmental Prediction. 39 , 40
NLLJ	Night-time Low-Level Jet. 16 , 41 , 77 , 78 , 82
NMM	Non-hydrostatic Mesoscale Model. 40

NOAA	National Oceanic and Atmospheric Administration. 27, 39
PBL	Planetary Boundary Layer. 10, 41, 74
POES	Polar Orbiting Environmental Satellites. 87
PW	Precipitable Water. 11
RFI	Radio Frequency Interference. 28, 36
RGB	Red-Green-Blue. 25
RMSE	Root-Mean-Square Error. 76
RUDICS	Iridium Router-Based Unrestricted Digital Internetworking Connectivity Solutions. 23
SEVIRI	Spinning Enhanced Visible and InfraRed Imager. 25, 28, 53, 59, 61, 62
SHL	Saharan Heat Low. 1–10, 13, 16–19, 29, 40, 41, 46, 53, 60, 68, 69, 81, 83–86
SNR	Signal-to-Noise Ratio. 90
SST	Sea Surface Temperature. 1
STJ	Sub-Tropical Jet. 5
SYNOP	Standard surface synoptic observations. 24
TEI	Tropical-extra-Tropical Interactions. 49
TEJ	Tropical Easterly Jet. 5
TKE	Turbulent Kinetic Energy. 31
TRMM	Tropical Rainfall Measuring Mission. 8, 28
UM	UK Met Office Unified Model. 46
WAHL	West African Heat Low. 4
WAM	West African Monsoon. 1, 2, 4, 5, 7, 8, 16, 81, 83, 85, 86
WMO	World Meteorological Organization. 24, 81
WRF	Weather Research and Forecast. 13, 15, 17, 19, 29, 31, 39–41, 44, 46, 55, 59, 61–63, 67, 74, 79, 81, 83, 86
WSF	WRF Software Framework. 40

Danksagung

Zuerst möchte ich meinen Betreuern Prof. Dr. Andreas H. Fink und Prof. Dr. Peter Knippertz danken, die mir die Möglichkeit gegeben haben mit diesem interessanten Thema meinem Interesse an dem afrikanischen Kontinent nachgehen zu können. Trotz der räumlichen Entfernung gab es immer die Möglichkeit zur Diskussion, aber auch die Freiheit Ideen meinen Vorstellungen entsprechend umzusetzen. Danke auch für die Unterstützung bei der Vorbereitung der beiden Teilpublikationen.

Diese Arbeit wurde von der Deutschen Forschungsgemeinschaft (DFG) unter der Förderkennziffer FI 786/3-1 gefördert.

Des Weiteren danke ich Prof. Dr. Susanne Crewell für das Begutachten der Arbeit, Prof. Dr. Joachim Saur für die Übernahme des Vorsitzes bei der Disputation und Dr. Patrick Ludwig für das Protokollieren der selbigen.

I am also grateful to Julie Berckmans and Philipp Aben for the maintenance of the IMPETUS stations in Morocco, your efforts have been an important contribution.

Many Thanks also to Dr. John Marsham and Prof. Dr. Doug Parker for suggestions and discussions in Leeds, as well as for the uncomplicated exchange of data in a rather complicated environment.

Die im Rahmen dieser Arbeit durchgeführten Simulationen haben sehr viel Rechenzeit gekostet. Ich möchte dem regionalen Rechenzentrum der Universität zu Köln (RRZK) dafür danken mir diese auf dem Hochleistungsrechner CHEOPS sehr großzügig zur Verfügung gestellt zu haben.

Vielen Dank auch an meine Kommilitonen, Kollegen und Freunde am Institut für Geophysik und Meteorologie. Ihr hattet einen ganz wesentlichen Anteil daran, dass mir die Meteorologie in den letzten Jahren viel Freude bereitet hat.

Zuletzt möchte ich der wichtigsten Person danken, meiner lieben Frau Steffi. Vielen Dank für Deine Unterstützung und Deine Liebe, ganz besonders in den letzten Wochen. Vielen Dank auch für das unermüdliche Korrigieren der immer wieder gleichen Fehler und Deine sehr hilfreichen Ratschlägen beim Erstellen dieser Arbeit.

Erklärung

Ich versichere, dass ich die von mir vorgelegte Dissertation selbständig angefertigt, die benutzten Quellen und Hilfsmittel vollständig angegeben und die Stellen der Arbeit – einschließlich Tabellen, Karten und Abbildungen –, die anderen Werken im Wortlaut oder dem Sinn nach entnommen sind, in jedem Einzelfall als Entlehnung kenntlich gemacht habe; dass diese Dissertation noch keiner anderen Fakultät oder Universität zur Prüfung vorgelegen hat; dass sie – abgesehen von unten angegebenen Teilpublikationen – noch nicht veröffentlicht worden ist sowie, dass ich eine solche Veröffentlichung vor Abschluss des Promotionsverfahrens nicht vornehmen werde. Die Bestimmungen der Promotionsordnung sind mir bekannt. Die von mir vorgelegte Dissertation ist von Prof. Dr. Andreas H. Fink und Prof. Dr. Peter Knippertz betreut worden.

Freising, den 17. Mai 2016

Robert Redl

Teilpublikationen

Redl, R., A. H. Fink, and P. Knippertz, 2015: An Objective Detection Method for Convective Cold Pool Events and Its Application to Northern Africa. *Mon. Weather Rev.*, **143** (12), 5055–5072, ©American Meteorological Society. Used with permission. doi: [10.1175/MWR-D-15-0223.1](https://doi.org/10.1175/MWR-D-15-0223.1)

Redl, R., P. Knippertz, and A. H. Fink, 2016: Weakening and Moistening of the Summertime Saharan Heat Low through Convective Cold Pools from the Atlas Mountains. *J. Geophys. Res. Atmos.*, **121**, ©American Geophysical Union. Used with permission. doi: [10.1002/2015JD024443](https://doi.org/10.1002/2015JD024443)